

**FUNCTIONAL ANALYSIS OF CONSERVED AROMATIC RESIDUES  
IN HELIX 7 CRITICAL FOR LARVICIDAL ACTIVITY OF THE  
*Bacillus thuringiensis* Cry4Ba TOXIN**



**A THESIS SUBMITTED IN PARTIAL FULFILLMENT  
OF THE REQUIREMENTS FOR  
THE DEGREE OF DOCTOR OF PHILOSOPHY  
(MOLECULAR GENETICS AND GENETIC ENGINEERING)  
FACULTY OF GRADUATE STUDIES  
MAHIDOL UNIVERSITY**

**2007**


**COPYRIGHT OF MAHIDOL UNIVERSITY**


Thesis  
Entitled


**FUNCTIONAL ANALYSIS OF CONSERVED AROMATIC RESIDUES  
IN HELIX 7 CRITICAL FOR LARVICIDAL ACTIVITY OF THE  
*Bacillus thuringiensis* Cry4Ba TOXIN**


KASORN TIEWSIRI


Miss Kasorn Tiew Siri  
Candidate

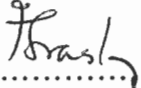
  
Assoc. Prof. Chanan Angsuthanasombat, Ph.D.  
Major-Advisor


  
Prof. Emeritus Prapon Wilairat, Ph.D.  
Co-Advisor

  
Asst. Prof. Chamras Promptmas, Ph.D.  
Co-Advisor

  
Asst. Prof. Panadda Boonserm, Ph.D.  
Co-Advisor

  
Lect. Dr. Kittisak Yokthongwattana  
Co-Advisor

  
Prof. M.R. Jisnuson Svasti, Ph.D.  
Dean  
Faculty of Graduate Studies

  
Asst. Prof. Varaporn Akkarapatumwong, Ph.D.  
Chair  
Doctor of Philosophy Programme in  
Molecular Genetics and Genetic Engineering  
Institute of Molecular Biology and Genetics

Thesis  
Entitled

**FUNCTIONAL ANALYSIS OF CONSERVED AROMATIC RESIDUES  
IN HELIX 7 CRITICAL FOR LARVICIDAL ACTIVITY OF THE  
*Bacillus thuringiensis* Cry4Ba TOXIN**

was submitted to the Faculty of Graduate Studies, Mahidol University  
for the degree of Doctor of Philosophy  
(Molecular Genetics and Genetic Engineering)

On

March 29, 2007

KASORN TIEWSIRI

Miss Kasorn Tiewsiiri  
Candidate

*V. Akkarapatumwong*

Asst. Prof. Varaporn Akkarapatumwong, Ph.D.  
Chair

*C. Angsuthanasombat*

Assoc. Prof. Chanan Angsuthanasombat, Ph.D.  
Member

*W. Fischer*

Prof. Wolfgang B Fischer, Ph.D.  
Member

*Cham Promptmas*

Asst. Prof. Chamras Promptmas, Ph.D.  
Member

*J. Torres*

Assoc. Prof. Jaime Torres, Ph.D.  
Member

*P. Boonserm*

Asst. Prof. Panadda Boonserm, Ph.D.  
Member

*M.R. Jisnuson Svasti*

Prof. M.R. Jisnuson Svasti, Ph.D.  
Dean  
Faculty of Graduate Studies  
Mahidol University

*C. Krittanai*

Asst. Prof. Chartchai Krittanai, Ph.D.  
Acting Director  
Institute of Molecular Biology and Genetics  
Mahidol University

## ACKNOWLEDGEMENTS

I would like to express my sincere appreciation to many persons, especially my major advisor, Assoc. Prof. Chanan Angsuthanasombat, for his warm guidance, valuable advice and encouragement during the various stages of this thesis project. I would also like to thank my co-advisors, Prof. Praon Wilairat, Asst. Prof. Gerd Katzenmeier, Asst. Prof. Panadda Boonserm, Asst. Prof. Chamras Promptmas and Lect. Dr. Kittisak Yokthongwattana for their constructive comments and discussion for this research project. I would like to give my sincere thank to Assoc. Prof. Jaime Torres for his great advice in ATR-FTIR spectroscopy and Prof. Wolfgang B Fischer for his guidance, advice in molecular dynamics simulations.

My appreciation also is extended to Ms. Anchalee Nirachanon for her great help in managing all documents and scholarship budgets during the whole project period. I would like to thank to all BT members, especially Ms. Somsri Sakdee, and all my friends for their great assistance in solving problems in Singapore and England, wonderful friendships. Finally, I am grateful to express my deepest appreciation to my parent for both's entirely care and encouragement.

I am particularly indebted to the Royal Golden Jubilee Ph.D. program, conducted by the Thailand Research Fund (TRF) that provided me the good opportunity for doing this project.

Kasorn Tiewsiriri

FUNCTIONAL ANALYSIS OF CONSERVED AROMATIC RESIDUES IN HELIX 7 CRITICAL FOR LARVICIDAL ACTIVITY OF THE *Bacillus thuringiensis* Cry4Ba TOXIN

KASORN TIEWSIRI 4636654 MBMG/D

Ph.D. (MOLECULAR GENETICS AND GENETIC ENGINEERING)

THESIS ADVISORS: CHANAN ANGSUTHANASOMBAT, Ph.D.,  
CHAMRAS PROMPTMAS, Ph.D., PANADDA BOONSERM, Ph.D.,  
PRAPON WILAIRAT, Ph.D., KITTISAK YOKTHONGWATTANA, Ph.D.

ABSTRACT

Functional elements of the conserved helix 7 in the pore-forming domain of the *Bacillus thuringiensis* Cry  $\delta$ -endotoxins have not yet been clearly identified. In this study, alanine substitutions were initially performed for four highly conserved aromatic residues, Trp<sup>243</sup>, Phe<sup>246</sup>, Tyr<sup>249</sup> and Phe<sup>264</sup>, in helix 7 of the Cry4Ba mosquito-larvicidal protein. Bioassays against *Stegomyia aegypti* mosquito-larvae revealed that only W243A, Y249A and F264A mutant toxins displayed a dramatic decrease in toxicity. Further mutagenic analysis showed that replacements with an aromatic residue particularly at Tyr<sup>249</sup> and Phe<sup>264</sup> still retained the high-level toxin activity. In addition, a nearly complete loss in larvicidal activity was found for Y249L/F264L or F264A/Y249A double mutants, confirming the involvement in toxicity of both aromatic residues, which face towards the same direction. By using ATR-FTIR, a 27-residue peptide corresponding to Cry4Ba- $\alpha$ 7 in DMPC multibilayers was found to exhibit a mixture of  $\alpha$ -helical and  $\beta$ -sheet structures. However, the  $\alpha$ 7 peptide incorporated in DMPG and DDPC could adopt predominantly  $\alpha$ -helix and  $\beta$ -sheet, respectively. In addition, changes in the peptide-lipid ratio revealed variations in the peptide conformational ratio of  $\alpha$ -helix to  $\beta$ -structure. Hydrogen/deuterium exchange suggested that the  $\beta$ -form was approximately 90% insertion into the DMPC lipid membranes, with an average tilt angle of 47°, whilst the  $\alpha$ -helical form was placed on the membrane surface with ~40% insertion and both critical aromatic residues pointing towards the membrane. These results are consistent with that of a 10-ns MD simulations of both conformations in the DMPC bilayers. Altogether, the data suggest a potential role of two critical aromatic residues, Tyr<sup>249</sup> and Phe<sup>264</sup>, in the Cry4Ba toxin activity.

KEY WORDS: AROMATICITY/ ATR-FTIR/ *Bacillus thuringiensis*/  $\delta$ -ENDOTOXIN, DMPC/ LARVICIDAL ACTIVITY/ MD SIMULATIONS

156 P.

การศึกษาหน้าที่ของกรดอะมิโนโรมาติกที่อนุรักษ์ในเกลียวอัลฟา 7 ของโปรตีนฆ่าลูกน้ำของ Cry4Ba จากแบคทีเรีย *Bacillus thuringiensis* (FUNCTIONAL ANALYSIS OF CONSERVED AROMATIC RESIDUES IN HELIX 7 CRITICAL FOR LARVICIDAL ACTIVITY OF THE *Bacillus thuringiensis* Cry4Ba TOXIN)

เกษร เตียวศิริ 4636654 MBMG/D

ปร.ค. (อนุพันธุศาสตร์และพันธุวิศวกรรมศาสตร์)

คณะกรรมการควบคุมวิทยานิพนธ์: ชนันท อังสุรนสมบัติ Ph.D. จำรัส พร้อมมาส Ph.D.

ปนัดดา บุญเสริม Ph.D. ประพนธ์ วิไลรัตน์ Ph.D. กิตติศักดิ์ หยกทองวัฒนา Ph.D.

### บทคัดย่อ

บทบาทหน้าที่ของเกลียวอัลฟา 7 ซึ่งค่อนข้างอนุรักษ์ (conserved) ของโปรตีนฆ่าลูกน้ำของ Cry4Ba ยังไม่มีการวินิจฉัยอย่างชัดเจน ในการศึกษากรดอะมิโนโรมาติกที่อนุรักษ์ในเกลียวอัลฟา 7 อันได้แก่ Trp<sup>243</sup>, Phe<sup>246</sup>, Tyr<sup>249</sup> และ Phe<sup>264</sup> ซึ่งถูกแทนที่ด้วย Ala พบว่าโปรตีนกลายพันธุ์ W243A, Y249A และ F264A นั้นมีฤทธิ์การฆ่าลูกน้ำของลาย (*Stegomyia aegypti*) ลดลงมาก ซึ่งเมื่อศึกษาเพิ่มเติมของโปรตีนกลายพันธุ์ใน Tyr<sup>249</sup> และ Phe<sup>264</sup> พบว่าคุณสมบัติความเป็นโรมาติกของทั้งสองกรดอะมิโนนี้ซึ่งวางหันหน้าไปทางเดียวกันในเกลียวอัลฟาที่ 7 นั้นมีความสำคัญต่อฤทธิ์ฆ่าลูกน้ำอย่างมากเมื่อถูกเปลี่ยนแปลงพร้อมกัน (Y249L/F264L หรือ F264A/Y249A) เมื่อศึกษาเพิ่มเติมโดยใช้วิธี ATR-FTIR spectroscopy พบว่าเปปไทด์สังเคราะห์ขนาด 27 กรดอะมิโนที่เหมือนกับเกลียวอัลฟา 7 ซึ่งอยู่ในสภาพของเยื่อหุ้มเซลล์จำลองที่เป็น DMPC นั้นมีทั้งที่เป็นลักษณะเกลียวอัลฟา ( $\alpha$ -helix) และแผ่นเบต้า ( $\beta$ -sheet) แต่เมื่อเปลี่ยนชนิดของเยื่อหุ้มจำลองเป็น DMPG และ DDPC พบว่าเปปไทด์ดังกล่าวมีลักษณะโครงสร้างส่วนใหญ่เป็นเกลียวอัลฟาและแผ่นเบต้า ตามลำดับ และเมื่อปรับเปลี่ยนอัตราส่วนระหว่างเปปไทด์และเยื่อหุ้มไขมันที่ใช้พบว่า มีการแสดงลักษณะโครงสร้างของชิ้นส่วนเกลียวอัลฟา 7 ที่เป็นระหว่างอัลฟาและเบต้าในอัตราส่วนที่แตกต่างกัน นอกจากนี้พบว่าถ้าเป็นลักษณะโครงสร้างเบตานั้นจะมีการฝังตัวลงในเยื่อหุ้มจำลองชนิด DMPC ประมาณ 90% มีค่ามุมเอียงเฉลี่ย 47° แต่ถ้าเป็นลักษณะโครงสร้างเกลียวอัลฟานั้นจะมีการวางตัวเป็นแนวราบขนานกับผิวหน้าของเยื่อหุ้มจำลองพร้อมกับฝังตัวลงในเยื่อหุ้มประมาณ 40% โดยที่กรดอะมิโนโรมาติกทั้ง 2 ซึ่งสำคัญต่อความเป็นพิษนั้นชี้ไปทางเยื่อหุ้มจำลอง โดยผลการทดลองจาก ATR-FTIR นั้นให้ผลสอดคล้องกับการทำ 10-ns MD simulations ของเปปไทด์ดังกล่าวใน DMPC จากผลการทดลองทั้งหมดนี้แนะนำว่า Tyr<sup>249</sup> และ Phe<sup>264</sup> ในเกลียวอัลฟา 7 นั้นน่าจะมีบทบาทสำคัญในการออกฤทธิ์โปรตีนฆ่าลูกน้ำของ Cry4Ba

# CONTENTS

	Page
<b>ACKNOWLEDGEMENTS</b>	iii
<b>ABSTRACT</b>	iv
<b>LIST OF TABLES</b>	x
<b>LIST OF FIGURES</b>	xi
<b>LIST OF ABBREVIATIONS</b>	xv
<b>CHAPTER</b>	
<b>I INTRODUCTION</b>	
1.1 Pore-forming toxins	1
1.2 General background of <i>Bacillus thuringiensis</i>	1
1.3 Classification of <i>Bt</i> $\delta$ -endotoxins	2
1.4 Structure of the Cry toxins	4
1.5 Mechanism of action of the Cry toxins	9
1.5.1 General features	9
1.5.2 Solubilisation and proteolytic activation	9
1.5.3 Receptor binding	10
1.5.4 Membrane insertion and pore formation	13
1.6 ATR-FTIR spectroscopic studies of toxin-membrane interaction	18
1.6.1 Principle of ATR-FTIR spectroscopy	19
1.6.2 Conformation and orientation determination of membrane-bound peptides	22
<b>II OBJECTIVES</b>	23
<b>III MATERIALS AND METHODS</b>	
3.1 Materials	26
3.1.1 Chemicals and reagents	26
3.1.2 Enzymes and accessory buffers	26

## CONTENTS (continued)

	<b>Page</b>
3.1.3 Bacterial strain	27
3.1.4 Recombinant plasmid	27
3.1.5 Oligonucleotide primers	29
3.1.6 Culture media	32
3.1.7 Phosphorus content analysis solution	32
3.1.8 Chromatographic columns	32
3.1.9 Miscellaneous	33
3.2 Methods	33
3.2.1 Plasmid extraction by CTAB method	33
3.2.2 Agarose gel electrophoresis of DNA	34
3.2.3 Site-directed mutagenesis	34
3.2.4 PCR conditions	35
3.2.5 <i>DpnI</i> digestion of PCR products	38
3.2.6 Competent cell preparation using calcium chloride method	38
3.2.7 Plasmid DNA transformation	38
3.2.8 Restriction endonuclease analysis	39
3.2.9 DNA sequencing analysis	39
3.2.10 Toxin expression	40
3.2.11 Toxin inclusion purification	40
3.2.12 SDS-PAGE analysis	41
3.2.13 Toxin inclusion solubilisation and proteolytic processing	41
3.2.14 Mosquito larvicidal activity assays	42
3.2.15 Purification of Cry4Ba and its derivatives	42
3.2.16 Purification of helix 6 and helix 7 peptides	42
3.2.17 Circular dichroism (CD) measurement	43
3.2.18 Intrinsic fluorescence spectroscopy	43

## CONTENTS (continued)

	<b>Page</b>
3.2.19 Preparation of calcein-entrapped LUVs	43
3.2.20 Phosphorus content analysis of phospholipid	44
3.2.21 Membrane permeation assay	44
3.2.22 ATR-FTIR spectroscopy	45
3.2.22.1 Sample preparation	45
3.2.22.2 Polarised ATR-FTIR measurements	45
3.2.22.3 Analysis of ATR-FTIR data	45
3.2.23 Molecular dynamics simulations	47
<b>IV RESULTS: Mutagenesis of conserved aromatic residues in helix 7 of Cry4Ba</b>	
4.1 Constructions of Cry4Ba-mutant plasmids	49
4.2 Expression of the Cry4Ba-helix 7 mutant toxins	50
4.3 Solubilisation and proteolytic processing of the Cry4Ba-helix 7 mutants	50
4.4 Larvicidal activity of Cry4Ba-helix 7 mutant toxins	50
4.5 Mutagenic analysis of Trp <sup>243</sup> , Phe <sup>246</sup> , Tyr <sup>249</sup> and Phe <sup>264</sup>	62
4.6 Expression of the Cry4Ba mutant toxins	83
4.7 Larvicidal activity of Cry4Ba mutant toxins	83
4.8 Solubilisation and proteolytic processing of the Cry4Ba mutant toxins	83
<b>V RESULTS: Functional characterization of conserved aromaticity in Cry4Ba-helix 7</b>	
5.1 Purification of Cry4Ba and its mutants	94
5.2 Secondary structure of Cry4Ba and its mutants	94
5.3 Fluorescence emission spectra of Cry4Ba and its mutants	95
5.4 Membrane perturbing activity of Cry4Ba and its mutants	95
5.5 ATR-FTIR measurement of the helix 7 peptide	100

## CONTENTS (continued)

	<b>Page</b>
5.5.1 Quantification of secondary structure of the $\alpha$ 7 peptide	100
5.5.2 Orientation of helix 7 incorporated into lipid membranes	104
5.5.3 Secondary structures and orientation determination of helix 7 peptide using $C^{13}=O^{18}$	106
5.5.4 Localisation of Tyr <sup>249</sup> and Phe <sup>264</sup> in helix 7 of the Cry4Ba toxin	106
5.6 Peptide-induced membrane perturbation	114
5.7 Structure and dynamics of the helix 7 peptide in DMPC bilayers	114
<b>VI DISCUSSIONS</b>	
6.1 Solubilisation and proteolytic processing of the Cry4Ba mutants	122
6.2 Functional characterisation of the conserved aromaticity in Cry4Ba-helix 7	124
6.3 Characterisation of the helix 7 peptide in lipid membranes	125
6.4 Structure and dynamics of the helix 7 peptide in DMPC bilayers	129
<b>VII CONCLUSIONS</b>	136
<b>REFERENCES</b>	138
<b>APPENDIX</b>	153
<b>BIOGRAPHY</b>	156

## LIST OF TABLES

Tables		Page
3.1	Temperature cycling parameters for site-directed mutagenesis	35
3.2	Annealing temperature ( $T_a$ ) for each mutant	37
5.1	Estimated percentage of secondary structural contents of helix 7 in DMPC, DMPG and DDPC with different peptide-to-lipid ratios	103
5.2	Orientation analysis of helix 7 peptide in DMPC, DMPG and DDPC with different peptide-to-lipid ratios	111

## LIST OF FIGURES

Figures	Page
1.1 Electron micrograph of <i>Bacillus thuringiensis</i> subsp. <i>israelensis</i>	3
1.2 Phylogram of amino acid sequence identity among Cry proteins	5
1.3 Ribbon illustrations of crystallographic resolved Cry toxins	7
1.4 Positions of conserved blocks among the <i>Bt</i> Cry proteins	8
1.5 Model of the mode of action of the Cry1A-lepidopteran toxin	14
1.6 Schematic presentation of the umbrella model for the pore-forming mechanism of Cry toxins	18
1.7 Geometric configuration of an ATR setup	21
2.1 3D structure of the Cry4Ba toxin	25
3.1 Physical map of the plasmid pMU388	28
3.2 Site-directed mutagenesis method	36
4.1 PCR amplification of Cry4Ba mutant plasmids	51
4.2 The PCR products of Cry4Ba mutant plasmids digested with <i>DpnI</i>	52
4.3 Restriction digestion and DNA sequencing analysis of pW243A	53
4.4 Restriction digestion and DNA sequencing analysis of pF246A	54
4.5 Restriction digestion and DNA sequencing analysis of pY249A	55
4.6 Restriction digestion and DNA sequencing analysis of pF264A	56
4.7 Expression of the Cry4Ba mutant toxins	57
4.8 Solubility of Cry4Ba mutant inclusions	58
4.9 Trysinised products of the Cry4Ba-F246A mutant toxin	59
4.10 Larvicidal activity of <i>E. coli</i> cells expressing of W <sup>243</sup> , F <sup>246</sup> , Y <sup>249</sup> and F <sup>264</sup> mutants	60
4.11 Larvicidal activity of toxin inclusions of W <sup>243</sup> , F <sup>246</sup> , Y <sup>249</sup> and F <sup>264</sup> mutants	61
4.12 PCR amplification of Cry4Ba mutant plasmids, Y249E, Y249R, Y249H, Y249L, Y249F and Y249W	63

## LIST OF FIGURES (continued)

Figures	Page
4.13 The PCR products of Cry4Ba-F264 mutant plasmids digested with <i>DpnI</i>	64
4.14 The PCR products of Cry4Ba-W243 and double mutant plasmids digested with <i>DpnI</i>	65
4.15 Restriction digestion and DNA sequencing analysis of pY249E	66
4.16 Restriction digestion and DNA sequencing analysis of pY249R	67
4.17 Restriction digestion and DNA sequencing analysis of pY249H	68
4.18 Restriction digestion and DNA sequencing analysis of pY249L	69
4.19 Restriction digestion and DNA sequencing analysis of pY249F	70
4.20 Restriction digestion and DNA sequencing analysis of pY249W	71
4.21 Restriction digestion and DNA sequencing analysis of pF264E	72
4.22 Restriction digestion and DNA sequencing analysis of pF264R	73
4.23 Restriction digestion and DNA sequencing analysis of pF264H	74
4.24 Restriction digestion and DNA sequencing analysis of pF264L	75
4.25 Restriction digestion and DNA sequencing analysis of pF264W	76
4.26 Restriction digestion and DNA sequencing analysis of pF264Y	77
4.27 Restriction digestion and DNA sequencing analysis of pW243K	78
4.28 Restriction digestion and DNA sequencing analysis of pW243L	79
4.29 Restriction digestion and DNA sequencing analysis of pW243F	80
4.30 Restriction digestion and DNA sequencing analysis of pF264A/Y249A	81
4.31 Restriction digestion and DNA sequencing analysis of pY249L/F264L	82
4.32 Expression of the Trp-243 and double mutants	85
4.33 Expression of the Tyr-249 mutants	86
4.34 Expression of the Phe-264 mutants	87
4.35 Solubility of Trp-243 and double mutant inclusions	88
4.36 Solubility of Tyr-249 mutant inclusions	89
4.37 Solubility of Phe-264 mutant inclusions	90

## LIST OF FIGURES (continued)

Figures	Page
4.38 Trypsinised products of the Cry4Ba toxin and its mutants	91
4.39 Larvicidal activity Cry4Ba mutant toxins	92
4.40 Larvicidal activity Cry4Ba mutant inclusions	93
5.1 Size-exclusion chromatogram and SDS-PAGE analysis of purified trypsin-treated Cry4Ba and its mutants	96
5.2 CD spectra of the wild-type Cry4Ba and its mutant toxins	97
5.3 Fluorescence emission spectra of the purified wild-type Cry4Ba and its mutants	98
5.4 Membrane perturbation activity of the Cry4Ba and its mutant toxins	99
5.5 Synthetic peptides corresponding to $\alpha 6$ and $\alpha 7$ of the Cry4Ba toxin	101
5.6 Secondary structural contents of helix 7 in different lipid membranes	102
5.7 ATR-FTIR spectra of helix 7 peptide in DMPC membranes	107
5.8 ATR-FTIR spectra of helix 7 peptide in DMPG membranes	108
5.9 ATR-FTIR spectra of helix 7 peptide in DDPC membranes	109
5.10 ATR-FTIR spectra of helix 6 peptide in DMPC membranes	110
5.11 Polarised ATR-FTIR spectra of the isotope probe $^{13}\text{C}=^{18}\text{O}$ at Val <sup>18</sup>	112
5.12 Polarised ATR-FTIR spectra of the nitrile-derivatised probe at Phe <sup>7</sup> (Phe <sub>CN</sub> )	113
5.13 Effects of Cry4Ba-helical peptides on the entrapped calcein released from LUVs	116
5.14 Schematic ribbon representations of $\alpha$ -helical and $\beta$ -meander conformations of the helix 7 peptide	117
5.15 Trajectory analysis of $\alpha$ -helical structure of the helix 7 peptide in DMPC bilayers	118

**LIST OF FIGURES (continued)**

<b>Figure</b>		<b>Page</b>
5.16	Trajectory analysis of $\beta$ -hairpin structure of the helix 7 peptide in DMPC bilayers	119
5.17	Trajectory analysis of $\alpha$ -helical structure of the helix 6 peptide in DMPC bilayers	120
5.18	The snapshot of $\alpha$ -helix 6 peptide at the membrane water-interface DMPC bilayers	121
6.1	Close-up views of part of the Cry4Ba crystal structure, illustrating the packing interactions	127
6.2	Space-filling representation of the Cry4Ba structure	131
6.3	The snapshot of helix 7 peptide at the membrane water-interface and in the DMPC bilayers	132
6.4	Atomic structure fits of prepore and pore structure of the pneumolysin toxin	134
6.5	Proaerolysin structure and alignments of putative transmembrane domains of different $\beta$ -barrel PFT	135

## LIST OF ABBREVIATIONS

%C	Percent of crosslink
%T	Percent of gel
Å	Angstrom
°C	Degree Celsius
Amp	Ampicillin
APS	Ammonium persulphate
ATR-FTIR	Attenuated total reflection-Fourier transform infrared
AU	Arbitrary unit
bp	Base pair (s)
BSA	Bovine serum albumin
<i>Bt</i>	<i>Bacillus thuringiensis</i>
<i>Bti</i>	<i>Bacillus thuringiensis</i> subsp. <i>israelensis</i>
ca	Approximately
CD	Circular dichroism
CFTs	Channel-forming toxins
Ch	Cholesterol
cm	Centimeter (s)
Cry	Crystal protein
CTAB	Cetyl trimethyl ammonium bromide
Cyt	Cytolytic protein
DMSO	Dimethylsulfoxide
DMPC	Dimyristoylphosphatidylcholine
DNA	Deoxyribonucleic acid
DNase	Deoxyribonuclease

## LIST OF ABBREVIATIONS (continued)

dNTPs	dATP, dGTP, dTTP, dCTP
DTT	1,4-Dithiothreitol
<i>E. coli</i>	<i>Escherichia coli</i>
EDTA	Ethylenediaminetetraacetic acid
EPR	Electron paramagnetic resonance
<i>et al</i>	And others
EtBr	Ethidium bromide
FPLC	Fast protein liquid chromatography
g	gram (s)
h	Hour (s)
IPTG	Isopropyl- $\beta$ -D-thiogalactopyranoside
IR	Infrared
kb	Kilobase
kDa	Kilodalton
LB	Luria-Bertani medium
LUVs	Large unilamellar vesicles
L	Litre
M	Molar
mg	Milligram (s)
min	Minute (s)
ml	Milliliter (s)
mM	Millimolar
mol	Mole
msec	Millisecond (s)

## LIST OF ABBREVIATIONS (continued)

ng	Nanogram (s)
ns	Nanosecond(s)
nm	Nanometer (s)
NMR	Nuclear magnetic resonance
OD	Optical density
PCR	Polymerase chain reaction
PFT	Pore-forming toxin
PC	Phosphatidylcholine
PE	Phosphatidylethanolamine
RP-HPLC	Reverse phase-high performance liquid chromatography
RMS	Root mean square
SEC	Size exclusion chromatography
SDS-PAGE	Sodium dodecyl sulphate-polyacrylamide gel electrophoresis
sec	Second (s)
supsp.	Subspecies
TBE	Tris borate EDTA
TEMED	<i>N,N,N',N'</i> -Tetramethylenediamine
TPCK	Tosyl phenylalanine chloromethyl ketone
Tris	Tris (hydroxymethyl)-aminomethane
UV	Ultraviolet
v/v	Volume by volume
w/v	Weight by volume
w/w	Weight by weight
μg	Microgram (s)
μl	Microliter (s)
μM	Micromola

# CHAPTER I

## INTRODUCTION

### 1.1 Pore-forming toxins

Pore-forming protein toxins (PFTs) are one of Nature's most potent biological weapons. An essential feature of their toxicity is the remarkable property that PFTs can exist either in a stable water-soluble state or as an integral membrane pore. There are now more than a dozen PFTs for which crystal structures have been determined, especially the nature of the conformational changes process. For example, to study clearly defining which regions undergo conformational rearrangements during the pore formation in actinoporins that are a peculiar class of eukaryotic PFT found in sea anemones (1,2,3,4). Many of these toxins appear to function simply by forming pores in cell membrane, disrupting the permeability barrier and leading eventually to cell death (5). PFTs can be broadly classified into two groups, those which are thought to interact with the membrane through  $\alpha$  helices and those which utilise mostly  $\beta$ -sheet structures such as  $\beta$  barrels (6,7). The focus of this thesis is on the insecticidal  $\delta$ -endotoxin (Cry) toxin (8) that is the  $\alpha$ -PFT.

### 1.2 General background of *Bacillus thuringiensis*

*Bacillus thuringiensis* (*Bt*) is a rod-shaped, aerobic, spore-forming Gram-positive bacterium that can be found widespread in nature. It produces protein inclusion during sporulation seeing *Bt* subsp. *israelensis* as an example in **Figure 1.1** (9,10). This microorganism is related to other *Bacillus* species such as *B. cereus*, the causative agent of some types of food poisoning, and *B. anthracis*, the causative agent of anthrax. During sporulation, *Bt* produces unique cytoplasmic proteinaceous inclusions of insecticidal proteins ( $\delta$ -endotoxins) which have been shown to be specifically active against their target insect larvae including Diptera (mosquitoes and blackflies), Lepidoptera (moths and butterflies), Coleoptera (beetles) and Hymenoptera (wasps and bees) (11,12) and hence they are safe for human beings.

Due to these properties, *Bt* has been developed for the control of insect pests and disease vectors (10,13). Strains of *Bt* producing different larvicidal proteins are variously toxic to insect larvae. For instance, the 130-kDa Cry4Ba (see classification below) toxin produced from *Bt* subsp. *israelensis* is specifically toxic to mosquito larvae of the genus *Stegomyia* (*Aedes*) and *Anopheles* which continue to be the most important vectors of such serious human diseases as dengue haemorrhagic fever and malaria (14).

### 1.3 Classification of *Bt* $\delta$ -endotoxins

Formulations of *Bt* have been used for more than two decades as biological insecticides to control agricultural pests and more recently insect vectors of a variety of human and animal diseases. These applied aspects are to a large extent responsible for an increased interest in this bacterium and its crystal proteins in recent years. Extensive screening programs are being carried out by various groups to search for *Bt* strains with new insecticidal spectra, resulting in a variety of sequences and activities that no longer fit the original nomenclature system proposed by Hofte and Whiteley in 1989 (15). Moreover, several sequences are identical or nearly identical and thus represent the same gene or slight variants of the same gene. *Bacillus thuringiensis* pesticidal crystal protein (Cry and Cyt) nomenclature was initially based on insecticidal activity for the primary ranking criterion (15). The Cry toxins (ca. 70-140 kDa) have been initially divided into four major classes, namely CryI to CryIV, based on their insect specificity i.e. lepidopteran-specific (CryI), lepidopteran and dipteran-specific (CryII), coleopteran-specific (CryIII), and dipteran-specific (CryIV) (15). Since inconsistencies existed in the original scheme, a new nomenclature, based on hierarchical clustering using amino acid sequence identity, was proposed (16). The updated  $\delta$ -endotoxin nomenclature is shown in **Figure 1.2**. In the proposed revision, arabic numerals have been used in the primary rank for a class of the toxins (e.g., Cry4Ba for CryIVB) to better accommodate the large number of expected new proteins.

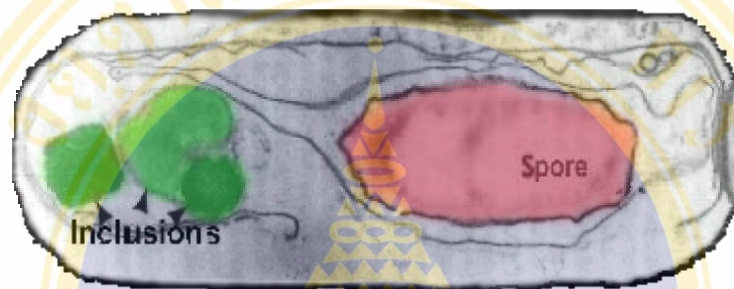


**Figure 1.1** Electron micrograph of *Bacillus thuringiensis* subsp. *israelensis* (10)

The figure shows a transmitted electron micrograph of *Bt* subsp. *israelensis* during sporulation stage. The arrows indicate parasporal inclusion bodies.

Cyt denoted a crystal proteins that exhibit a general cytolytic activity *in vitro* has been retained because of its historical precedent and entrenchment in the research literature. By these criteria, the nontoxic 40-kDa crystal protein from *Bt* subsp. *thompsoni*, for example, has been excluded from the list, but the lepidopteran-active 34-kDa protein (now Cry15Aa) encoded by an adjacent gene of 40-kDa crystal protein has been included (15).

The 130-kDa Cry4Ba toxin is specifically toxic to the *Stegomyia sp.* and *Anopheles sp.* mosquito-larvae. The complete *cry4Ba* gene sequence has been cloned and reported with Genbank accession number X07423 (17).

#### 1.4 Structure of the *Bt* Cry toxins

To date, *Bt* Cry toxin crystal structures have been solved in almost all the major specificity classes, including the lepidopteran-specific Cry1Aa (18) and Cry1Ac (19), the lepidopteran, dipteran-dual specific Cry2Aa (20), the coleopteran-specific Cry3Aa (8), and more recently the dipteran-specific Cry4Ba (21) and Cry4Aa (22). They all share a high degree of overall structural similarity with three-distinct domain organisation (**Figure 1.3**). Certain structures common to *Bt* toxins suggest a kind of "built-in" variability which gives great flexibility of *Bt* in its action in different target insects. Like antibodies, their toxin genes and proteins consist of both alternating conserved and variable regions. The N-terminal part of the Cry protoxin has been shown to be responsible for toxicity and specificity. The C-terminal part is usually highly conserved and probably responsible for crystal formation.

The N-terminal domain I (DI) is a seven antiparallel  $\alpha$ -helices in which helix 5 is relatively hydrophobic and encircled by the remaining six helices. This domain is likely to be transmembrane pore-forming apparatus due to its sufficient length to account for penetration across through biological membrane bilayers. Structure and function relationship studies via site-directed mutagenesis in this domain proved that DI, or a part of them, was responsible for membrane insertion and pore formation as well as its larvicidal activity (23,24,25,26,27). Domain II (DII) consists of three antiparallel  $\beta$ -sheets joined in a typical "Greek key" topology, arranged in a so-called  $\beta$ -prism fold (28).

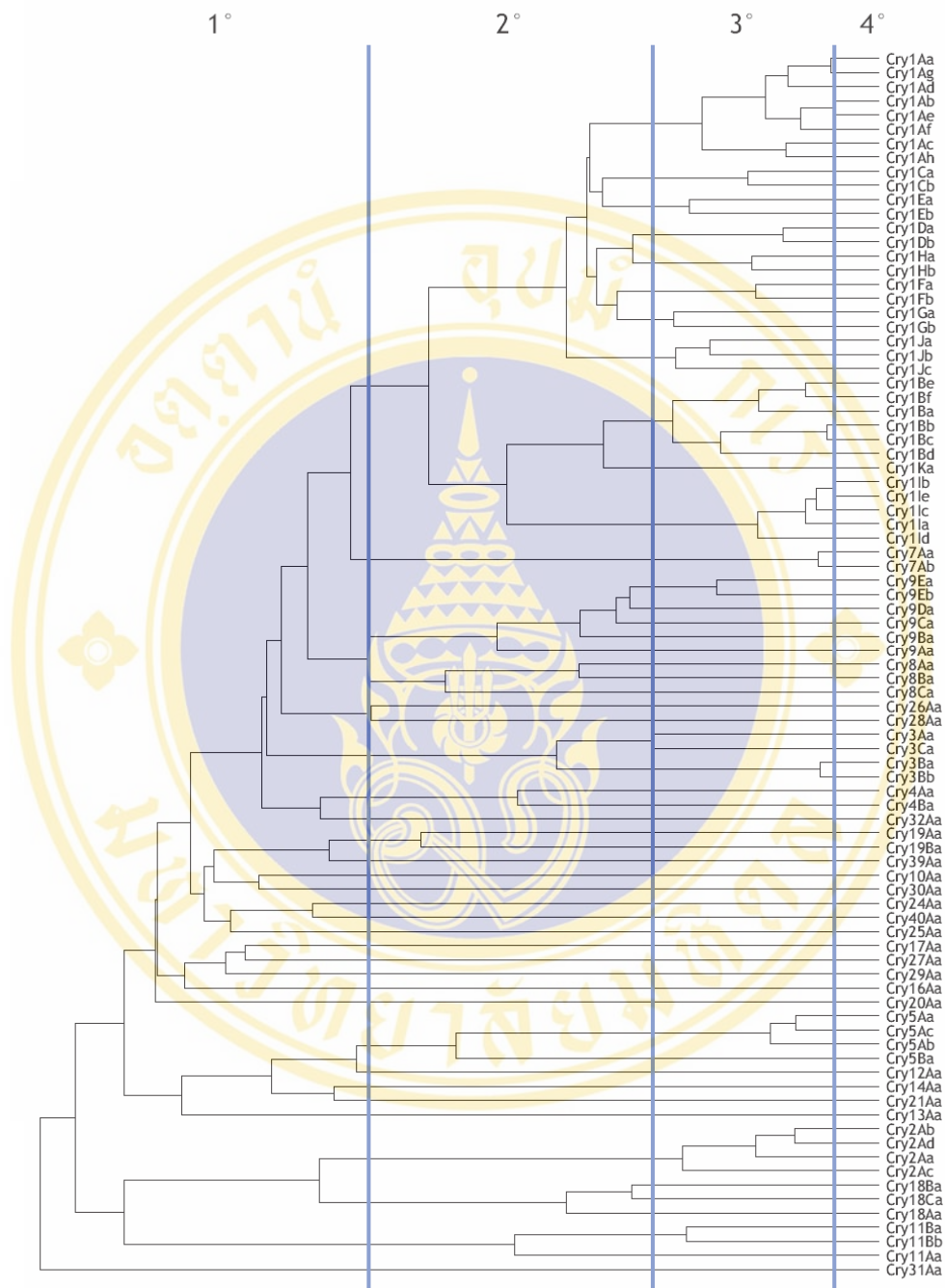


**Figure 1.2 Phylogram of amino acid sequence identity among Cry proteins (16)**

The modified phylogenetic tree visualisation of multiple alignment and distance matrix of the full-length toxin sequences, as described in. The gray vertical bars demarcate the four levels of nomenclature ranks. The updated figure can be accessed at [http://www.biols.susx.ac.uk/Home/Neil\\_Crickmore/Bt/index.html](http://www.biols.susx.ac.uk/Home/Neil_Crickmore/Bt/index.html).

This domain has been shown to be involved in insect specificity due to its high-affinity binding to the receptors (11). The C-terminal domain III (DIII) consists of two twisted, antiparallel  $\beta$ -sheets forming a  $\beta$ -sandwich with a “jelly roll” topology. A number of mutagenesis and recombination experiments have shown that this domain is likely to be responsible in insect specificity (29,30,31) or ion regulation (32). Complete amino acid sequence alignment of the Cry proteins reveals five blocks (**Figure 1.4**) which show to be highly conserved among most of the Cry family (15). Block 1 encompasses helix 5 of DI. This helix has been implicated in pore formation, a role that might explain its highly conserved nature. The central location of helix 5 within DI also suggests an essential role in maintaining the structural integrity of the helical bundle. Block 2 includes helix 7 of the DI and the first  $\beta$ -strand of DII. These structures act as equivalent salt bridges presenting between DI and DII observed in Cry1Aa and Cry3Aa (18) in which these residues lie within block 2. These interactions could be significant for the conformation changes upon binding to the toxin receptor and maintaining the structure integrity as globular form during solubilisation and activation. Block 3 corresponds to the last  $\beta$ -strand of the DII ( $\beta$ 11) and  $\beta$ 13- $\beta$ 15. This block is involved in interactions between DI and DIII. Block 4 contains  $\beta$ 17 and a conserved alternative arginine sequence tract lying in DIII. These residues have been implicated in channel function (33,34,35). Block 5 is located at the end of DIII. It has been proposed that a high degree of the alignment score of the Cry toxins reflected similarity in their 3D structures or the corresponding domains which can be virtually superimposed (11).

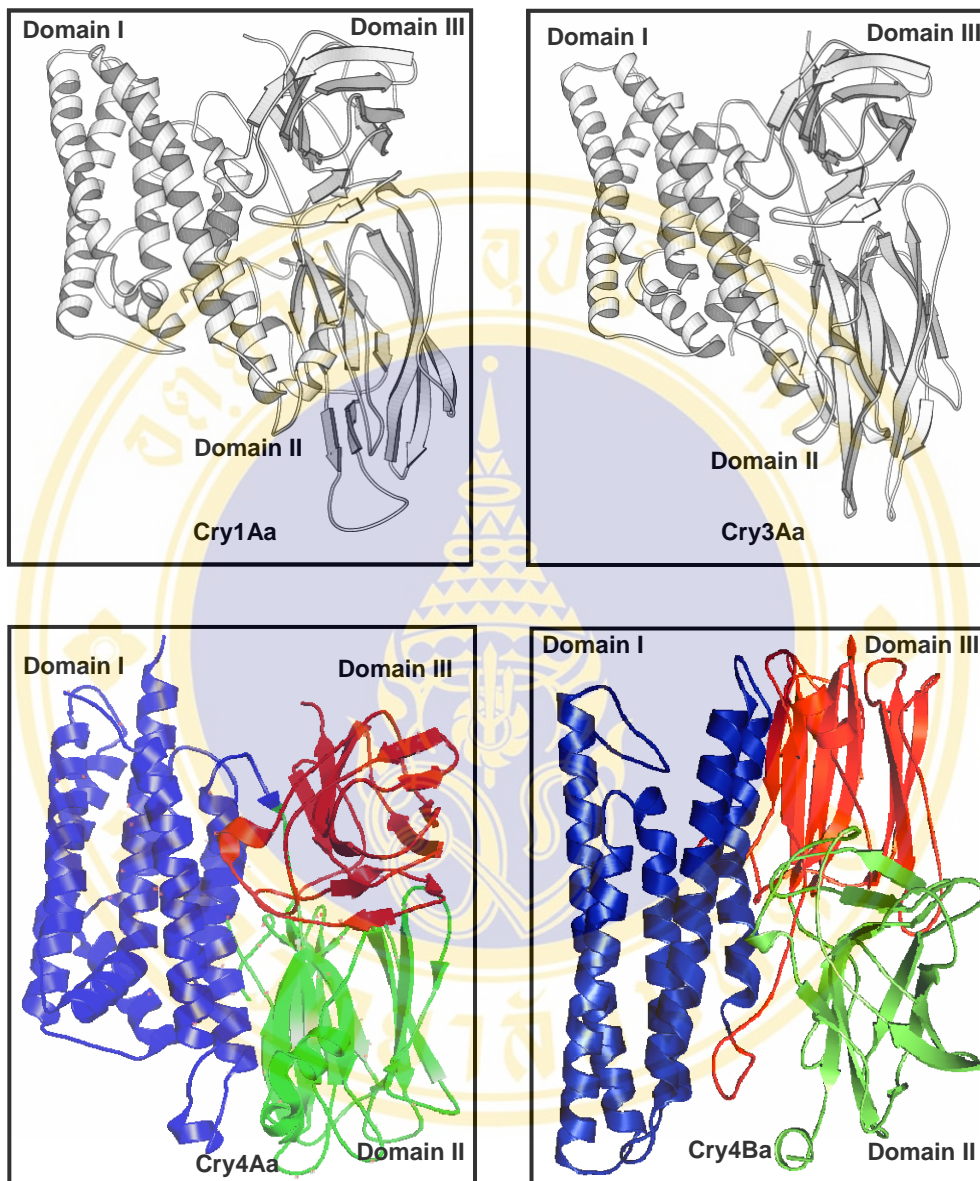


**Figure 1.3 Ribbon illustrations of crystallographic resolved Cry toxins**

The figure shows side view of four 3D structures of the Cry1Aa (18), Cry3Aa (8), Cry4Aa (22) and Cry4Ba (21) determined by X-ray crystallography. These ribbon illustrations demonstrate high similarity in their overall structures, with three-domain organisations (DI-DIII).

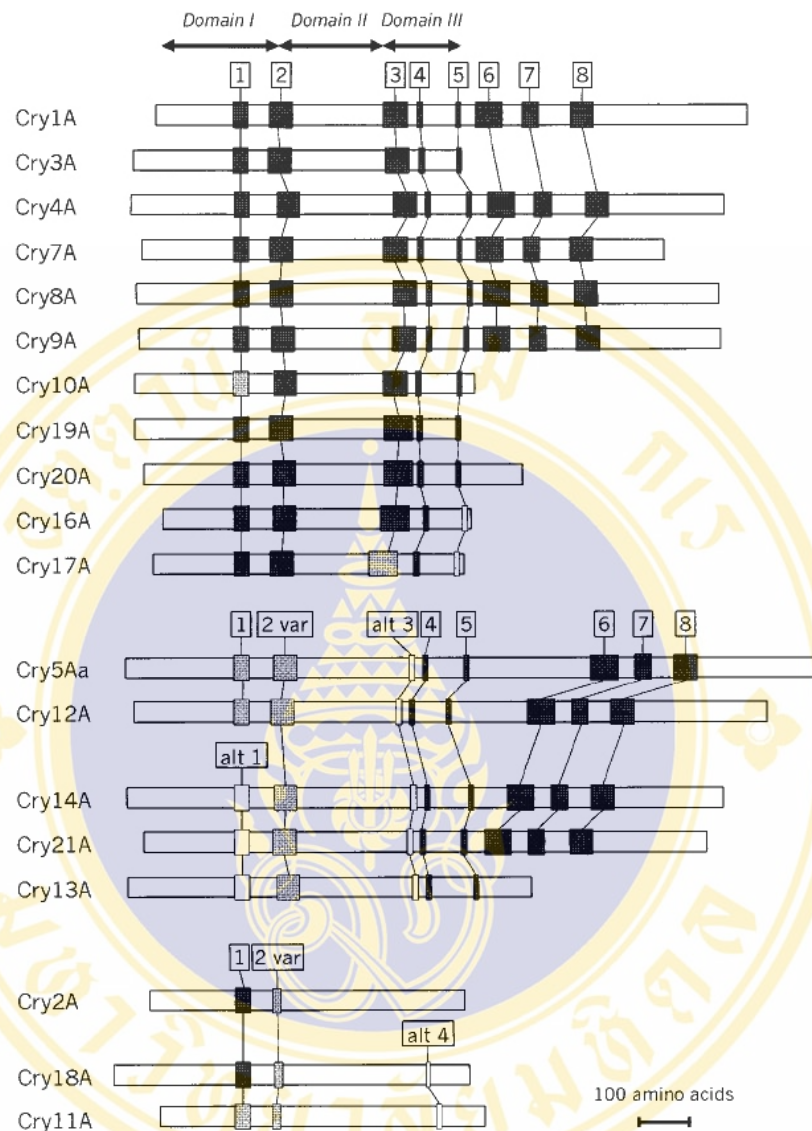


**Figure 1.4 Positions of conserved blocks among the *Bt* Cry proteins**

The sequence blocks are shown as dark gray, light gray or white to indicate the high, moderate or low degree of homology, respectively, to the consensus sequences for each conserved block. Variant (var) sequences conform to the consensus sequence of the highly conserved group at 50 to 75% of the positions. Alternate (alt) blocks are derived from groups of proteins having a consensus sequence over that sequence block that differs from the corresponding highly conserved sequence at more than half of its positions. The length of each protein and the conserved blocks within them are drawn to scale (11).

## 1.5 Mechanism of action of the Cry toxins

### 1.5.1 General features

In general, following the ingestion by susceptible insect larvae, the protoxin inclusions are solubilised in the midgut lumen which is highly alkaline for many dipteran and lepidopteran larvae (11). The liberated soluble protoxins are then processed by larval gut proteases to yield the active toxins. It has been shown for several Cry toxins that the activated toxins bind to specific receptors located on the apical brush-border membrane of midgut epithelium. Subsequent conformational changes allow the insertion of their pore-forming portions into the cell membranes to form ion-leakage pores, which cause colloid-osmotic cell lysis, resulting in extensive damage to the midgut and eventual larval death (36,37). However, detailed understanding of the molecular mechanism of action of these toxins remains to be explored, especially the steps of toxin insertion and lytic pore-formation in the target cell membrane.

### 1.5.2 Solubilisation and proteolytic activation

The Cry toxins are present in inclusions as insoluble inactive forms. The first step following the ingestion of *Bt* parasporal crystal bodies is the solubilisation of the crystalline protein inclusions in the alkaline environment of the insect gut to soluble protoxins of 130-140 kDa size. The efficiency of crystal protein solubilisation depends on the environment prevailing in the insect gut and the composition of the parasporal inclusion bodies. Before toxicity can occur, the protoxin must be proteolytically processed. This requires the high pH found in the midgut as well as digestive enzymes from the insect. Activation involved the removal of both the carboxyl terminal and the amino terminal ends of the protein. The proteolytic processing of the Cry toxins can be divided into 2 categories. One is the processing of the large Cry toxins (130 kDa) such as Cry1Aa, Cry4Aa or Cry4Ba. In the large Cry protoxins of ca. 130 kDa, approximately half of the toxin molecule is removed from C terminus during proteolytic activation, leaving the N-terminal half as a toxic fragment. Moreover additional removal of about 30 residues from the N-terminus also occurs (38,39), resulting in a ca. 65-kDa activated toxin. Three-dimensional (3D) models for the 65-kDa activated Cry4Ba toxin were constructed by homology

modeling, based on atomic coordinates of the Cry1Aa and Cry3Aa crystal structures suggested that one site of cleavages occurs in a region before the start of the N-terminal helical bundle and the second cleavage site occurs at Arg<sup>203</sup> in the exposed loop between  $\alpha 5$  and  $\alpha 6$  (40). This interhelical cleavage site has been shown to be critical for cytolytic activity *in vitro* of the Cry4Ba toxin. The second group is the processing of the small Cry toxins of ca. 70 kDa e.g. Cry2Aa, Cry3Aa or Cry11Aa. This processing occurs by cleavages at N-terminus rather than C-terminus that about 50 residues are removed (42,43). However, two stages of processing have been detected for Cry5Aa when the toxin is digested with trypsin or European corn borer (ECB), *Ostrinia nubilalis*, midgut proteases. At first, cleavages at the N-terminal residue 45 and C terminal residue 655 or 659 generate a fully toxic intermediate. Then it is further processed to a partially toxic core, with an N-terminal clip at residue 156 (44).

### 1.5.3 Receptor binding

Once activated, the Cry toxin diffuses from the lumen through the periplasmic membrane into the endoperiplasmic space. The fully processed and active Cry toxin now has access to binding with its receptor in the microvilli of the columnar epithelial cells (45,46). The major threat to the use of Cry toxins is the appearance of insect resistance. The most frequent mechanisms of resistance to Cry toxins are defects on toxin–receptor interactions. For Cry1A toxins (lepidopteran-specific toxins), at least four different protein receptors have been described, a cadherin-like protein [CADR], a glycosylphosphatidyl-inositol (GPI)-anchored aminopeptidase-N (APN), a GPI-anchored alkaline phosphatase (ALP) and a 270 kDa glycoconjugate (47,48,49,50). In addition, it has been proposed that glycolipids are important Cry-receptor molecules in insects and nematodes (51).

Cadherin proteins represent a large family of glycoproteins that are responsible for inter-cellular contacts. These proteins are transmembrane proteins with a cytoplasmic domain and an extracellular ectodomain with several cadherin repeats (49). In the case of CADR of the lepidopteran *Manduca sexta*, it was shown that this protein is located in the microvilli of midgut cells (52). The role of cadherin-like proteins as Cry1A toxin receptor was supported by the selection of a *Heliothis*

*virescens* Cry1Ac-resistant line YHD2 that has a retrotransposon insertion mutation in the cadherin-like gene (53). In addition, the characterisation of CADR alleles in field-derived and in laboratory-selected Cry toxin-resistant strains of the cotton pest *Pectinophora gossypiella* (pink bollworm) revealed three mutated CADR alleles that were associated with Cry toxin resistance (54). The interaction of Cry1A toxins with the CADR receptor is a complex process. Three regions in CADR proteins have been shown to interact with three domain II loop regions.

The aminopeptidase-N (APN) is a GPI-anchored exopeptidase. The APN from various lepidopteran insects were classified into four groups (55). APN1 seems to play an important role in Cry toxin action since a laboratory-selected *Spodoptera exigua* colony resistant to Cry1C did not express APN1, suggesting that the lack of APN production correlated with resistance to the Cry1C toxin (56). Also, inhibition of APN1 production on *S. littura* larvae by dsRNA interference showed that insects with low APN levels became less susceptible to the Cry1C toxin (57). Finally, heterologous expression of *M. sexta* APN1 in midguts and mesodermal tissues of transgenic *Drosophila melanogaster* caused sensitivity to the Cry1Ac toxin (58). The domain III of Cry toxins is involved in the APN–Cry interaction, as shown by the interchange of domain III between Cry1Ac and Cry1Ab toxins (30). Domain III residues of Cry1Aa<sup>508</sup>STRVN<sup>513</sup> and<sup>582</sup>VFTLSAHV<sup>589</sup> were shown to be involved in binding I135-P198 APN fragment (59). In the case of the Cry1Ac toxin, the interaction of domain III and APN is dependent on the sugar *N*-acetylgalactosamine (Gal-NAc). Mutagenesis studies of Cry1Ac domain III identified residues<sup>509</sup>QNR<sup>511</sup>, N506 and Y513 as the amino acid involved in sugar recognition (29). Recently, a GPI-anchored alkaline phosphatase of *M. sexta* was shown to bind Cry1Ac toxin (60). Also, reduced levels of a 65 kDa ALP correlated with resistance of *H. virescens* YHD2 larvae to the Cry1Ac toxin (47). As APN and ALP are both GPI-anchored proteins, these proteins are proposed to be selectively included in lipid rafts that are conceived as spatially differentiated liquid-ordered microdomains in cell membranes. Lipid rafts are enriched in glycosphingolipids, cholesterol and in GPI-anchored proteins and are proposed to be involved in signal transduction, sorting and trafficking of plasma membrane proteins (61). The APN and ALP in *M. sexta* and *H. virescens*, in contrast to the CADR receptors, were shown to be located in lipid rafts (62,63).

The interaction of pore-forming toxins with lipid rafts could result in additional cellular events, including toxin internalisation, signal transduction and cellular response.

Bravo et al (64) provided evidence that binding of monomeric Cry1A-lepidopteran toxin promotes an additional proteolytic activation of the toxin. The exposure of hydrophobic residues facilitates the formation of a pre-pore oligomeric structure. The pre-pore oligomer inserts more efficiently into membrane vesicles, in contrast to the monomeric Cry1Ab, forming stable channels with high probability of an open configuration and is active in bioassays against *M. sexta*, suggesting that the oligomer formation is required for proper toxin insertion into membranes (65). The pre-pore oligomer showed a 200-fold higher affinity [ $0.75 \text{ nM } K_d$ ] to APN receptor than the monomeric structure of the toxin [ $100 \text{ nM } K_d$ ]. The binding to the second receptor, GPI-anchored APN, leads to toxin insertion into lipid rafts membrane (62). Based on these data, we proposed a model that involves the sequential interaction of different toxin structures with CADR and APN in *M. sexta* (**Figure 1.5**).

In the case of Cry11Aa and Cry4Ba toxins, a binding protein of 65 kDa was identified on brush border membrane vesicles from *Stegomyia aegypti* larvae. Data from Buzdin et al (66) showed that this 65-kDa protein is a GPI-anchored ALP protein. In addition, a transmembrane 200-kDa protein that also binds Cry11Aa was described (67), suggesting the presence of multiple Cry toxin receptors in mosquito larvae. Bravo et al (67,68) identified the loop  $\alpha$ -8 region in domain II of Cry11Aa toxin as the binding epitope of this toxin involved in the interaction with ALP from *S. aegypti*. They isolated mutants in loop  $\alpha$ -8 that impaired toxicity and receptor interaction. Site-directed mutagenesis approaches have been used widely to investigate the role of the DII exposed loops of some Cry toxins. Alanine substitutions of residues in the  $\beta$ 10- $\beta$ 11 loop of Cry3Aa showed an increase in larvicidal activity against *Tenebrio molitor*, while no toxicity effect for alanine substitutions in the  $\beta$ 6- $\beta$ 7 loop (69). Deletion of residues in the  $\beta$ 6- $\beta$ 7 or  $\beta$ 10- $\beta$ 11 loops of Cry1Aa almost abolished all toxicity to *Bombyx mori* larvae (70). In addition, some residues in the  $\beta$ 6- $\beta$ 7 and  $\beta$ 10- $\beta$ 11 loops of Cry1Ab, Cry1Ac, Cry1Ca and Cry4Ba were demonstrated to be important for toxicity and receptor-binding interaction (71,72,73,74). More recently, Chayaratanasin et al (75) isolated the C-terminal

domain III from the rest of the Cry4Ba toxin. The results demonstrated that the C-terminal domain III of the Cry4Ba mosquito-larvicidal protein, which can be isolated as a native fold monomer, conceivably participates in toxin-receptor recognition.

However, some Cry toxins needed double mutations in putative surface-exposed loop of its DII to affect their larvicidal activities (72). The identification of receptor molecules and binding epitopes in the toxin and the different receptors will help in the development of strategies to cope with the potential problem of insect resistance. This knowledge will be fundamental for the development of novel toxins with unique specificities and to increase the use of these toxins.

#### **1.5.4 Membrane insertion and pore formation**

After binding to a specific receptor, the Cry toxins insert into the plasma membrane of epithelial cells and form a lytic pore which finally can cause insect death by colloidal osmotic lysis (76). It has been proposed that this lysis occurs via ion flux through holes in lipid bilayers (33,77). At present, the best model explaining the toxicity mechanism of the Cry toxins is the umbrella model (**Figure 1.6**). Briefly, upon binding to specific receptors, the activated Cry proteins has changes their conformation in the lipid membranes, leading to structural rearrangement (78,79). The  $\alpha$ 4- $\alpha$ 5 transmembrane hairpin then inserts into the phospholipid bilayers, while the five other amphipatic helices as well as the rest of the toxin would spread on the surface, following by oligomerisation and pore or channel formation. Feng and Becktel have studied Cry3Aa, Cry1Aa and Cry1Ac by means of size exclusion and found that the relative amounts of monomers and oligomers depended upon temperature, pH or buffer composition (80)(1). Guereca and Bravo have reported that Cry1Aa, Cry1Ac, Cry1Ca, Cry1Da and Cry3Aa toxins formed an oligomer consisting of more than ten units in both neutral and alkaline solution. It also suggested that oligomer formation might be a time-dependent process and might occur after the toxin binds to the receptor and inserts into the membrane (81).

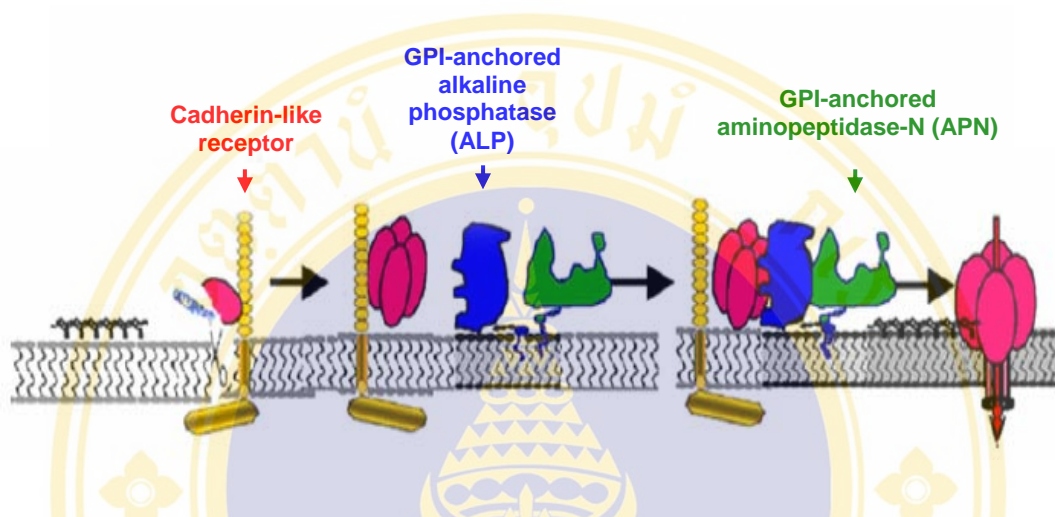


**Figure 1.5 Model of the mode of action of the Cry1A-lepidopteran toxin (62)**

The figure illustrates multiple Cry toxin receptors facilitating the formation of monomer Cry1A toxin to a pre-pore oligomeric structure required for proper toxin insertion into the membrane to APN receptor (yellow color). The binding of pre-pore oligomeric toxin (red color) to the second and third receptor, GPI-anchored ALP (blue color) and GPI-anchored APN (green color), respectively leads to toxin insertion into lipid membrane.

To examine steps or requirements for toxin insertion into the membrane, immunoblotting analysis of the Cry1Ac toxin binding to vesicles isolated from the midguts of *M. sexta* larvae showed that most of the toxin formed a large, antigenic aggregate of ca. 200 kDa. There was one exception, a very active  $\alpha 5$  mutant toxin bound very well to membranes, but no oligomer was detected. In addition, a Cry1Ac mutant containing a mutation in a loop between  $\alpha 2$  and  $\alpha 3$ , had changed in irreversible binding to vesicles, but did not oligomerise. Furthermore, after binding to the vesicles, the Cry1Ac toxin was largely resistant (up to 90%) to digestion with protease K. These results indicated that tight binding of virtually the entire toxin molecule to the membrane and the subsequent oligomerisation are both important steps in toxicity (82).

Mutations in the loop connecting  $\alpha 4$  and  $\alpha 5$  of the Cry1Ac toxin did not affect toxicity for *M. sexta* and *H. virescens* (82,83). In contrast to random mutations in these two helices, which inactivated the toxin but they did not alter in toxin stability, binding of toxin to a membrane protein, and aggregation in the membrane (82). Although helix 5 is reported to be significant for oligomerisation, it might somehow have other functions. Helix 4 was shown to be important in beginning the properties of the channel (25). In the opposite way, the mutations of conserved residues within  $\alpha 5$  of Cry1Ab did not affect oligomerisation but the toxin was able to make pores *in vitro* (24).

Experiments with synthetic peptides of the DI helices demonstrated a role of  $\alpha 7$  in enhancing the insertion of the crucial pore-forming region ( $\alpha 4$ -loop- $\alpha 5$ ) into the membrane. It was found that among seven synthetic peptides corresponding to each individual  $\alpha$ -helix in DI, the  $\alpha 7$ -peptide fragment bound most rapidly to phospholipid vesicles (78). Moreover, the  $\alpha 5$ -peptide fragment was found to be specifically associated with the partially inserted  $\alpha 7$  peptide as well as with itself in a parallel manner within the membrane. This finding was as expected if the pores were formed from several such helices.

In case of the mosquito-toxic Cry4Ba protein, the fragment consisting of  $\alpha 1$ - $\alpha 5$  of Cry4Ba expressed in *E. coli*, after refolding was able to induce glucose permeability of liposome, supporting that the  $\alpha 1$ - $\alpha 5$  fragment constitutes the region responsible for pore-forming activity of the Cry4Ba toxin (87). Single proline

substitutions of residues in the middle of  $\alpha 4$  and  $\alpha 5$  of Cry4Ba directly demonstrated that  $\alpha 4$  and  $\alpha 5$  are important determinants for larvicidal activity, conceivably being involved in membrane penetration and pore formation (26,84). Charged-to-alanine mutagenesis of residues in  $\alpha 4$  of Cry4Ba revealed that the positively charged side-chain of Arg<sup>158</sup> plays a crucial role in toxin activity, possibly being involved in the passage of ions through the toxin-induced pore (88). An analogous effect on toxicity was also observed for Cry1Aa, when charged and polar residues in  $\alpha 4$  were altered (89). Specific mutagenesis studies in the loop connecting  $\alpha 4$  and  $\alpha 5$  of the Cry4Ba toxin revealed an importance of either polar (Asn<sup>166</sup>) or aromatic (Try<sup>170</sup>) residues for its larvicidal activity (90). In addition, recent study showed that both the disulphide bond and the proline-rich motif within the  $\alpha 4$ – $\alpha 5$  long loop of Cry4Aa are structural requirements for larvicidal activity (91). The present study provided evidence that the  $\alpha 4$ – $\alpha 5$  hairpin of Cry4Ba play an important role in membrane perturbing and pore-forming activities (92).

Most recently, Tomimoto et al (93) used a conventional Pronase digestion method and proposed new membrane insertion model for Cry1Aa molecule called “buried dragon model”. It has been revealed that almost whole single molecule of active Cry1Aa penetrates into plasma membrane on the reaction with BBM of midgut epithelial cells, suggesting the stretch of  $\alpha$ -2 to  $\alpha$ -7 and of  $\beta$ -6 to domain III were buried or strongly interacted with BBMV.

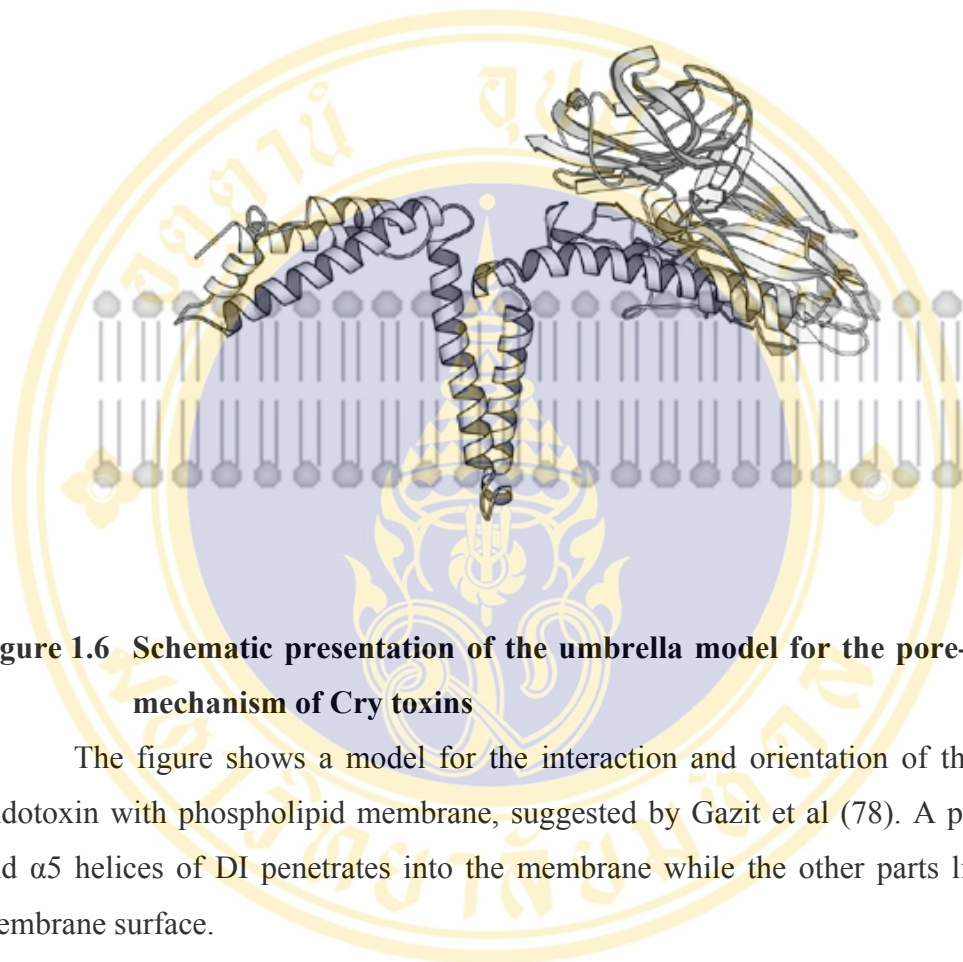


**Figure 1.6 Schematic presentation of the umbrella model for the pore-forming mechanism of Cry toxins**

The figure shows a model for the interaction and orientation of the Cry  $\delta$ -endotoxin with phospholipid membrane, suggested by Gazit et al (78). A pair of  $\alpha 4$  and  $\alpha 5$  helices of DI penetrates into the membrane while the other parts lie on the membrane surface.

## 1.6 Attenuated total reflection-fourier transform infrared ATR-FTIR spectroscopic studies of toxin-membrane interaction

There are a number of techniques that can provide information on protein structures. Undoubtedly, X-ray crystallography and two-dimensional nuclear magnetic resonance (NMR) spectroscopy are the most powerful towards this end. These two techniques can provide a most detailed structure of proteins. Fourier transform infrared spectroscopy (FTIR) is also becoming accepted as an increasingly useful tool for the structural analysis of proteins. There are a number of advantages that make IR spectroscopy an attractive tool for the structural studies of proteins or peptides. Probably the single most important advantage of FTIR spectroscopy is that the spectra of peptides can be obtained in such a wide range of environments. Thus, conformational changes of a peptide can be readily followed as a function of altering its environment. This is an important advantage of FTIR spectroscopy in light of the increasing evidence that a variation of the environment can be important in determining the secondary structure of a peptide. Hence FTIR spectroscopy offers the possibility of identifying the most physiologically relevant conformation of a peptide or protein.

It has a particular advantage for membrane-associated peptides and proteins over techniques such as NMR or crystallography. Furthermore, unlike some spectroscopic techniques such as electron spin resonance (ESR), FTIR spectroscopy does not rely on the external probe molecules, which may introduce artifacts. The time scale of the NMR and ESR are  $10^{-5}$  s and  $10^{-8}$  s, respectively, while IR spectroscopy provides a fast snapshot ( $10^{-12}$  s) of the peptide structure. Thus, interpretation of experimental data are not complicated (94).

ATR-FTIR spectroscopy is one of the popular techniques for collecting IR spectra of biological materials in general, and for biological membranes in particular. Most of membrane proteins or peptides contain sufficient atoms to give rise to approximately  $10^4$  vibrational modes. Particularly, in addition to the modes arising from the peptide backbone and the amino acid side chains, there can be contributions from their surrounding environments such as  $H_2O$ , buffer, and lipids present in the sample. Information can be obtained not only on a secondary structure, but also on the

orientations of membrane molecules from measurements with polarised light using only sub-milligram quantities of materials.

### 1.6.1 Principle of ATR-FTIR spectroscopy

Most commonly, IR spectroscopy is performed in the transmission experiment, in which the IR radiation passes directly through the sample. The absorbance is defined as

$$A = -\log(I/I_0),$$

and is calculated from the intensities of transmitted and incident light,  $I$  and  $I_0$ , respectively. The ratio  $T = I/I_0$  is called the transmittance. The absorbance is directly proportional to the concentration ( $c$ ) of the absorbing molecules and the path length ( $l$ ) of the measuring cell (Beer-Lambert's law)

$$A = \epsilon cl$$

where  $\epsilon$  is the molar extinction coefficients. Two important factors have to be considered in transmission IR spectroscopy of aqueous solutions of proteins. First, the vibrational extinction coefficients are generally relatively low (e.g. a few hundred  $M^{-1}cm^{-1}$  for the amide I mode). Second, protein samples require  $H_2O$  to be present, and the strong  $H_2O$  absorbance obscures too much of the IR spectrum and overlap with several of interest bands of interest in protein and membrane spectroscopy. To minimise these problems, relatively high protein concentrations ( $\geq 1$  mg/ml) and short path lengths are used in transmission FTIR spectroscopy. The excellent performance of FTIR spectrometers allows for accurate background subtraction and reliable recording of the protein spectra in aqueous solutions, which is not possible with the older, dispersive instruments.

One way to overcome the strong absorption of  $H_2O$  is the application of the attenuated total reflection (ATR) technique (**Figure 1.7**). In this technique, the IR beam is internally reflected within an IR-transparent internal reflection element. An evanescent wave of the same frequency as the incoming IR light is set up in the optically rarer medium, such as an aqueous solution that is adjacent to the interface. The decay of an intensity of the wave is an exponential function of amplitude of the electric field ( $E$ ) and distance ( $z$ ) from the interface.

$$E = E_0 e^{-z/d_p}$$

with a characteristic decay length (depth of penetration),

$$d_p = \frac{\lambda / n_1}{2\pi \sqrt{[\sin^2 \gamma - (n_2 / n_1)^2]}}$$

here  $d_p$  = penetration depth,  $\lambda$  = wavelength,  $n_1$  = a refraction index of the IRE,  $n_2$  = a refraction index of the sample, and  $\gamma$  = an angle of incidence. Because  $d_p$  is of an order of only a few hundred nm in many typical applications, an internal reflection spectroscopy is a surface-sensitive technique. Samples, such as membranes, that are deposited at the solid-liquid (or solid-gas) interface absorbed the electromagnetic radiation of the evanescent wave, and thereby reduced the intensity of the reflected light. Hence, this technique is referred to as 'attenuated total reflection spectroscopy'. A major advantage of ATR spectroscopy is that absorption due to H<sub>2</sub>O and other molecules in the bulk solution is greatly reduced. Another advantage is that molecular orientations can be determined in oriented samples with polarised light.

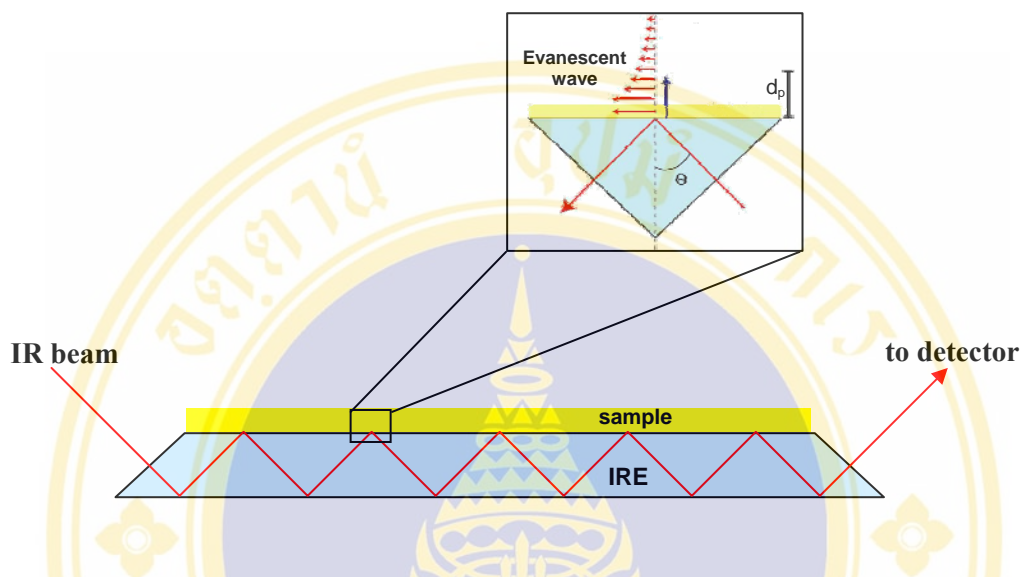


**Figure 1.7 Geometric configuration of an ATR set up (95)**

The IR beam is internally reflected through an internal reflection element (IRE). The sample deposited on the IRE has a different index of refraction and mismatch results in leakage of some IR radiation into the sample as an evanescent wave. This evanescent-wave IR radiation is absorbed by vibrational modes in the sample. The inset in the figure illustrates the penetration of the evanescent wave, which decays exponentially to zero from the surface of the IRE.

### 1.6.2 Conformation and orientation determinations of membrane-bound peptides

ATR-FTIR spectroscopy has become an important tool to determine the conformation and orientation of membrane-bound peptides (95). Spectral interpretation of peptides containing relatively short amino acid sequences is quite straightforward. An effect of small amino sequences on the spectral parameters can be easily assessed by chemically synthesising of variant peptides carrying altered sequences. In addition, this method requires only small amounts of materials. It does not depend on introducing spectroscopic probes and light scattering artifacts or limited by the size of the material. Therefore, FTIR spectroscopy can be applied to peptides in solution, detergent micelles, or lipid bilayers, which allows to investigate structural changes of peptides in their native environment. By using this technique, key molecular mechanistic details of some membrane proteins have been gathered (95). Many ATR-FTIR studies have performed to understand protein-lipid associations and visualise the properties of peptides or proteins in membrane system (78,96,97,98,99,100,101). In addition, spectroscopic studies using an isotopic label/probe ( $C^{13}=O^{18}$ ) at specific sites in the protein have been used because it can reflect on particular properties of the protein. This method is based upon the incorporation of an isotopic label in the peptide and examined the resulting shifted peak by polarised infrared spectroscopy (102). Thus far, this probe was still used to study or to determine helix tilt and rotational orientation of peptides in membrane environment (103,104,105,106,107,108). Moreover, Getahun et al (109) have shown that nitrile-derivatised amino acids could be used as infrared environmental probes, because this probe can be used to provide detailed information regarding the interaction between peptides and membranes, especially the hydration state and orientation of individual side chains (110).

## CHAPTER II

### OBJECTIVES

Although several crystal structures of different Cry  $\delta$ -endotoxins from *Bacillus thuringiensis*, including Cry4Ba (21), have been elucidated, little is known about the structural changes during toxin insertion into the lipid membrane. Thus far, the umbrella model seems to be the best description for the membrane-associated state of the Cry toxins, which involves an insertion of  $\alpha$ 4 and  $\alpha$ 5 into the lipid membrane as a helical hairpin whilst the remaining helices are rearranged to spread on the membrane surface (36,78). A refined model further suggested that  $\alpha$ 7 may serve as a binding sensor that could initiate the binding of the pore-forming domain to the lipid membrane, facilitating the membrane insertion of the  $\alpha$ 4- $\alpha$ 5 hairpin (78).

Although helix 7 has also been implicated in ion-channel activity and receptor-binding affinity of Cry1A toxins (23,85), structural stability and crystallisation of Cry3Aa (86), or a kink introduced by proline substitution at Thr<sup>254</sup> located in the middle of helix 7 was shown to significantly decrease larvicidal activity of the Cry4Ba toxin (84), the functional importance for toxicity of the structurally conserved aromaticity in this helix has not been clearly highlighted. Due to several studies, the aromatic residues could play several different roles in membrane-protein interactions, depending on their location and side-chain orientation (111,112,113,114). For example, alanine substitutions of aromatic side chains (Trp<sup>19</sup>, Trp<sup>61</sup>, Phe<sup>64</sup>) of phospholipase A<sub>2</sub> from the Chinese cobra venom (*Naja naja atra*) were shown to influence interfacial binding (111). Also, replacements of all the five Phe residues with Ala in the MARCKS peptide, one of the major substrates for protein kinase C, revealed a significant decrease in binding of the peptide to membrane vesicles (112). From amino acid sequence alignments,  $\alpha$ -helix 7 of domain I contains four conserved aromatic residues, W<sup>243</sup>, F<sup>246</sup>, Y<sup>249</sup> and F<sup>264</sup>. The objective

of this thesis was therefore to characterise the function of these four aromaticity in the Cry4Ba toxin (**Figure 2.1**) by using substitution analysis, liposome perturbation assay, ATR-FTIR spectroscopy and molecular dynamics simulations.



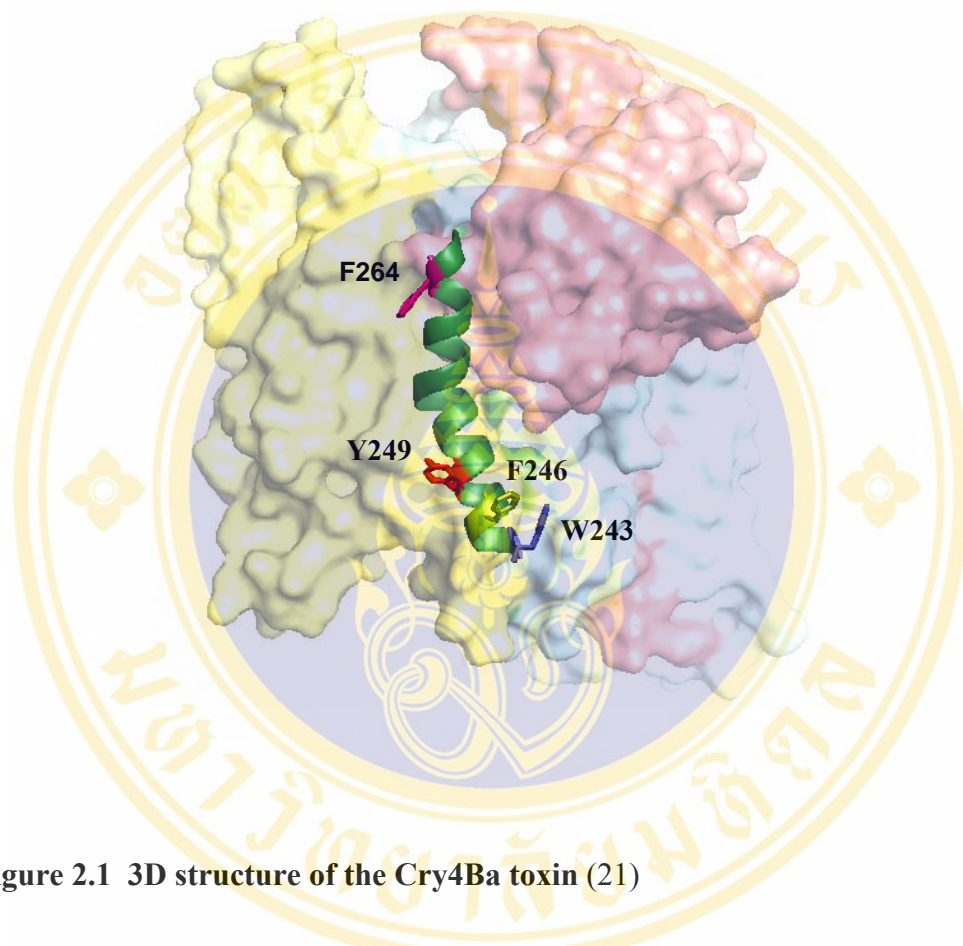


**Figure 2.1** 3D structure of the Cry4Ba toxin (21)

The figure shows the 3D structure of the 65-kDa activated Cry4Ba toxin, showing the three-domain organisation (I-III). Domain I is illustrated in a yellow surface, while domain II and domain III are shown in blue and red surface color. Positions of the secondary structure of Cry4Ba-helix 7, including ball and stick of conserved aromaticity, W243 (blue), F246 (green), Y249 (red) and F264 (pink) are also illustrated.

## CHAPTER III

### MATERIALS AND METHODS

#### 3.1 Materials

##### 3.1.1 Chemicals and reagents

Ampicillin	Sigma
Calcein	Molecular Probes
Cetyl trimethyl ammonium bromide (CTAB)	Sigma
Chloroform	Merck
Cholesterol (purity>98%, wool grease)	Avanti polar-lipids, Inc
Coomassie brilliant blue R-250	Sigma
Dimethylsulfoxide (DMSO) (synthesis grade)	Merck
1, 2-Dimyristoyl- <i>sn</i> -glycero-3-phosphocholine (DMPC)	Avanti polar-lipids, Inc
1,2-Dimyristoyl- <i>sn</i> -glycero-3-phosphocholine (DMPG)	Avanti polar-lipids.Inc
1,2-didecanoyl- <i>sn</i> -glycero-3-phosphocholine (DDPC)	Avanti polar-lipids.Inc
1, 4-Dithiothreitol (DTT)	Sigma
D <sub>2</sub> O, 99.9% deuterium atom	Aldrich
Isopropyl- $\beta$ -D-thiogalactopyranoside (IPTG)	Sigma
L- $\alpha$ -Phosphatidylcholine (egg)	Avanti polar-lipids, Inc
L- $\alpha$ -Phosphatidylethanolamine (egg)	Avanti polar-lipids, Inc

All other unlisted chemicals and reagents are analytical grade purchased from various suppliers.

##### 3.1.2 Enzymes and accessory buffers

<i>Pfu</i> DNA polymerase (cloned)	Promega
Trypsin (bovine pancreas, TCPK treated)	Sigma

### Restriction endonucleases

Promega

All restriction endonuclease enzymes and their buffers were commercially provided by specified companies.

### 3.1.3 Bacterial strain

*E. coli* strain JM109 [*recA1 supE44 endA1 hsdR17 gyrA96 rclA1 thiΔ*/(*lac-pro AB*) F'(*traD36 proAB<sup>+</sup> lacI<sup>q</sup> lacZΔM15*)] was purchased from Promega.

### 3.1.4 Recombinant plasmid

pMU388 (Figure 3.1) the recombinant plasmid containing the full length of the *cry4Ba* gene, which has been cloned from *Bt* subsp. *israelensis* was used as a DNA template for site-directed mutagenesis.

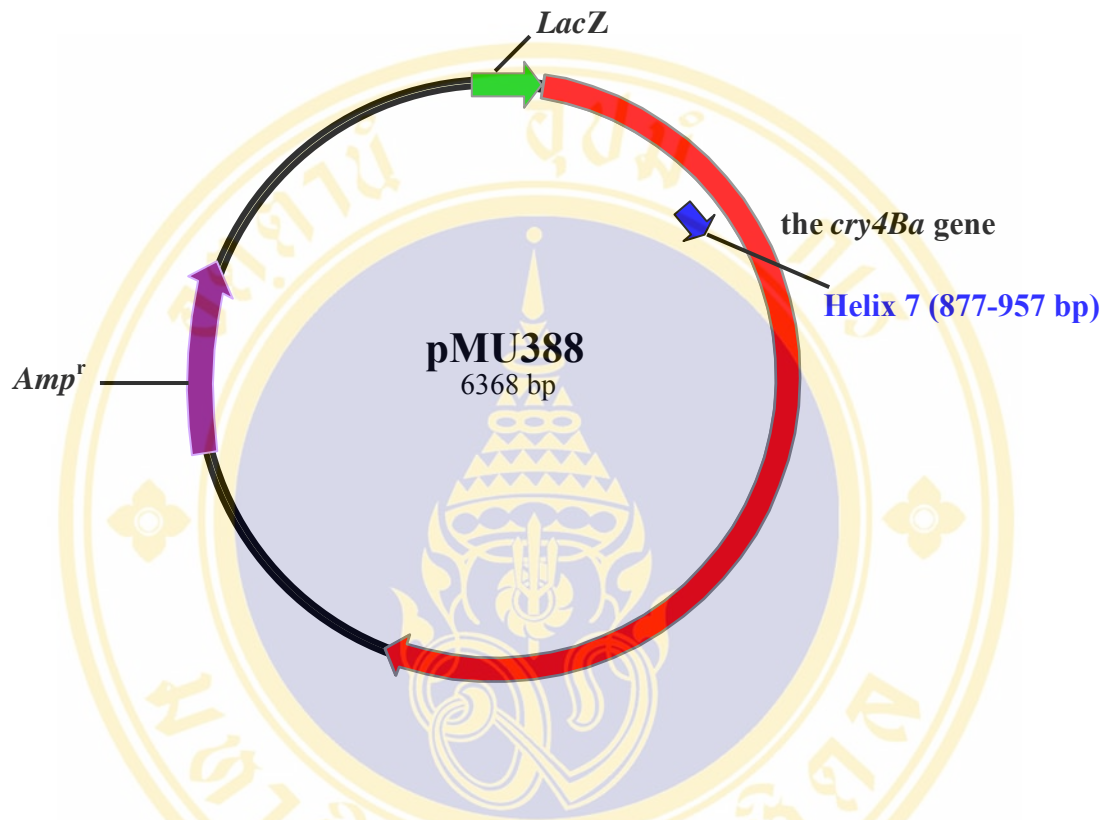
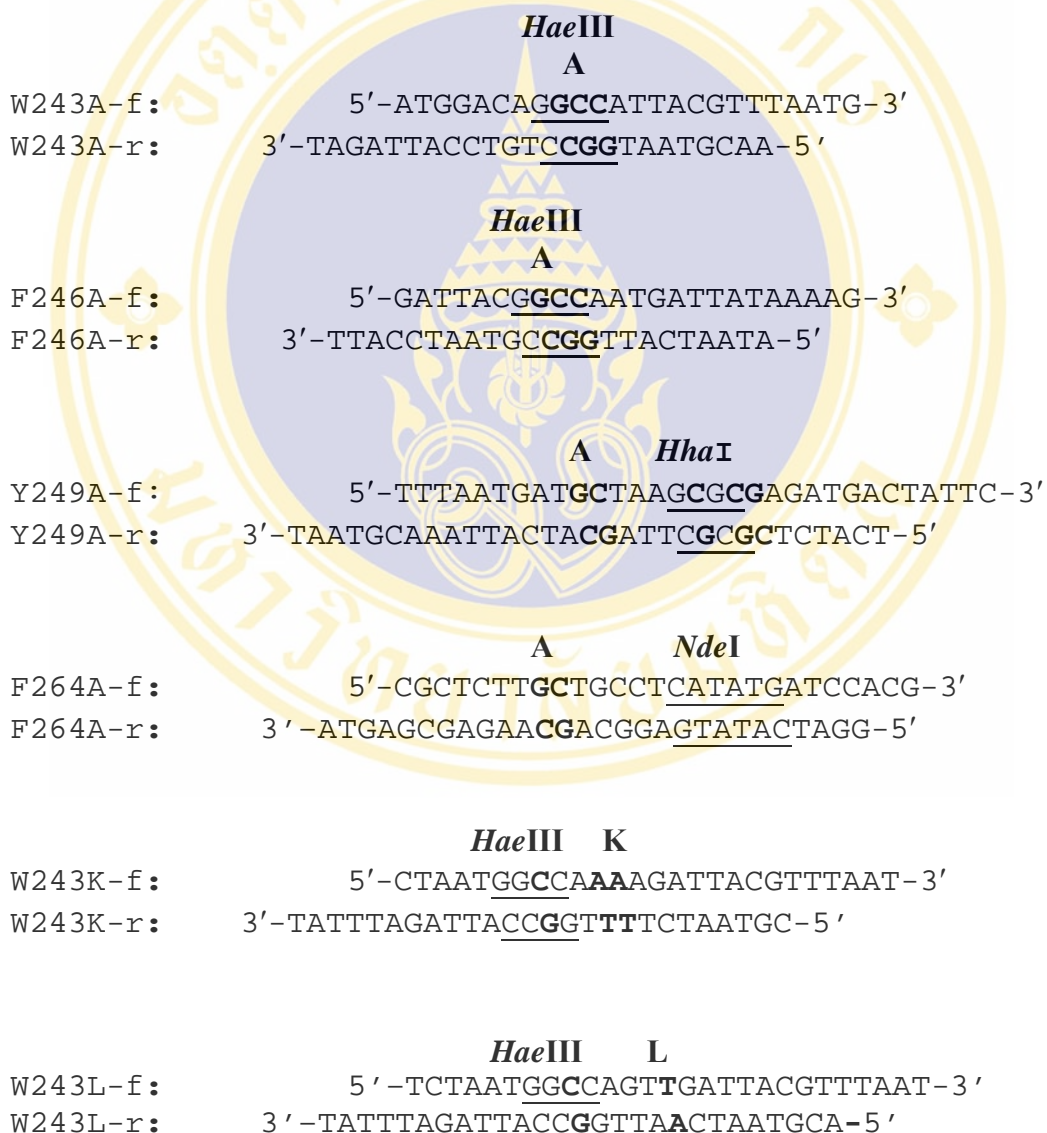


**Figure 3.1 Physical map of the plasmid pMU388**

The figure shows the plasmid-pMU388, containing the *LacZ* promoter driving the expression of the gene encoding the 130-kDa full-length Cry4Ba toxin. *Amp<sup>r</sup>* gene and  $\alpha 7$  within the pore-forming domain I is shown in violet and blue.

### 3.1.5 Oligonucleotide primers

All mutagenic oligonucleotide primers were purchased from Proligo Inc. (Singapore). The sequences of these oligonucleotides are shown below. Single letter codes for amino acid were placed above their corresponding nucleotide sequences. Introduced restriction endonuclease recognition sites are underlined. The bold letters indicate mutated nucleotides or amino acid residues.



**HaeIII F**

W243F-f: 5'-CTAATGGCCAATTTATTACGTTTAATG-3'  
 W243F-r: 3'-TATTTAGATTACCGGTTAAATAATGCAA-5'

**E HhaI**

Y249E-f: 5'-TTTAATGATGAAAAGCGCGAGATGACTATTC-3'  
 Y249E-r: 3'-TAATGCAAATTACTACTTTTCGCGCTCTACT-5'

**R HhaI**

Y249R-f: 5'-TTTAATGATCGTAAGCGCGAGATGACTATTC-3'  
 Y249R-r: 3'-AATGCAAATTACTAGCATTTCGCGCTCTACT-5'

**H HhaI**

Y249H-f: 5'-TTTAATGATCATAAGCGCGAGATGACTATTC-3'  
 Y249H-r: 3'-TAATGCAAATTACTAGTATTTCGCGCTCTACT-5'

**F HhaI**

Y249F-f: 5'-TTAATGATTTTAAGCGCGAGATGACTATTC-3'  
 Y249F-r: 3'-AATGCAAATTACTAAAATTTCGCGCTCTACT-5'

**W HhaI**

Y249W-f: 5'-TTAATGATTGGAAGCGCGAGATGACTATTC-3'  
 Y249W-r: 3'-AATGCAAATTACTAACCTTTCGCGCTCTACT-5'

**L HhaI**

Y249L-f: 5'-TTTAATGATCTTAAGCGCGAGATGACTATTC-3'  
 Y249L-r: 3' TAATGCAAATTACTAGAAATTTCGCGCTCTACT 5'

**XbaI****E**

F264E-f: 5'-CGCTCTAGAGGCCAGTTATG-3'  
 F264E-r: 3'-ATGAGCGAGATCTCCGGTCA-5'

**R NdeI**

F264R-f: 5'-TCGCTCTT**CGTGCCTCATATGATCCACG**-3'  
 F264R-r: 3'-TATGAGCGAGAAG**CACGGAGTATACTAGG**-5'

**EcoRV H**

F264H-f: 5'-GTATTAGATAT**CCTCGCTCTTCATGCCAGTTATGA**-3'  
 F264H-r: 3'-G TTCATAATCTATAG**GAGCGAGAAGTACGGTCAAT**-5'

**Y NdeI**

F264Y-f: 5'-CGCTCTTT**ATGCCTCATATGATCCACG**-3'  
 F264Y-r: 3'-ATGAGCGAGAA**ATACGGAGTATACTAGGA**-5'

**Sau96I**

**W**

F264W-f: 5'-CGCTCTTT**GGGCCAGTTATGAT**-3'  
 F264W-r: 3'-ATGAGCGAGAA**ACCCGGTCAAT**-5'

**Sau96I L**

F264L-f: 5'-TAGATATACT**GGCCCTTTTAGCCAGTTATGAT**-3'  
 F264L-r: 3'-CATAATCTATATG**ACCGGGA**AAATCGGTCAAT-5'

**Sau96I L**

Y249L/F264L-f: 5'-AGATATACT**GGCCCTTCTTGCCAGTTATGAT**-3'  
 Y249L/F264L-r: 3'-TTCATAATCTATATG**ACCGGA**AGAACGGTC-5'

**A HhaI**

F264A/Y249A-f: 5'-GTTTAATGAT**GCTAAGCGCG**GAGATGACTATTC-3'  
 F264A/Y249A-r: 3'-TAATGCAAATTACTAC**GATT**CGCGCTCTACTG-5'

### 3.1.6 Culture media

#### Luria-Bertani (LB) broth and agar (115)

1 L of LB broth contains 10 g casein hydrolysate, 5 g bacto-yeast extract and 5 g NaCl. LB agar was prepared by adding 10 g bacto-agar in 1 L of LB broth. The mixture was autoclave at 121°C, 15 p.s.i. for 20 min. For LB broth, 100 µg/ml ampicillin was added before used and for LB agar, 100 µg/ml ampicillin was added after the medium cool to 60°C. Approximately 20 ml of the sterilised medium was poured into culture plates. The plates were left at room temperature until solidified. The agar plates were stored in 4°C until used.

### 3.1.7 Phosphorus content analysis solution

#### Ammonium molybdate-H<sub>2</sub>SO<sub>4</sub> solution (100 ml)

Ammonium molybdate	4.31	g
H <sub>2</sub> SO <sub>4</sub>	28	ml
dH <sub>2</sub> O	72	ml

Ammonium molybdate was dissolved well in H<sub>2</sub>O and then added with H<sub>2</sub>SO<sub>4</sub>. This solution should be prepared in prechilled container.

#### Phosphorus content assay solution (25 ml)

Ascorbic acid	0.38	g
dH <sub>2</sub> O	23	ml
Ammonium molybdate-H <sub>2</sub> SO <sub>4</sub> solution	2	ml

This solution should be prepared freshly before assay.

### 3.1.8 Chromatographic columns

Analytical RP-HPLC column Jupiter C <sub>18</sub> (250x4.6 mm)	Phenomenex, USA.
Analytical RP-HPLC column ZORBAK 300SB-C <sub>18</sub> (250x4.6 mm)	Agilent, USA.
Semi-preparative RP-HPLC column ZORBAK 300SB-C <sub>18</sub> (250x10 mm)	Agilent, USA.
HiTrap™ desalting column	Amersham Pharmacia Biotech
Superdex 200 HR 10/30 column	Amersham Pharmacia Biotech

### 3.1.9 Miscellaneous

15 and 50 ml centrifuge tube (polypropylene)	CORNING®
96 well-flat bottom plate	Maxi®sorb, NUNC
Broad range protein marker (65-200 kDa)	Bio-Rad
Geldoc® system	Bio-RAD
GeneAmp PCR System 2400 thermal cycler	Perkin-Elmer
Jasco J-715 spectropolarimeter	Jasco Inc
Mega™BACE 500 DNA sequencing system	Amersham Bioscience
Spectra MAX 250 ELISA plate reader	Molecular Device
UV 1601 spectrophotometer	Shimadzu

All accessories, i.e. Nicolet Nexus 470 spectrometer, MCT/A detector, germanium (Ge) internal reflection element for ATR-FTIR experiments was kindly provided by Assoc. Prof. Jaume Torres (School of Biological Science, Nanyang Technological University, Singapore).

## 3.2 Methods

### 3.2.1 Plasmid extraction by CTAB method (115)

A single colony of recombinant *E. coli* was inoculated into 3 ml LB broth containing 100 µg/ml ampicillin. After overnight culture at 37°C with shaking at 200 rpm, the cell culture was transferred to a 1.5 ml microcentrifuge tube. The cells were collected by centrifugation at 12,000 rcf for 10 sec. The pellet was resuspended in 200 µl STET buffer (8% sucrose, 0.1% Triton X-100, 50 mM EDTA and 50 mM Tris-HCl, pH 8.0) and 5 µl of freshly prepared lysozyme solution (10 mg/ml). The mixture was kept at room temperature for 10 min and then boiled for 45 sec and immediately centrifuged at 10,000 rcf for 15 min. The pellet containing cell debris and chromosomal DNA was carefully removed with toothpick. Plasmids and low molecular weight residual DNAs were recovered by adding 5% CTAB into supernatant fraction to give 1/10 (v/v) of CTAB. The solution was mixed by vortexing and centrifuged at 10,000 rcf for 5 min. The pellet was suspended in 300 µl of 1.2 M NaCl by vigorously vortexing. In order to eliminate RNA, 5 µl RNase A (20 mg/ml) was added into the plasmid solution and incubated at 37°C for 30 min. Proteins were removed by adding an equal volume of chloroform, mixed and centrifuged at 10,000

ref for 5 min. Plasmid DNA was precipitated by adding two volume of ethanol and kept at  $-20^{\circ}\text{C}$  for 30 min. The mixture was centrifuged at 10,000 rcf for 15 min to pellet DNA, then the pellet was washed with 70% ethanol, air dried and dissolved in 20  $\mu\text{l}$  of sterilised distilled  $\text{H}_2\text{O}$ .

### 3.2.2 Agarose gel electrophoresis of DNA

Agarose gel electrophoresis was performed according to Sambrook et al (115). Agarose powder was dissolved in TBE buffer (89 mM Tris-HCl, 89 mM boric acid, 25 mM EDTA, pH 8.0) to obtain 1% (w/v) agarose gel. After boiling to ensure the homogeneity of the gel solution, the gel mixture was cooled down and poured into the mold to solidify at room temperature. Gel loading dye (0.1% bromophenol blue, 15% (w/v) Ficoll 400, 50 mM EDTA) was mixed with DNA in a ratio of 1:5 (v/v) and then the mixture was loaded into a well of the agarose gel submerged in TBE buffers. After electrophoresis setting constant voltage at 100 V was completed, the gel was stained in 2  $\mu\text{g}/\text{ml}$  ethidium bromide solution for 5 min and destained in  $\text{H}_2\text{O}$  for 10 min. The DNA bands were visualised under UV light by the Geldoc® system. The amount of DNA was estimated by comparing the stained DNA band with standard DNA markers of known concentration under UV light (200 ng of total known DNA).

### 3.2.3 Site-directed mutagenesis

The method used was PCR-based according to Stratagene's QuikChange site-directed mutagenesis kit (see **Figure 3.2**). The recombinant plasmid-pMU388 (see **section 3.1.4**) was used as a template and a pair of complementary mutagenic primers (see **section 3.1.5**) were added to PCR tube containing optimised buffer for *Pfu* DNA polymerase. The amplification of *cry4Ba* carrying a mutated residue was accomplished by the use of *Pfu* DNA polymerase which replicates both strands of DNA plasmid with high fidelity without displacing the mutant oligonucleotide primers.

### 3.2.4 PCR conditions

An automated GeneAmp PCR System 2400 thermal cycler (Perkin-Elmer, CA, USA) was used to perform PCR for all samples as conditions shown in **Table**

**3.1.** The reaction mixture (50  $\mu$ l) is composed of

DNA template	100 ng
dNTP	50 $\mu$ M each
Forward primer	10 pmol
Reverse primer	10 pmol
10x <i>Pfu</i> buffer	5 $\mu$ l
<i>Pfu</i> DNA polymerase	2.5 U
Sterilised distilled H <sub>2</sub> O was added to make final volume to 50 $\mu$ l.	

**Table 3.1 Temperature cycling parameters for site-directed mutagenesis**

Temperature ( $^{\circ}$ C)	Time (min:sec)	Cycles
95	1:00	1
95	0:30	25
*T <sub>a</sub>	1:30	
68	13:00	
68	7:00	1
4	HOLD	

\* The annealing temperature (T<sub>a</sub>) are shown in Table 3.2

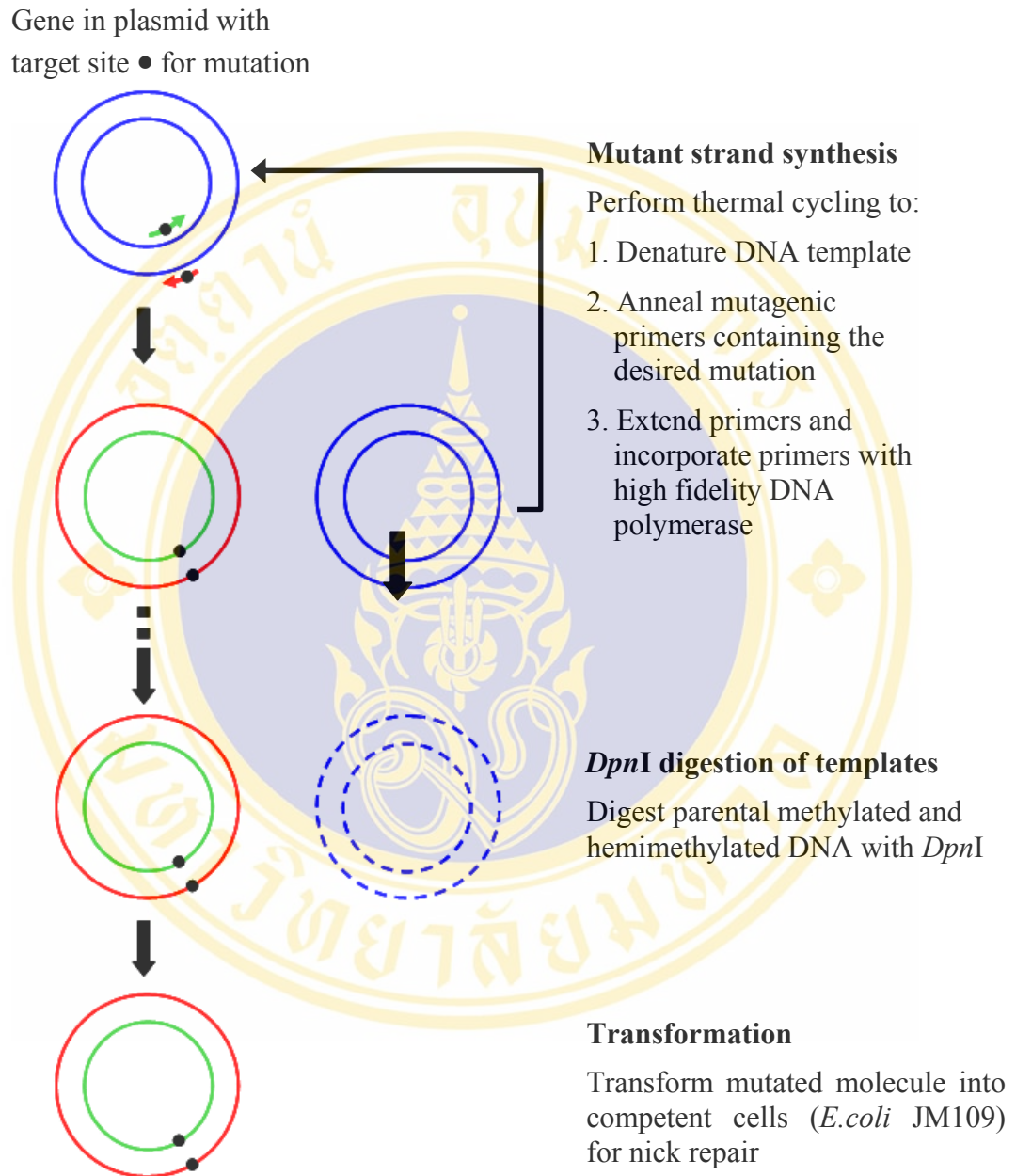


**Figure 3.2 Site-directed mutagenesis method**

The figure shows site-directed mutagenesis method redrawn from Stratagene's QuikChange instruction manual.

**Table 3.2 Annealing temperature ( $T_a$ ) for each mutant**

<b>Mutants</b>	<b>Annealing Temperature (<math>T_a</math>)</b>
W243A	45
F246A	45
Y249A	45
F264A	45
W243K	49
W243L	49
W243F	50
Y249E	50
Y249R	50
Y249H	50
Y249F	50
Y249W	50
Y249L	49
F264E	50
F264R	50
F264H	52
F264Y	52
F264W	52
F264L	49
Y249L/F264L	50
F264A/Y249A	50

The amino acid substitution was performed. When the amplification reaction was finished, the PCR products were examined for the presence of amplified DNA on 1% agarose gel electrophoresis.

### 3.2.5 *DpnI* digestion of PCR products

Each PCR amplified reaction was mixed with *DpnI* restriction endonuclease. DNA isolated from almost all *E. coli* strains, is *dam* methylated and it would be therefore susceptible to *DpnI* digestion. *DpnI* restriction endonuclease is specific for methylated and hemimethylated DNA (5'-G<sup>me</sup>A↓TC-3'). After enzyme digestion, only a newly synthesised DNA was resistant to the digestion and subsequently transformed into *E. coli* competent cells.

### 3.2.6 Competent cell preparation using calcium chloride method (115)

A single isolated colony of *E. coli* strain JM 109 was inoculated into 3 ml of LB broth containing 100 mg/ml ampicillin and incubated at 37°C with 200 rpm shaking for 16 h. An overnight culture was inoculated into fresh LB broth to obtain 1% of cell concentration and then incubated further until OD<sub>600</sub> was between 0.3-0.5. When OD<sub>600</sub> of culture approached 0.4, cell culture was chilled on ice for 10 min. Cells were harvested by centrifugation at 2,000 rcf for 10 min at 4°C. The medium was decanted from a cell pellet as much as possible and then the cell pellet was resuspended gently in one-third of the original volume with ice-cold 0.1 M CaCl<sub>2</sub> and stored on ice for 1 h. Cells were recovered by centrifugation at 2,000 rcf for 10 min at 4°C and the pellet was suspended in 2 ml of ice-cold 0.1 M CaCl<sub>2</sub> for 50 ml of original culture. Cells were either directly used for transformation or dispersed into 200 µl aliquots and kept at -80°C. For long-term storage, glycerol was added into the competent cell suspension to give a 30% (v/v) final concentration.

### 3.2.7 Plasmid DNA transformation (115)

50 ng *DpnI*-digested PCR product was mixed with 200 µl of competent cells. The mixture was immediately chilled on ice for 30 min, following by heating at 42°C for 90 sec, and then immediately placed on ice for 5 min. 800 µl of LB broth was added into the transformed cells, gently mixed and incubated at 37°C for 1 h. Transformed cells were collected by centrifugation at 5000 rcf for 2 min. The cell

pellet was gently resuspended with 200  $\mu$ l of LB broth. The transformed cell suspension was gently spread on LB agar plate containing 100  $\mu$ g/ml of ampicillin. The agar plate was incubated at 37°C for 16-20 h until *E. coli* colonies were clearly seen on agar plate.

### 3.2.8 Restriction endonuclease analysis (115)

Restriction endonuclease analysis was used to screen a mutant plasmid based on the recognition site, silently introduced into each pair of mutagenic oligonucleotide primers. 20  $\mu$ l of digestion reaction contains about 0.5-1  $\mu$ g of DNA sample, digestion buffer, and approximately 5 U of restriction endonuclease and sterilised distilled H<sub>2</sub>O to make up to the 20  $\mu$ l total volume. The digestion reaction was incubated at 37°C for 2 h with appropriate enzymes. Appropriate restriction enzyme digestion buffers were used following manufacturers. To visualise the restriction patterns, electrophoresis of the digested DNA was carried out in a horizontal 1% agarose gel in TBE buffer at 100 V at least 1 h and subsequently stained with ethidium bromide.

### 3.2.9 DNA sequencing analysis

To confirm the resultant mutation, the ABI PRISM™ Sequencing Kit was used to prepare samples for sequence analysis based on fluorescent-labeled terminator cycle sequencing. The PCR reaction was performed in 20  $\mu$ l of a mixture containing 4  $\mu$ l of Terminator Premix (A-Dye Terminator, C-Dye Terminator, G-Dye Terminator, T-Dye Terminator, dATP, dCTP, dTTP, dITP, Tris-HCl (pH 9.0), MgCl<sub>2</sub>, thermal stable pyrophosphatase, and AmpliTaq DNA polymerase). 300 ng of plasmid DNA template, 10 pmole of oligonucleotide primers, N195A-f was used as a sequencing primer for all mutants. The reaction mixture was carried out in an automated thermal cycle with the following conditions

96°C	3 min	1 cycle
96°C	10 sec, 60°C 4 min	20 cycles
60°C	7 min	1 cycle

After completion of the PCR reaction, the PCR product was recovered by the ethanol precipitation. The dye-label-PCR product was analysed on the ABI PRISM™ 377 automated DNA sequencer.

### 3.2.10 Toxin expression

A single colony of *E. coli* strain JM109 containing the wild-type pMU388 plasmid or its derivatives was inoculated into 3 ml of LB broth containing 100 µg/µl ampicillin at 37°C and 250 rpm shaking for 16-20 h. The overnight culture was transferred into a new flask containing 700 ml LB broth and 100 µg/ml ampicillin to make up 1% of the final concentration. The cultures were further incubated at 37°C until OD<sub>600</sub> reached 0.4-0.5. An expression was induced by adding IPTG to a final concentration of 0.1 mM for 10 h at 30°C. 0.1 OD<sub>600</sub> of the *E. coli* culture (ca. 10<sup>7</sup> cells) was subjected to analysis on SDS-polyacrylamide gel electrophoresis (PAGE).

### 3.2.11 Toxin inclusion purification

Cells expressing the mutant toxins as inclusion bodies were harvested by centrifugation and suspended in 30 ml of distilled water. The cell suspension was disrupted by using a French Press Cell at 10,000 psi. The crude lysate was centrifuged at 6000 rcf, 4°C for 10 min. The pellets were washed 3 times with cold distilled water. Protein concentrations of the partially purified toxin inclusions were determined by using the Bradford-based protein microassay (Bio-RAD), with bovine serum albumin fraction V (Sigma) as a standard (116).

The calibration curve was constructed from a standard protein, bovine serum albumin (BSA). BSA standards were prepared by making dilution ranging from 0, 1, 2, 3, 4 and 5 µg/ 50 µl BSA in distilled H<sub>2</sub>O. Each standard protein solution was mixed with 200 µl of 1:4 (v/v) diluted dye (Bradford reagent) in distilled H<sub>2</sub>O. The solution was mixed in a 96-well flat bottom Sero-Wel microtitre plate (Bibby Sterilin, England) and incubated at room temperature for 10 min before measuring an absorbance at 595 nm on the SpectraMAX 250 ELISA plate reader (Molecular Device). 50 µl of diluted inclusion proteins were used and the protein concentrations of samples were calculated from the standard curve.

### 3.2.12 SDS-PAGE analysis (114)

Protein sample was prepared by mixing the sample with 4X loading buffer (60 mM Tris-HCl pH 7.5, 2% of SDS 10% glycerol, 0.025 % bromophenol blue, 100 mM DTT) in 3:1 (v/v) ratio and boiled at 100 °C for 5 min. The heated samples were vigorously mixed using vortex and centrifuged at 10,000 rcf for 10 min to precipitate any insoluble materials. Supernatant equivalent to 0.1 OD of the cell culture was loaded into each well for SDS-PAGE analysis. The SDS-PAGE was performed using the Bio-Rad Mini-Protein III system. The gel system in SDS-PAGE is composed of separating and stacking gels. The separating gel is consisted of 3% crosslinker 10%, 12% or 14% gel, 0.375 M Tris-HCl (pH 8.8) and 0.1% SDS. The stacking gel contains 3% crosslinker, 5% gel, 0.125 M Tris-HCl (pH 6.8) and 0.1% SDS. The gel was run in Tris-glycine buffer (25 mM Tris, 192 mM glycine, 0.1% SDS). Electrophoresis was performed with constant ampere of 100 V/gel at room temperature. After electrophoresis, the protein band on the gel was visualised by 20 min soaking in staining solution containing 50% methanol, 10% glacial acetic acid and 0.1% Coomassie brilliant blue R-250 in H<sub>2</sub>O. The gel was then soaked in destaining solution (10% methanol and 10% glacial acetic acid) overnight or until the background clears.

### 3.2.13 Toxin inclusion solubilisation and proteolytic processing

Protoxin inclusions were solubilised at concentration of 3 mg/ml in 50 mM Na<sub>2</sub>CO<sub>3</sub>, pH 10.0 at 37°C for 1 h. For solubility analysis, the incubated toxins were subjected to centrifugation at 10,000 rcf for 10 min and then toxin concentrations of pre- and post-centrifugation were quantitated as described in **section 3.2.11**. The samples were also analysed on SDS-PAGE.

A solution of 130-kDa protoxins (2 mg/ml) was mixed with trypsin (TCPK treated, Sigma) at enzyme/toxin ratio of 1/20 (w/w) in 50 mM Na<sub>2</sub>CO<sub>3</sub>, pH 10.0 at 37°C for 16 h. The enzyme activity was inhibited by adding phenylmethane sulfonyl fluoride to give a final concentration of 1 mM and trypsin digestion patterns were analysed on SDS-PAGE.

### 3.2.14 Mosquito larvicidal activity assays (117)

2-day old *S. aegypti* mosquito larvae were used for toxicity assays. The larvae were obtained from the mosquito-rearing facility (Institute of Molecular Biology and Genetics, Mahidol University). *E. coli* cells containing pMU388 or mutated plasmids were grown in LB broth with 100 µg/ml ampicillin at 37°C. The expression of protein was induced with 0.1 mM IPTG, incubated at 30°C for 10 h. Cell pellet (10 OD ~ 10x10<sup>8</sup> cells) harvested by centrifugation at 6000 rcf, 4°C for 10 min was suspended in 2 ml of distilled H<sub>2</sub>O. Each assay was performed in a 48-well titration plate (11.3 mm well diameter, Costar, MA, USA), containing 10 larvae in 800 µl of distilled H<sub>2</sub>O. Then, 200 µl of induced *E. coli* cells expressing the Cry4Ba or a mutant toxin (10<sup>8</sup> cells) was added into each well. One hundred larvae were used for each sample in one experiment. At least 3 independent experiments were performed. The mortality was recorded and analysed after 24 h of incubation at room temperature.

### 3.2.15 Purification of Cry4Ba and its derivatives

Purification of the 65-kDa trypsin-treated Cry4Ba toxin or its derivatives was accomplished by using a size-exclusion FPLC system (Superdex 200/HR10 column, Amersham Pharmacia Biotech) eluted with carbonate buffer (50 mM Na<sub>2</sub>CO<sub>3</sub>, pH 10.0) at a flow rate of 0.4 ml/min and monitored by UV absorption at 280 nm. Fractions were collected and analysed on 15% SDS-PAGE. Elution fractions across the 65-kDa protein peak were pooled and subjected to further concentration with a 30-kDa cutoff centrifugal filter tube (MILLIPORE, U.S.A). Protein concentration was determined by Bradford assays.

### 3.2.16 Purification of helix 6 and helix 7 peptides

The purification of helix 6 and 7 peptides was accomplished using semi-preparative RP-HPLC column Jupiter C<sub>4</sub> system. Chromatographic separations were achieved with a linear gradient of B in A. Both the H<sub>2</sub>O phase (A) and the acetonitrile phase (B) include 0.1% TFA. Peptides were eluted at about 45 min and 50 min between 40-60% B gradient for helix 6 and helix 7 peptides, respectively at a flow

rate 1 ml/min. The purified helix 6 and 7 peptides and other fractions were confirmed by mass spectrometer.

### 3.2.17 Circular dichroism (CD) measurement

CD measurements of the purified peptide were performed on a Jasco J-715 CD spectropolarimeter (Jasco Inc., Easton, USA) in the far UV region (190-260 nm) at 25°C using a rectangular quartz cuvette (0.2-mm optical path-length) to gain information about the secondary structure of Cry4Ba toxin and its mutant. The CD spectra were recorded at a scanning rate of 50 nm/min with a spectral bandwidth of 2 nm and response times of 2 msec. Three accumulations were taken and the results were averaged. After background subtraction, all CD data were converted from CD signal (mdegree) into mean residue ellipticity (deg cm<sup>2</sup>/dmole) by the following formula:

$$\Delta\varepsilon = (\theta) \times 10^6 / (c \times d \times \text{mdeg}_{\text{CSA290}})$$

where

$\theta$  is the measured ellipticity (millidegrees)

$c$  is the sample concentration (M)

$\text{mdeg}_{\text{CSA290}}$  is milidegrees of standard CSA at 290 nm ( $\cong 42.34$ )

$d$  is the optical path length of the sample cell (cm)

### 3.2.18 Intrinsic fluorescence spectroscopy

The intrinsic tryptophan fluorescence spectroscopy was used to analyse structural changes of proteins. The fluorescence spectra were obtained by emission scanning of approximately 20  $\mu\text{g/ml}$  toxin protein concentration in quartz cell 0.5 cm path length using the Shimadzu RF 5001PC. All measurements were performed at room temperature with excitation wavelength at 280 nm. The emission spectra were recorded from 300-450 nm and the background spectrum was subtracted from the protein spectrum.

### 3.2.19 Preparation of calcein-entrapped large unilamellar vesicles (LUVs)

LUVs were prepared from 2 mg/ml of a lipid mixture (Avanti Polar Lipid, USA) of phosphatidylcholine (PC)/phosphatidyl-ethanolamine (PE)/cholesterol (Ch)

(10:10:1 w/w) dissolved in chloroform. The solvent was evaporated under a nitrogen stream and the resultant lipid film was suspended in 200  $\mu\text{l}$  of 60 mM calcein (pre-dissolved in 100 mM  $\text{Na}_2\text{CO}_3$ , pH 9.0)/10 mM Tris-HCl, pH 9.0. After subjected to 5 cycles of freezing and thawing, the lipid suspension was repeatedly squeezed through a polycarbonate membrane (0.1- $\mu\text{m}$  pore size, Avanti Polar Lipid, USA) for a minimum of 20 passes, using a two-syringe extruder (Avanti Polar Lipid, USA). The untrapped calcein was removed from the LUV suspension by gel filtration on a HiTrap<sup>TM</sup> desalting column (Amersham Pharmacia Biotech, Uppsala, Sweden), equilibrated with 150 mM NaCl/10 mM Tris-HCl, pH 9.0. Liposome concentrations were estimated by measuring the lipid phosphorus content (118), and a final concentration of 1.25  $\mu\text{M}$  LUV was used for the calcein release assay (119) (see section 3.2.20).

### 3.2.20 Phosphorus content analysis of phospholipid

Phosphorus standards were prepared by making dilution ranging from 0, 10, 20, 30, and 40  $\mu\text{l}$  of 1 mM  $\text{Na}_2\text{HPO}_4$ . Each standard solution was transferred to clean glass tube and solvent is completely dried on heating box and added with 50  $\mu\text{l}$  of 70% perchloric acid, allowed to heat at 180°C for 2 h. After the mixtures were cooled down, 0.9 ml of phosphorus assay solution was added and then incubated at 80°C for 10 min before measuring an absorbance at 820 nm following by plotting a standard curve. For phospholipids samples, 30  $\mu\text{l}$  of liposome suspension were used and the phospholipid concentrations were calculated from the standard curve.

### 3.2.21 Membrane perturbation assay

5  $\mu\text{l}$  of a tested sample (5-10  $\mu\text{g}$ ) was added into 400  $\mu\text{l}$  of LUV solution placed in a 1-cm light-path polymethyl methacrylate cuvette (Brand, Germany), the degree of LUV perturbation was determined as an increase in the fluorescence intensity of the released calcein. Fluorescence was monitored at 25°C on a Perkin-Elmer LS50 spectrofluorimeter with excitation and emission wavelengths set at of 485 and 520 nm, respectively, and a slit width of 5 nm. The time-course of the percentage of calcein release was indicated as a fraction of maximum fluorescence

release determined after addition of 0.1% (v/v) Triton X-100 to the liposome suspension. The percentage of total fluorescence  $F_t$  was defined as

$$F_t = (I_t - I_o / I_f - I_o) \times 100$$

where  $I_o$  = the initial fluorescence,  $I_f$  = the total fluorescence observed after addition of Triton X-100, and  $I_t$  = the fluorescence observed after addition of the protein sample.

### **3.2.22 ATR-FTIR spectroscopy**

#### **3.2.22.1 Sample preparation**

DMPC, DMPG and DDPC were used as lipid model for study. the peptide and lipid membrane were mixed in a glass vial in 1,1,1,3,3,3-hexafluoro-2-propanol. The mixture was applied onto a trapezoidal germanium internal reflection element (Graseby Specac, Kent, UK) of dimensions 50mm x 2mm x 20mm. For hydration under D<sub>2</sub>O and H/D exchange experiments, spectra were collected after flushing the interior of the sample cell with D<sub>2</sub>O-saturated nitrogen gas, obtained by bubbling dry nitrogen through two compartments containing D<sub>2</sub>O for 1 h.

#### **3.2.22.2 Polarised ATR-FTIR measurements**

ATR-FTIR spectra were collected on a Nicolet Nexus 470 spectrometer purged with dry air and equipped with a MCT/A detector cooled with liquid nitrogen. Infrared spectra were measured with a 25-reflections ATR accessory (Graseby Specac, Kent, UK) and a wire grid polariser (0.25  $\mu\text{m}$ , Graseby Specac). A total 200 interferograms were collected using either parallel or perpendicular polarised light at a resolution of 4  $\text{cm}^{-1}$ . Interferograms were processed using 1-point zero filling and Happ-Genzel apodisation followed by automatic base line correction.

#### **3.2.22.3 Analysis of ATR-FTIR data**

To determine the amide I and A absorption bands of the peptide, polarised spectra were collected either after removal of bulk H<sub>2</sub>O or after hydration with D<sub>2</sub>O. In the first case, the dichroic ratios ( $R^{\text{ATR}}$ ) of the amide I band (due to C=O stretching) and that corresponding to the band at 2850  $\text{cm}^{-1}$  (due to the symmetric CH<sub>2</sub> stretching of the lipid) were recorded. In the later case, after hydration with D<sub>2</sub>O until no

significant differences between the spectra in the CH<sub>2</sub> stretching and amide I or amide A regions were observed, suggesting that maximal hydration occurred within 1 h. The dichroic ratio of the amide A band (due to N-H stretching) was also recorded. Dichroic ratios were calculated as the ratio between the integrated absorptions collected with parallel and perpendicular polarised light.

A correlation between frequency of the amide I vibrational mode and secondary structure has been well established in the literature (120). Amide I is the most intense absorption band in proteins. Its frequency is found in the range between 1600 and 1700 cm<sup>-1</sup>. The exact band position is determined by the backbone conformation and the hydrogen bonding pattern. Frequencies in the regions of 1650-1660 cm<sup>-1</sup> correspond to  $\alpha$ -helical segments while modes resonating in regions of 1630-1640 and 1670-1685 cm<sup>-1</sup> correspond to  $\beta$ -sheet elements or turns.

To determine the secondary structure of a peptide in the membrane environment, curve fitting of the amide I band was Fourier self-deconvoluted (FSD) with a full-width at a half-height of 20 cm<sup>-1</sup> and an enhancement factor *k* of 2.0. Peak integration was performed on these spectra from 1700 to 1600 cm<sup>-1</sup> (121). For the amide A band and the band of symmetric CH<sub>2</sub> stretching, integration was performed without deconvolution from 3400 to 3200 cm<sup>-1</sup> and from 2890 to 2800 cm<sup>-1</sup>, respectively.

The order parameters were calculated as previously (122). First, the order parameters for the helix  $S_{\text{helix}}$  and the lipid  $S_{\text{lipid}}$  were calculated according to the formula:

$$S = \frac{\epsilon_x^2 - R^{\text{ATR}} \epsilon_y^2 + \epsilon_z^2}{\epsilon_x^2 - R^{\text{ATR}} \epsilon_y^2 - \epsilon_z^2} \div \frac{3\cos^2\alpha - 1}{2}$$

where  $R^{\text{ATR}}$  is the dichroic ratio of amide I or amide A for the protein and the dichroic ratio of the 2850 cm<sup>-1</sup> band for lipid. The angle  $\alpha$  is the angle between the direction of the transition dipole moment of the vibrational transition and the z-axis. The angle  $\alpha$  is 90° for the lipid symmetric CH<sub>2</sub> stretching (2850 cm<sup>-1</sup> band), 39° for the peptidic C=O bond (angle between the helix director and the transition dipole moment of the amide I vibrational mode) and 29° for the N-H bond (123,124). The parameters (electric field components of the evanescent wave)  $\epsilon_x = 1.398$ ,  $\epsilon_y = 1.516$  and  $\epsilon_z =$

1.625 are the integrated absorption coefficients for a germanium reflection element given by Harrick (125) according to a thick-film approximation. The contribution of  $S_{lipid}$  to  $S_{helix}$  was taken into account and the helix tilt  $\beta$  was calculated from (96)

$$S_{helix'} = \frac{S_{helix}}{S_{lipid}}$$

according to

$$S_{helix'} = \frac{3(\cos^2 \beta) - 1}{2}$$

The precision in the determination of the helix tilt is increased by using the N-H stretching because the angle  $\alpha$  is smaller than for the C=O bond stretching (see above), and consequently the possible range of dichroic ratios is wider (96). Also, the amide A band in these conditions, i.e. when the sample is exposed to D<sub>2</sub>O, originates only from the transmembrane  $\alpha$ -helix that has not exchanged, therefore it only takes into account the contribution of amino acids that have inserted properly in the membrane. Thus, amide A was used to calculate the tilt of the peptide in a membrane environment. Isotopic (H/D) exchange was calculated from the ratio amide A/C=O stretching of lipid (1730 cm<sup>-1</sup>) before and after H/D exchange using non-polarised spectra. These were obtained from the parallel ( $\parallel$ ) and perpendicularly ( $\perp$ ) ATR polarised spectra, according to 1 ( $\parallel$ ) + 1.44 ( $\perp$ ), as described by Marsh (126).

### 3.2.23 Molecular dynamics simulations

Helical and beta-structure models of helices (31-residue helix 6, 27-residue helix 7) and  $\beta$ -hairpin (27-residue helix 7 sequence) were generated by using a combined simulated annealing and MD simulations (SD/MD) approach *via* Xplor and What if programs, respectively. The  $\beta$ -hairpin model was embedded in a preequilibrated lipid bilayer consisting of 128 molecules of DMPC. Unfavorable lipid-protein contact made necessary the removal of 32 DMPC molecules, giving a final total of 96 lipid molecules. The whole system was solvated in 6108 molecules with a Na<sup>+</sup> ion added at position corresponding to the lowest Coulombic energy of the ion. For 27-residue  $\alpha$ -helix 7 formation lying at the interface, the system contains 243

DMPC (initial set-up 288 DMPC molecules) and 12199 water molecules. Like  $\beta$ -hairpin model system,  $\alpha$ -helical model of 31-residue helix 6 peptide was placed at the interface of a bilayer of 116 DMPC (initial set-up 128 DMPC molecules) and 5960 water molecules. In peptide-orientation setup details, helical model of helix 7/surface was perpendicular to the bilayer normal, with its aromatic side chains (Phe<sup>7</sup>) pointing towards to the bilayer that based on the ATR-FTIR experiments. Helix 6 was also perpendicular to the bilayer with high hydrophobic side-chain region point towards the lipid surface. On the other hand,  $\beta$  structure was inserted across the bilayer. Each system was minimised and equilibrated for 400 ps before unrestraint MD simulations. Gromacs 3.2.1 software (<http://www.gromacs.org>) was used in all 10 ns MD simulations systems. The simulations used a time step of 2 fs and a LINCS algorithm to keep the geometry of the molecules. An isothermal-isobaric ensemble was used with periodic boundaries and Berendsen temperature and pressure coupling. Long-range electrostatics have been calculated with the particle-mesh Ewald (PME) method. Lennard-Jones and short-range Coulombic interactions were cut off at 1.0 nm.

The root mean square deviation (RMSD) of C <sub>$\alpha$</sub>  atom of peptide was calculated using g\_rmsd program. The diagrams of secondary structure versus time for the conformational dynamics were analysed by DSSP program.

## CHAPTER IV

### RESULT I: MUTAGENESIS OF CONSERVED AROMATIC RESIDUES IN HELIX 7 OF Cry4Ba

#### 4.1 Constructions of Cry4Ba-mutant plasmids

As was previously suggested in the “umbrella-like” model for the membrane-bound state of the *Bt* Cry  $\delta$ -endotoxins, the conserved helix 7 could function as a membrane-binding sensor of the pore-forming domain (78), although its functional elements have not yet been clearly identified. Moreover, previous studies suggested that the integrity of  $\alpha 7$  conceivably plays a role in larvicidal activity similar to that was observed for  $\alpha 4$  and  $\alpha 5$  (26,84) by performing single-proline scanning. Due to several studies, the aromatic residues could play several different roles in membrane-protein interactions. Therefore, in this study, four conserved aromatic residues, Trp<sup>243</sup>, Phe<sup>246</sup>, Tyr<sup>249</sup> and Phe<sup>264</sup> within helix 7 were chosen to be investigated by changing to alanine. The pMU388 plasmid encoding the 130-kDa Cry4Ba toxin (117) was used as a template for the introduction of single mutations. After PCR amplification, the 6.38-kb amplified products were digested with *DpnI* and analysed on 1% agarose gel electrophoresis as shown in **Figures 4.1-4.2**. The results showed that the size of all PCR products correspond to the length of the pMU388 DNA template.

The digested PCR products were then transformed into *E. coli* JM109 competent cells. The transformants from each mutation were screened using restriction endonuclease digestion as shown in **Figures 4.3-4.6A**. Each mutant plasmid was further confirmed by automated DNA sequencing (see **Figures 4.3-4.6B**). It is found that all mutants contain nucleotide changes at the desired positions.

## 4.2 Expression of the Cry4Ba-helix 7 mutant toxins

When each mutant toxin (W243A, F246A, Y249A and F264A) was expressed in *E. coli* upon IPTG induction at 30°C for 10 h, all were produced as inclusion bodies, and the expression level of the 130-kDa mutant protoxins was approximately the same as that of the wild-type toxin as shown in **Figure 4.7**.

## 4.3 Solubilisation and proteolytic processing of the Cry4Ba-helix 7 mutants

Experiments were further conducted to assess the solubility *in vitro* of the mutant protein inclusions in comparison with that of the wild-type. For determining the percentage of toxin solubility in carbonate buffer, pH 10.0 at 30°C for 1 h, the amounts of the 130-kDa soluble proteins in the supernatant were compared with those of the total protein inclusions that were initially used. It was found that a complete loss of the inclusion solubility was found for all the mutants with exception for the F246A mutant (see **Figure 4.8**).

The F264A 130-kDa soluble toxins were also assessed for their proteolytic processing by digestion with TPCK-treated trypsin at 37°C for 16 h. After analysed on SDS-PAGE, it showed two major trypsin-resistant fragments of ca. 47 and 20 kDa that are identical to the products obtained with the wild-type protoxin (**Figure 4.9**).

## 4.4 Larvicidal activity of Cry4Ba-helix 7 mutant toxins

To determine an effect of these single-alanine substitutions on toxicity, *E. coli* cells expressing each mutant toxin for their relative biological activity against *S. aegypti* mosquito larvae. The mortality data recorded after 24-h incubation revealed that the W243A, Y249A and F264A mutants exhibited a drastic decrease in larvicidal activity, whereas the F246A mutant showed only a small reduction in toxicity when compared to the wild-type toxin (**Figures 4.10-4.11**). As can be seen that both protoxin inclusions and *E. coli* whole cells gave similar results for toxicity activity. These results suggested that Trp<sup>243</sup>, Tyr<sup>249</sup> and Phe<sup>264</sup> in  $\alpha 7$  play a role in larvicidal activity of the Cry4Ba toxin.

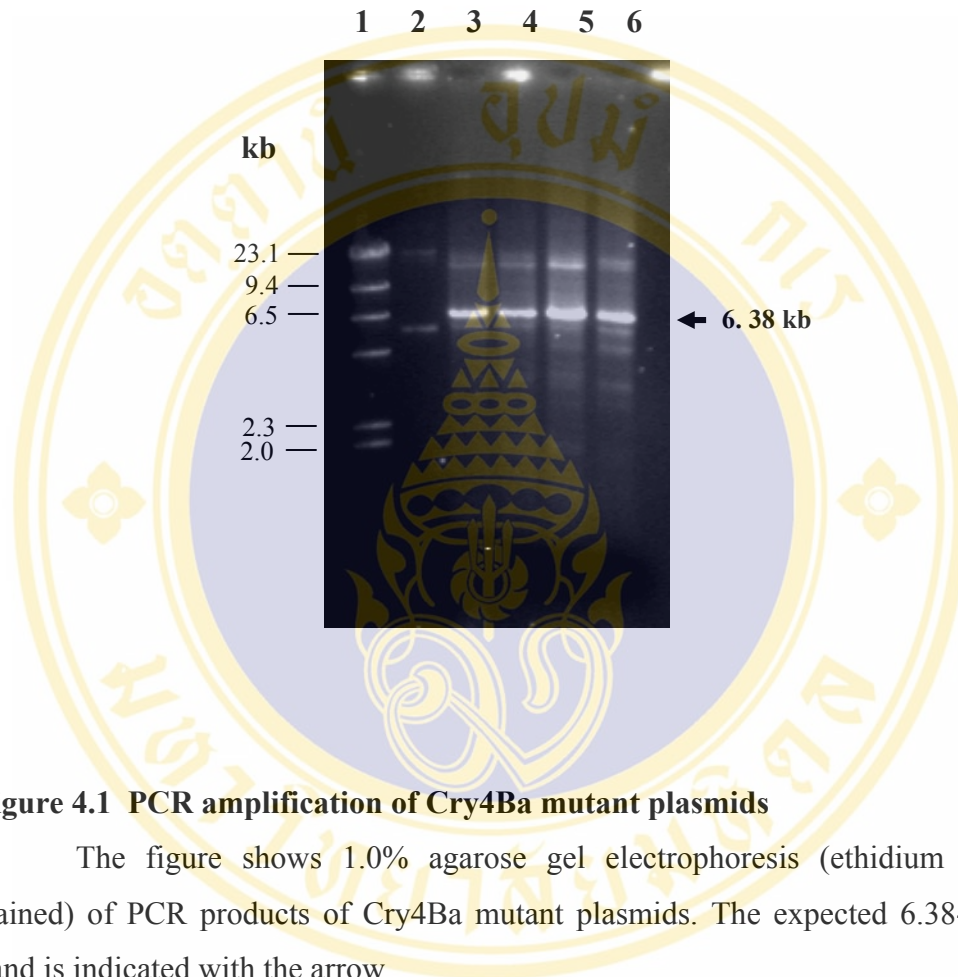


**Figure 4.1 PCR amplification of Cry4Ba mutant plasmids**

The figure shows 1.0% agarose gel electrophoresis (ethidium bromide-stained) of PCR products of Cry4Ba mutant plasmids. The expected 6.38-kb DNA band is indicated with the arrow.

- Lane 1:  $\lambda$ /HindIII digested DNA marker
- Lane 2: The template (pMU388 plasmid)
- Lane 3: The PCR product of the pW243A plasmid
- Lane 4: The PCR product of the pF246A plasmid
- Lane 5: The PCR product of the pY249A plasmid
- Lane 6: The PCR product of the pF264A plasmid

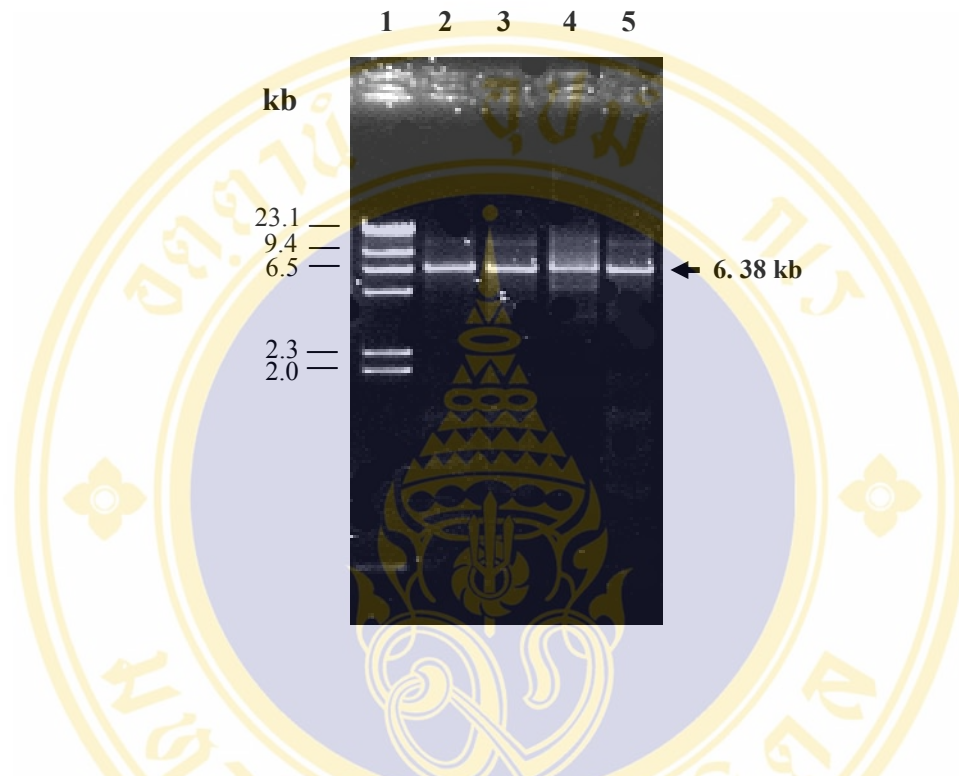


**Figure 4.2 The PCR products of Cry4Ba mutant plasmids digested with *DpnI***

The figure shows 1.0% agarose gel electrophoresis (ethidium bromide-stained) of digested PCR products of Cry4Ba mutant plasmids with *DpnI*. The expected 6.38-kb DNA band is indicated with the arrow.

Lane 1:  $\lambda$ /*HindIII* digested DNA marker

Lane 2: The PCR product of the pW243A plasmid digested with *DpnI*

Lane 3: The PCR product of the pF246A plasmid digested with *DpnI*

Lane 4: The PCR product of the pY249A plasmid digested with *DpnI*

Lane 5: The PCR product of the pF264A plasmid digested with *DpnI*

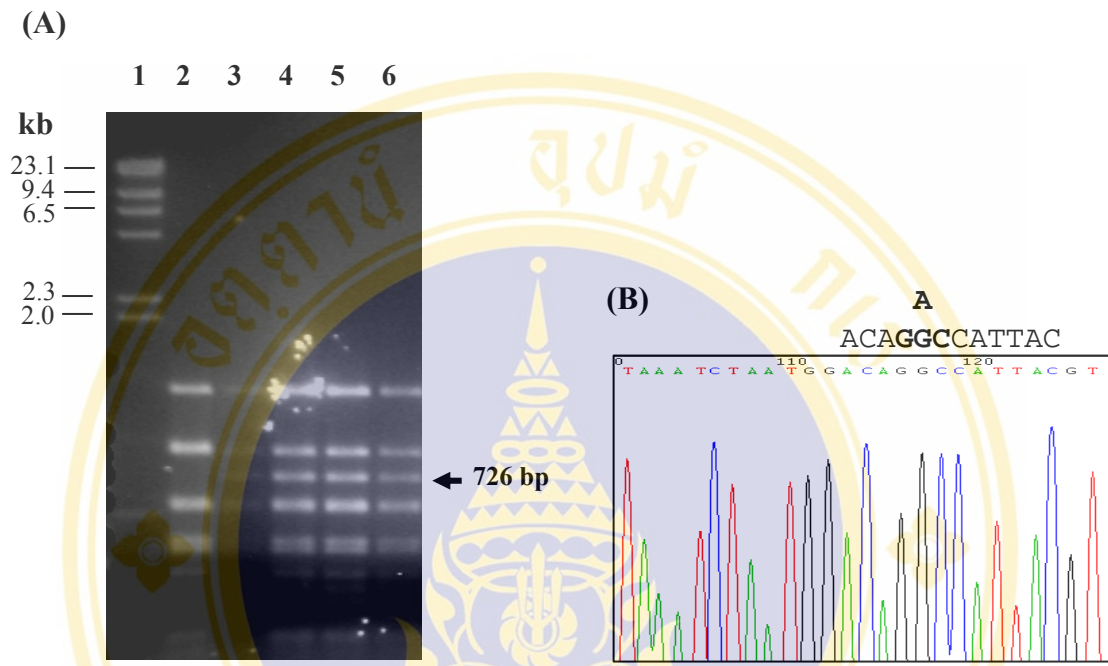


**Figure 4.3 Restriction digestion and DNA sequence analysis of pW243A**

The figure shows (A) 1.0 % agarose gel electrophoresis of *HaeIII* digestion patterns of the wild-type and mutant plasmids. The 726-bp mutant DNA band is indicated with the arrow.

Lane 1:  $\lambda$ /*HindIII* digested DNA marker

Lane 2: The *HaeIII* digested wild-type plasmid, pMU388

Lane 3: The *HaeIII* digested mutant plasmid, pW243A clone no. 1

Lane 4: The *HaeIII* digested mutant plasmid, pW243A clone no. 2

Lane 5: The *HaeIII* digested mutant plasmid, pW243A clone no. 3

Lane 6: The *HaeIII* digested mutant plasmid, pW243A clone no. 4

(B) The DNA sequencing chromatogram of pW243A (clone no. 2), using N195A-f as a sequencing primer. Part of the sense strand sequence is shown. The bold letter represents the substituted amino acid residue.

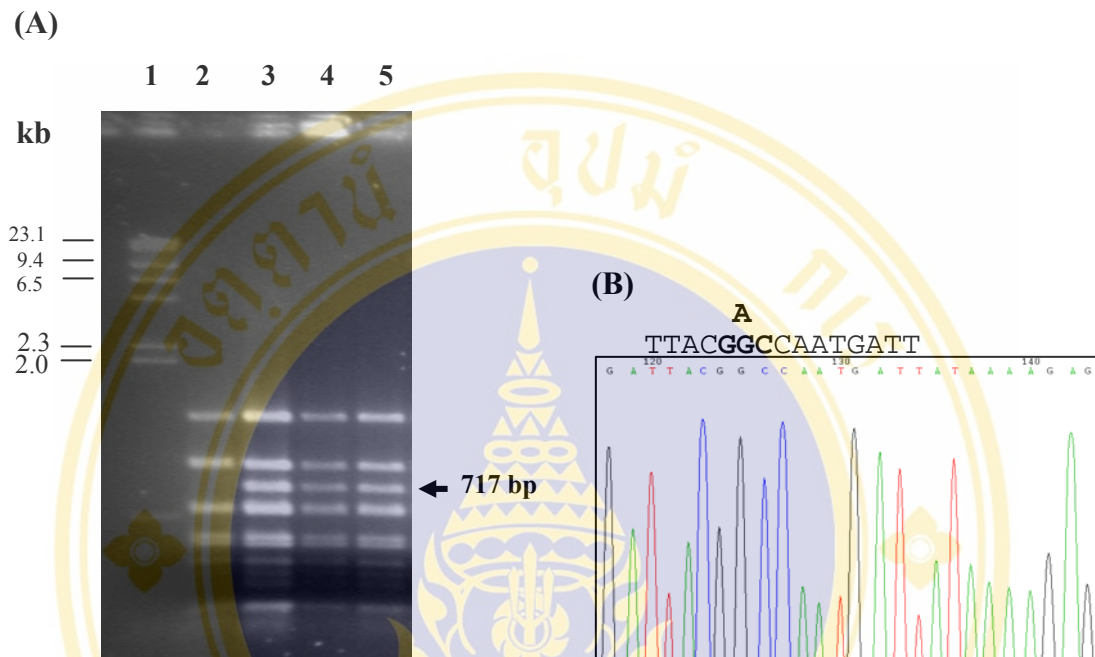


**Figure 4.4 Restriction digestion and DNA sequence analysis of pF246A**

The figure shows (A) 1.0 % agarose gel electrophoresis of *Hae*III digestion patterns of the wild-type and mutant plasmids. The 717-bp mutant DNA band is indicated with the arrow.

Lane 1:  $\lambda$ /*Hind*III digested DNA marker

Lane 2: The *Hae*III digested wild-type plasmid, pMU388

Lane 3: The *Hae*III digested mutant plasmid, pF246A clone no. 1

Lane 4: The *Hae*III digested mutant plasmid, pF246A clone no. 2

Lane 5: The *Hae*III digested mutant plasmid, pF246A clone no. 3

(B) The DNA sequencing chromatogram of pF246A (clone no. 2), using N195A-f as a sequencing primer. Part of the sense strand sequence is shown. The bold letter represents the substituted amino acid residue.

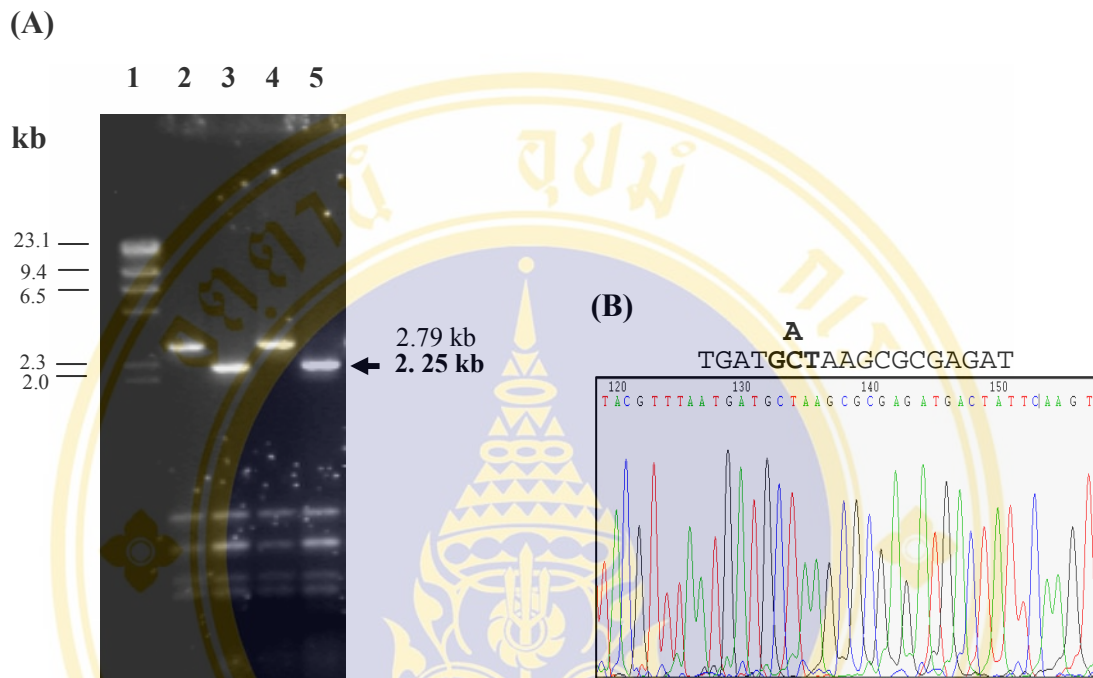


**Figure 4.5 Restriction digestion and DNA sequence analysis of pY249A**

The figure shows (A) 1.0 % agarose gel electrophoresis of *HhaI* digestion patterns of the wild-type and mutant plasmids. The 2.25-kb mutant DNA band is indicated with the arrow.

Lane 1:  $\lambda$ /*HindIII* digested DNA marker

Lane 2: The *HhaI* digested wild-type plasmid, pMU388

Lane 3: The *HhaI* digested mutant plasmid, pY249A clone no. 1

Lane 4: The *HhaI* digested mutant plasmid, pY249A clone no. 2

Lane 5: The *HhaI* digested mutant plasmid, pY249A clone no. 3

(B) The DNA sequencing chromatogram of pY249A (clone no. 1), using N195A-f as a sequencing primer. Part of the sense strand sequence is shown. The bold letter represents the substituted amino acid residue.

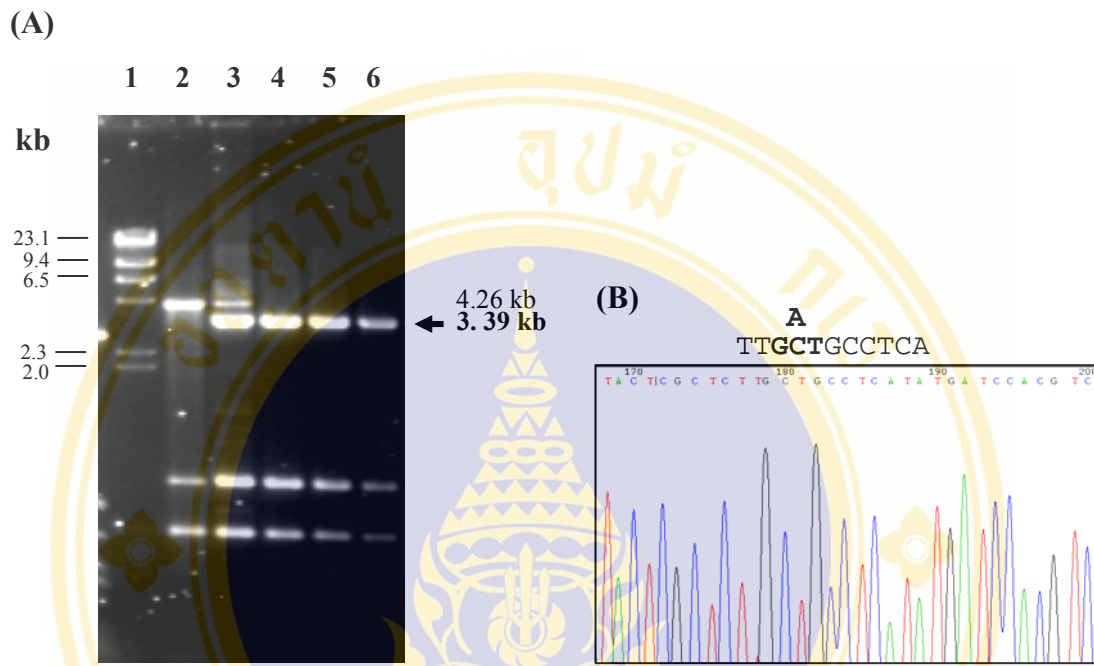


**Figure 4.6 Restriction digestion and DNA sequence analysis of pF264A**

The figure shows (A) 1.0 % agarose gel electrophoresis of *NdeI* digestion patterns of the wild-type and mutant plasmids. The 3.39-kb mutant DNA band is indicated with the arrow.

Lane 1 : $\lambda$ /*HindIII* digested DNA marker

Lane 2 :The *NdeI* digested wild-type plasmid, pMU388

Lane 3 :The *NdeI* digested mutant plasmid, pF264A clone no. 1

Lane 4 :The *NdeI* digested mutant plasmid, pF264A clone no. 2

Lane 5 :The *NdeI* digested mutant plasmid, pF264A clone no. 3

Lane 6 :The *NdeI* digested mutant plasmid, pF264A clone no. 4

(B) The DNA sequencing chromatogram of pF264A (clone no. 1), using N195A-f as a sequencing primer. Part of the sense strand sequence is shown. The bold letter represents the substituted amino acid residue.

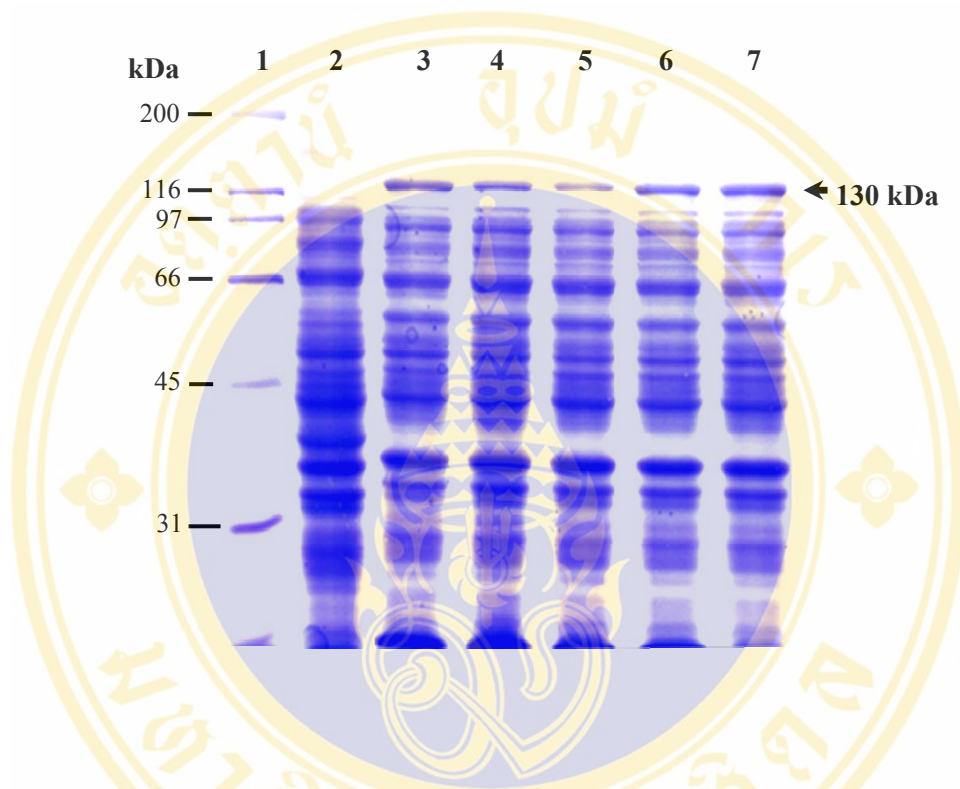


**Figure 4.7 Expression of the Cry4Ba mutant toxins**

The figure shows SDS-PAGE protein profile (Coomassie blue-stained 10% gel) of crude extracts from IPTG induced *E. coli* containing different mutant plasmids. The expected 130-kDa protoxin band is indicated by the arrow.

Lane 1: Molecular mass protein standards

Lane 2: Crude extracted proteins of *E. coli* containing pUC12

Lane 3: Crude extracted proteins of *E. coli* containing pMU388

Lane 4: Crude extracted proteins of *E. coli* containing pW243A

Lane 5: Crude extracted proteins of *E. coli* containing pF246A

Lane 6: Crude extracted proteins of *E. coli* containing pY249A

Lane 7: Crude extracted proteins of *E. coli* containing pF264A

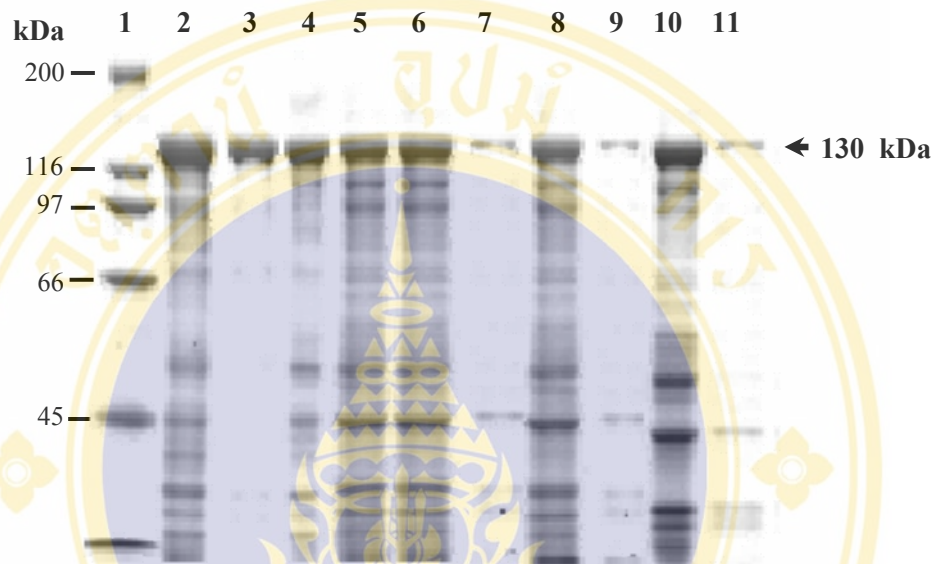


**Figure 4.8 Solubility of Cry4Ba mutant inclusions**

The figure shows SDS-PAGE (10% Coomassie blue-stained) comparing the solubility of the mutant inclusions in 50 mM carbonate buffer, pH 10.0 at 37°C for 1 h. The expected 130-kDa protoxin band is indicated by the arrow.

- Lane 1: Molecular mass protein standards
- Lane 2: The partially purified Cry4Ba inclusion
- Lane 3: The solubilised fraction Cry4Ba
- Lane 4: The partially purified F246A inclusion
- Lane 5: The solubilised fraction F246A
- Lane 6: The partially purified W243A inclusion
- Lane 7: The solubilised fraction W243A
- Lane 8 :The partially purified Y249A inclusion
- Lane 9 :The solubilised fraction Y249A
- Lane 10 :The partially purified F264A inclusion
- Lane 11 :The solubilised fraction F264A

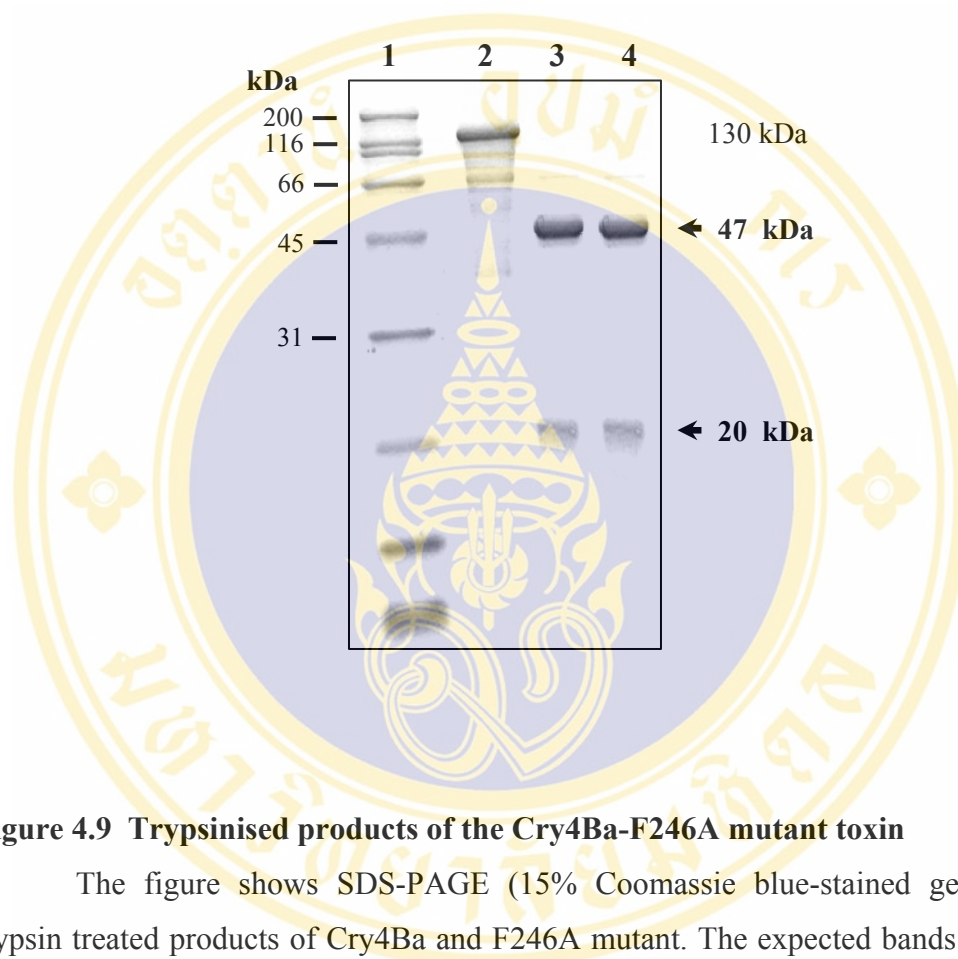


**Figure 4.9 Trypsinised products of the Cry4Ba-F246A mutant toxin**

The figure shows SDS-PAGE (15% Coomassie blue-stained gel) of the trypsin treated products of Cry4Ba and F246A mutant. The expected bands of ca. 47 and ca. 20 kDa are indicated.

Lane 1: Molecular mass protein standards

Lane 2: The 130-kDa Cry4Ba toxin

Lane 3: Trypsin treated products of the Cry4Ba wild-type toxin

Lane 4: Trypsin treated products of F246A

Toxin	% Mortality					
	pUC12	pMU388	W243A	F246A	Y249A	F264A
Mean	2.3	85.7	19.0	63.3	22.7	15.7
SEM	1.2	4.4	3.9	3.2	3.8	2.6

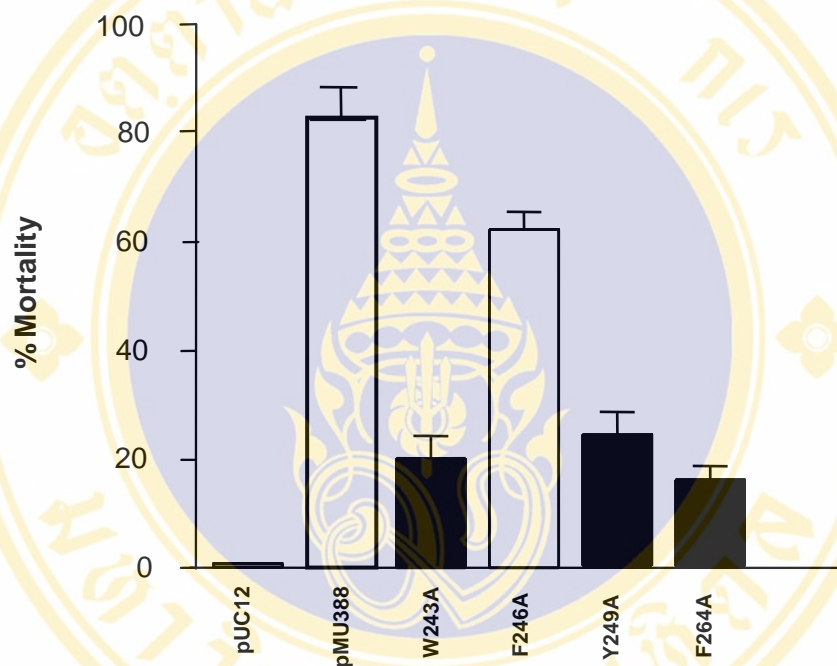


**Figure 4.10** Larvicidal activity of *E. coli* cells expressing of W<sup>243</sup>, F<sup>246</sup>, Y<sup>249</sup> and F<sup>264</sup> mutants

The figure shows larvicidal activity of the wild-type Cry4Ba and its mutant toxins against *S. aegypti* larvae using *E. coli* cells. Error bars represent standard errors of the mean from three independent experiments.

Toxin	% Mortality				
	pMU388	W243A	F246A	Y249A	F264A
Mean	100.0	22.9	59.2	0.8	2.5
SEM	0.0	0.9	1.4	0.9	1.2

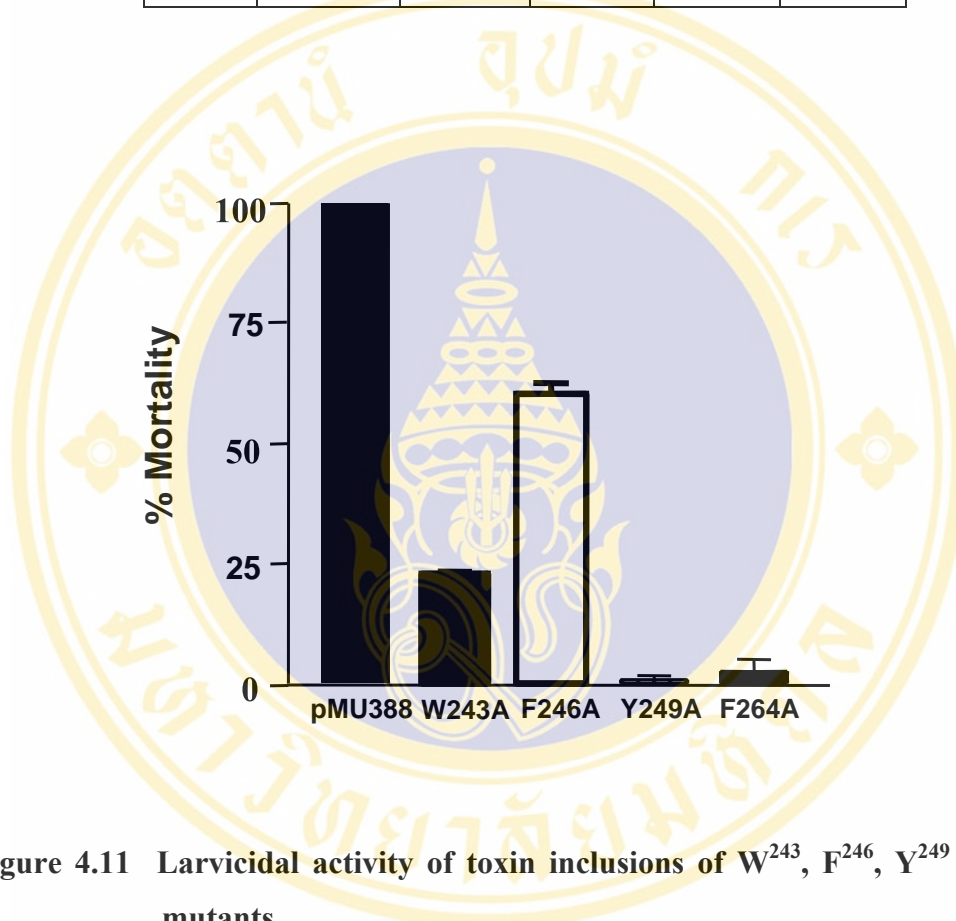


**Figure 4.11 Larvicidal activity of toxin inclusions of W<sup>243</sup>, F<sup>246</sup>, Y<sup>249</sup> and F<sup>264</sup> mutants**

The figure shows a larvicidal activity of the wild-type Cry4Ba and its mutant toxins against *S. aegypti* larvae using 5 µg protoxin inclusions. Error bars represent standard errors of the mean from three independent experiments.

#### 4.5 Mutagenic analysis of Trp<sup>243</sup>, Tyr<sup>249</sup> and Phe<sup>264</sup>

As can be inferred from the Cry4Ba crystal structure (**Figure 2.1**), both Tyr<sup>249</sup> and Phe<sup>264</sup> are oriented such that their aromatic side chains face towards in the same direction. Together with the toxicity data, this configuration might imply a functional and/or structural role for these two conserved residues in the membrane-binding step of the toxin. It has been shown by numerous studies that the binding of membrane-inserting proteins to the lipid membrane surface *via* an aromatic cluster is a prerequisite for their membrane insertion and pore formation (129,130,131). In this regard, further mutagenic analysis was performed using more refined substitutions at these two critical residues (Tyr<sup>249</sup> and Phe<sup>264</sup>) by changing to leucine, tryptophan, glutamic, aspartic, histidine and to either phenylalanine or tyrosine. For Trp<sup>243</sup> that is buried within the domain I-II interface and located opposite to Tyr<sup>249</sup> and Phe<sup>264</sup> (see **Figure. 2.1**), was also mutated to lysine, leucine or phenylalanine.

The pMU388 plasmid containing the *cry4Ba* gene was used as a template for the PCR amplification. In addition, two double mutants, Y249L/F264L and F264A/Y249A, were also constructed by using two resultant mutant plasmids, pY249L and pF264A, used as templates for generating double mutations, Y249L/F264L and F264A/Y249A, respectively. The 6.38 kb amplified products were digested with *DpnI* and analysed on 1% agarose gel electrophoresis as shown in **Figures 4.12-4.14**. The results showed all the PCR products are similar size corresponding to that of the pMU388 DNA template.

The PCR products digested with *DpnI* were then transformed into *E. coli* JM109 competent cells. Each mutation was screened using restriction endonuclease digestion as shown in **Figures 4.15-4.31A** and was further confirmed by automated DNA sequencing (see **Figures 4.15-4.31B**). It is found that all mutants contain nucleotide changes at the desired positions

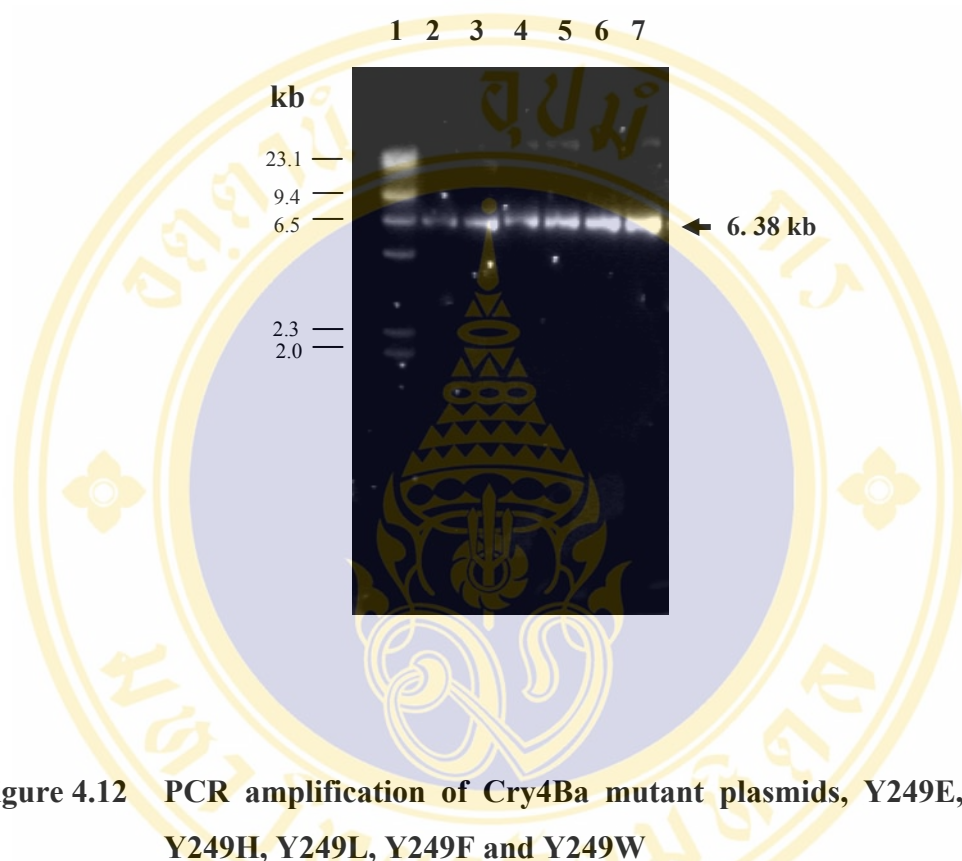


**Figure 4.12 PCR amplification of Cry4Ba mutant plasmids, Y249E, Y249R, Y249H, Y249L, Y249F and Y249W**

The figure shows 1.0% agarose gel electrophoresis (ethidium bromide-stained) of digested PCR products of Cry4Ba mutant plasmids. The expected 6.38-kb DNA band is indicated with the arrow.

Lane 1:  $\lambda$ /HindIII digested DNA marker

Lane 2: The PCR product of the pY249E plasmid digested with *DpnI*

Lane 3: The PCR product of the pY249R plasmid digested with *DpnI*

Lane 4: The PCR product of the pY249H plasmid digested with *DpnI*

Lane 5: The PCR product of the pY249L plasmid digested with *DpnI*

Lane 6: The PCR product of the pY249F plasmid digested with *DpnI*

Lane 7 :The PCR product of the pY249W plasmid digested with *DpnI*

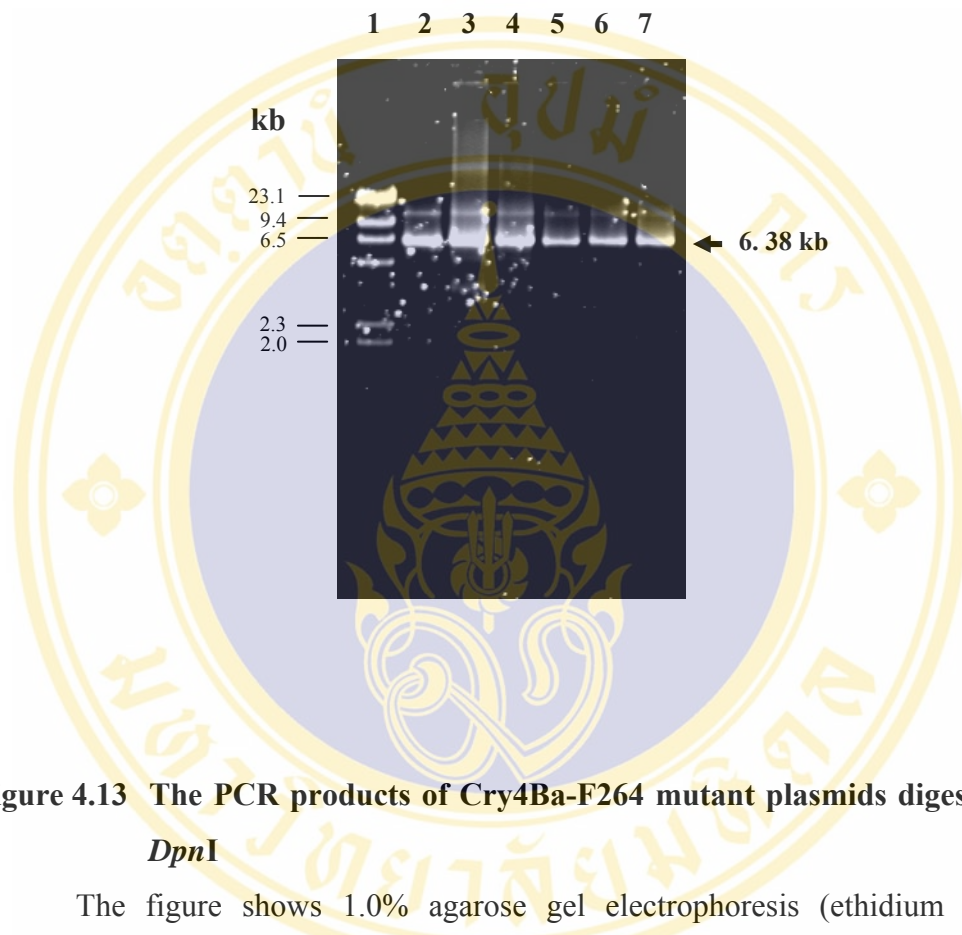


**Figure 4.13** The PCR products of Cry4Ba-F264 mutant plasmids digested with *DpnI*

The figure shows 1.0% agarose gel electrophoresis (ethidium bromide-stained) of digested PCR products of Cry4Ba mutant plasmids with *DpnI*. The expected 6.38-kb DNA band is indicated with the arrow.

Lane 1:  $\lambda$ -HindIII digested DNA marker

Lane 2: The PCR product of the pF264E plasmid digested with *DpnI*

Lane 3: The PCR product of the pF264R plasmid digested with *DpnI*

Lane 4: The PCR product of the pF264H plasmid digested with *DpnI*

Lane 5: The PCR product of the pF264L plasmid digested with *DpnI*

Lane 6: The PCR product of the pF264Y plasmid digested with *DpnI*

Lane 7: The PCR product of the pF264W plasmid digested with *DpnI*

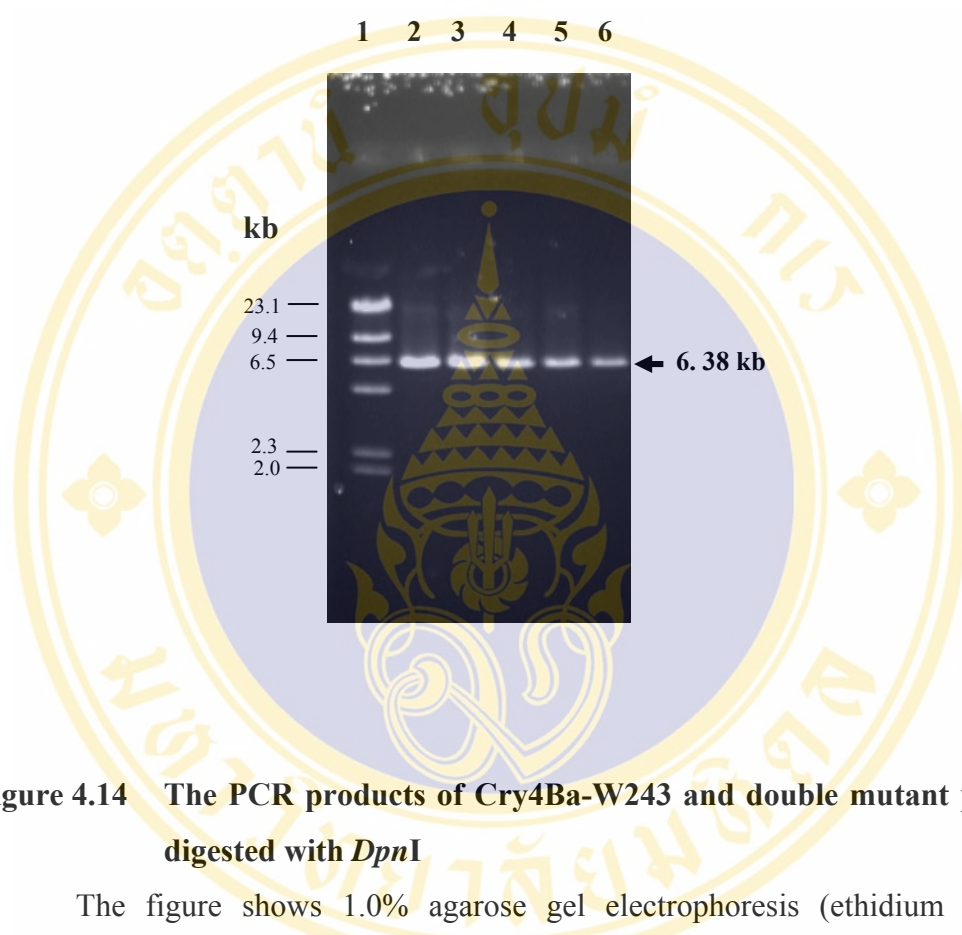


**Figure 4.14** The PCR products of Cry4Ba-W243 and double mutant plasmids digested with *DpnI*

The figure shows 1.0% agarose gel electrophoresis (ethidium bromide-stained) of digested PCR products of Cry4Ba mutant plasmids with *DpnI*. The expected 6.38-kb DNA band is indicated with the arrow.

Lane 1:  $\lambda$ /*HindIII* digested DNA marker

Lane 2: The PCR product of the pW243F plasmid digested with *DpnI*

Lane 3: The PCR product of the pW243K plasmid digested with *DpnI*

Lane 4: The PCR product of the pW243L plasmid digested with *DpnI*

Lane 5: The PCR product of the pY249L/F264L plasmid digested with *DpnI*

Lane 6: The PCR product of the pF264A/Y249A plasmid digested with *DpnI*

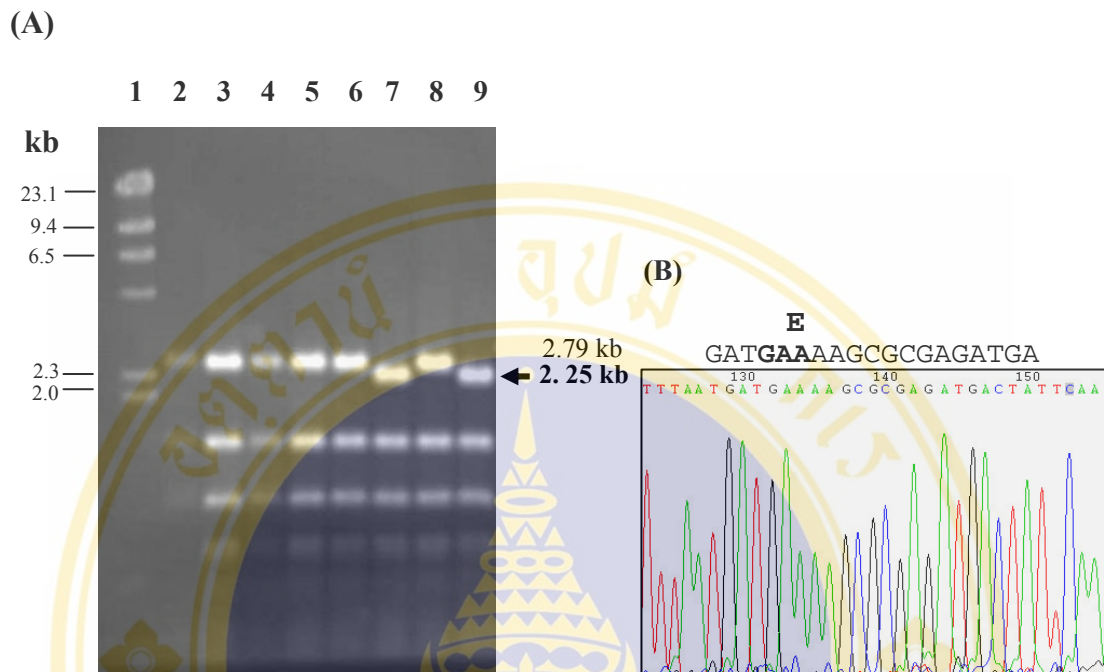


**Figure 4.15 Restriction digestion and DNA sequence analysis of pY249E**

The figure shows (A) 1.0 % agarose gel electrophoresis of *HhaI* digestion patterns of the wild-type and mutant plasmids. The 2.25-kb mutant DNA band is indicated with the arrow.

Lane 1:  $\lambda$ /*HindIII* digested DNA marker

Lane 2: The *HhaI* digested wild-type plasmid, pMU388

Lane 3: The *HhaI* digested mutant plasmid, pY249E clone no. 1

Lane 4: The *HhaI* digested mutant plasmid, pY249E clone no. 2

Lane 5: The *HhaI* digested mutant plasmid, pY249E clone no. 3

Lane 6: The *HhaI* digested mutant plasmid, pY249E clone no. 4

Lane 7: The *HhaI* digested mutant plasmid, pY249E clone no. 5

Lane 8: The *HhaI* digested mutant plasmid, pY249E clone no. 6

Lane 9: The *HhaI* digested mutant plasmid, pY249E clone no. 7

(B) The DNA sequencing chromatogram of pY249E (clone no. 5), using N195A-f as a sequencing primer. Part of the sense strand sequence is shown. The bold letter represents the substituted amino acid residue.

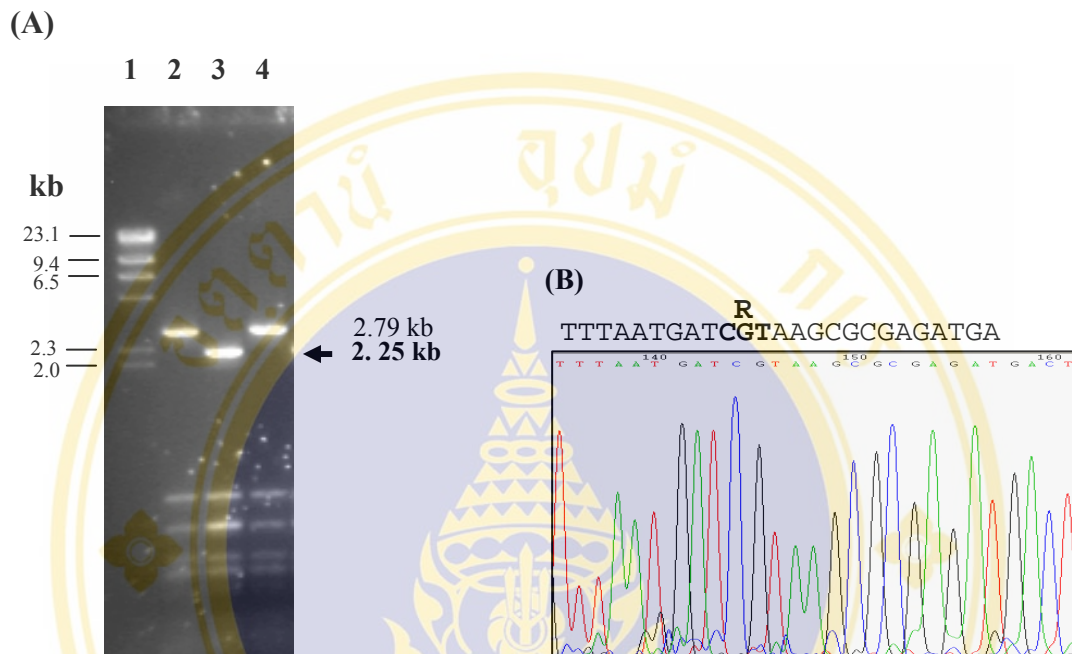


**Figure 4.16 Restriction digestion and DNA sequence analysis of pY249R**

The figure shows (A) 1.0 % agarose gel electrophoresis of *HhaI* digestion patterns of the wild-type and mutant plasmids. The 2.25-kb mutant DNA band is indicated with the arrow.

Lane 1:  $\lambda$ /*HindIII* digested DNA marker

Lane 2: The *HhaI* digested wild-type plasmid, pMU388

Lane 3: The *HhaI* digested mutant plasmid, pY249R clone no. 1

Lane 4: The *HhaI* digested mutant plasmid, pY249R clone no. 2

(B) The DNA sequencing chromatogram of pY249R (clone no. 1), using N195A-f as a sequencing primer. Part of the sense strand sequence is shown. The bold letter represents the substituted amino acid residue.

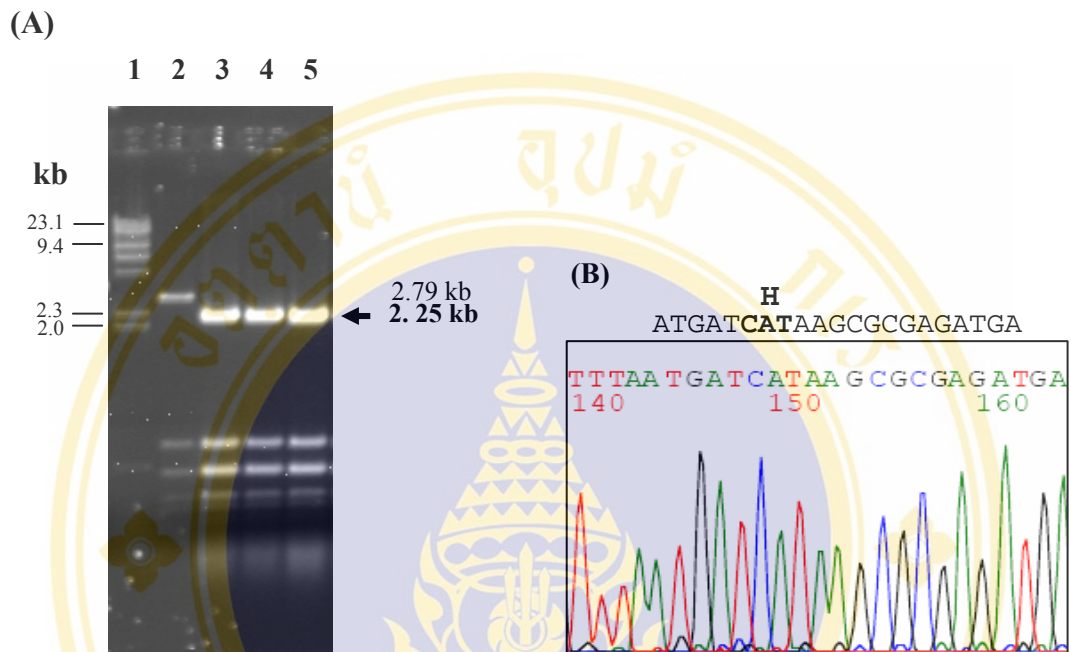


**Figure 4.17 Restriction digestion and DNA sequence analysis of pY249H**

The figure shows (A) 1.0 % agarose gel electrophoresis of *Hha*I digestion patterns of the wild-type and mutant plasmids. The 2.25-kb mutant DNA band is indicated with the arrow.

Lane 1:  $\lambda$ /*Hind*III digested DNA marker

Lane 2: The *Hha*I digested wild-type plasmid, pMU388

Lane 3: The *Hha*I digested mutant plasmid, pY249H clone no. 1

Lane 4: The *Hha*I digested mutant plasmid, pY249H clone no. 2

Lane 5: The *Hha*I digested mutant plasmid, pY249H clone no. 3

(B) The DNA sequencing chromatogram of pY249H (clone no. 1), using N195A-f as a sequencing primer. Part of the sense strand sequence is shown. The bold letter represents the substituted amino acid residue.

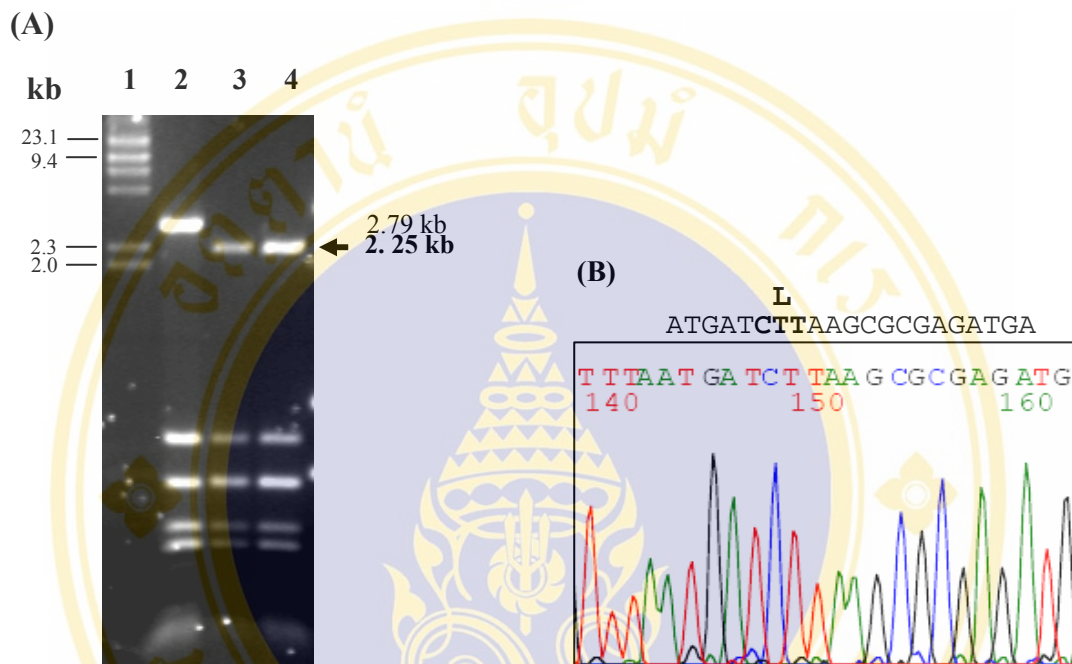


**Figure 4.18 Restriction digestion and DNA sequence analysis of pY249L**

The figure shows (A) 1.0 % agarose gel electrophoresis of *HhaI* digestion patterns of the wild-type and mutant plasmids. The 2.25-kb mutant DNA band is indicated with the arrow.

Lane 1:  $\lambda$ /*HindIII* digested DNA marker

Lane 2: The *HhaI* digested wild-type plasmid, pMU388

Lane 3: The *HhaI* digested mutant plasmid, pY249L clone no. 1

Lane 4: The *HhaI* digested mutant plasmid, pY249L clone no. 2

(B) The DNA sequencing chromatogram of pY249L (clone no. 1), using N195A-f as a sequencing primer. Part of the sense strand sequence is shown. The bold letter represents the substituted amino acid residue.

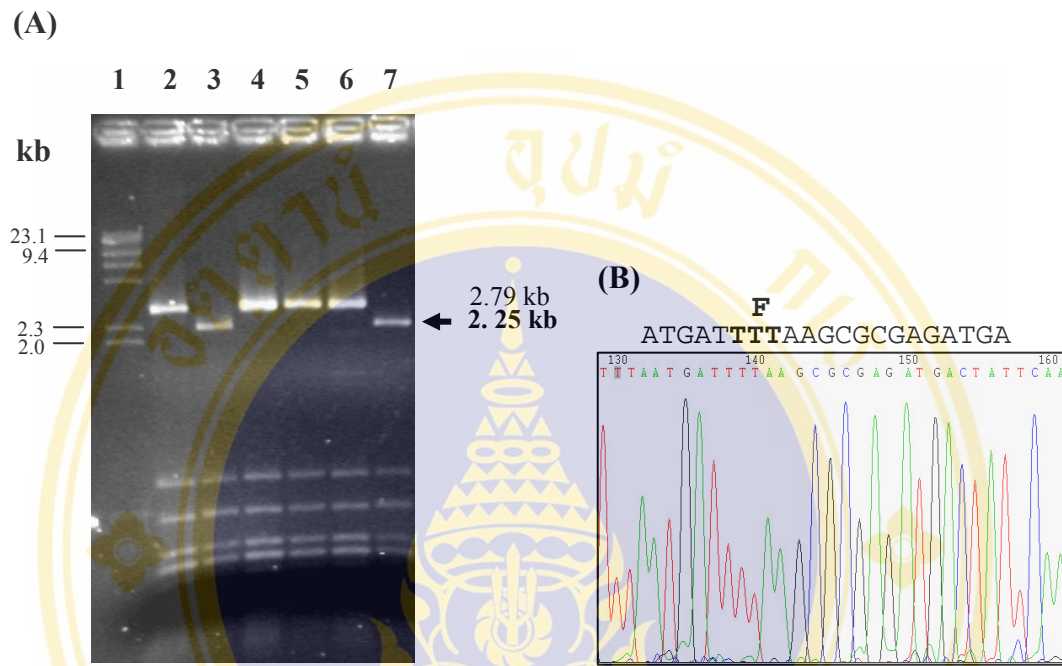


**Figure 4.19 Restriction digestion and DNA sequence analysis of pY249F**

The figure shows (A) 1.0 % agarose gel electrophoresis of *HhaI* digestion patterns of the wild-type and mutant plasmids. The 2.25-kb mutant DNA band is indicated with the arrow.

Lane 1:  $\lambda$ /*HindIII* digested DNA marker

Lane 2: The *HhaI* digested wild-type plasmid, pMU388

Lane 3: The *HhaI* digested mutant plasmid, pY249F clone no. 1

Lane 4: The *HhaI* digested mutant plasmid, pY249F clone no. 2

Lane 5: The *HhaI* digested mutant plasmid, pY249F clone no. 3

Lane 6: The *HhaI* digested mutant plasmid, pY249F clone no. 4

Lane 7: The *HhaI* digested mutant plasmid, pY249F clone no. 5

(B) The DNA sequencing chromatogram of pY249F (clone no. 5), using N195A-f as a sequencing primer. Part of the sense strand sequence is shown. The bold letter represents the substituted amino acid residue.

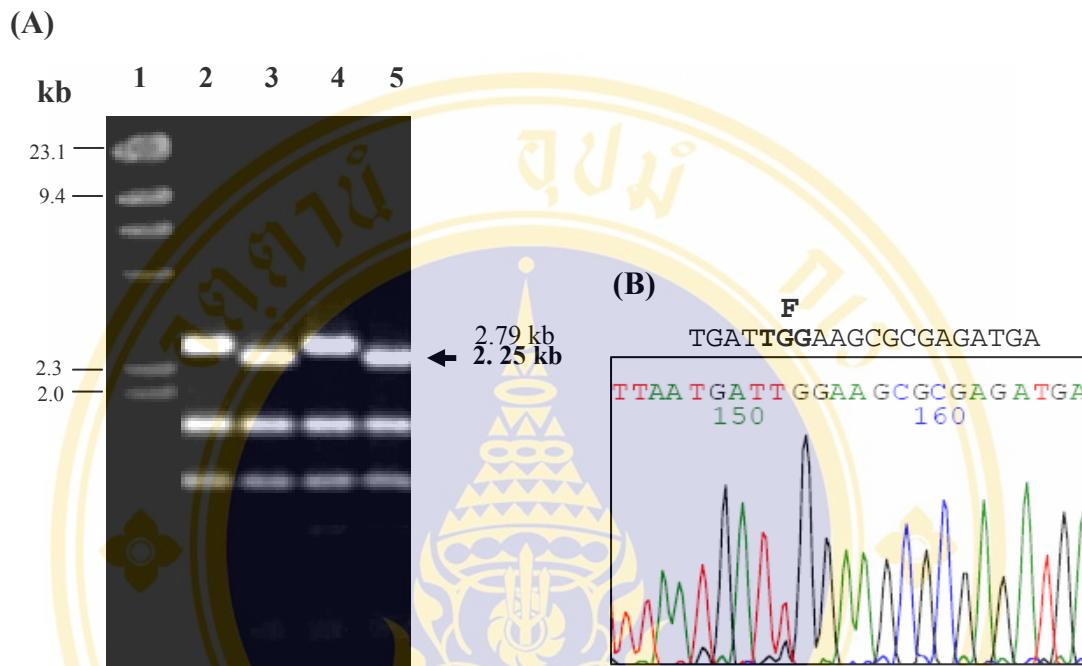


**Figure 4.20 Restriction digestion and DNA sequence analysis of pY249W**

The figure shows (A) 1.0 % agarose gel electrophoresis of *HhaI* digestion patterns of the wild-type and mutant plasmids. The 2.25-kb mutant DNA band is indicated with the arrow.

Lane 1 : $\lambda$ /*HindIII* digested DNA marker

Lane 2 :The *HhaI* digested wild-type plasmid, pMU388

Lane 3 :The *HhaI* digested mutant plasmid, pY249W clone no. 1

Lane 4 :The *HhaI* digested mutant plasmid, pY249W clone no. 2

Lane 5 :The *HhaI* digested mutant plasmid, pY249W clone no. 3

(B) The DNA sequencing chromatogram of pY249W (clone no. 1), using N195A-f as a sequencing primer. Part of the sense strand sequence is shown. The bold letter represents the substituted amino acid residue.

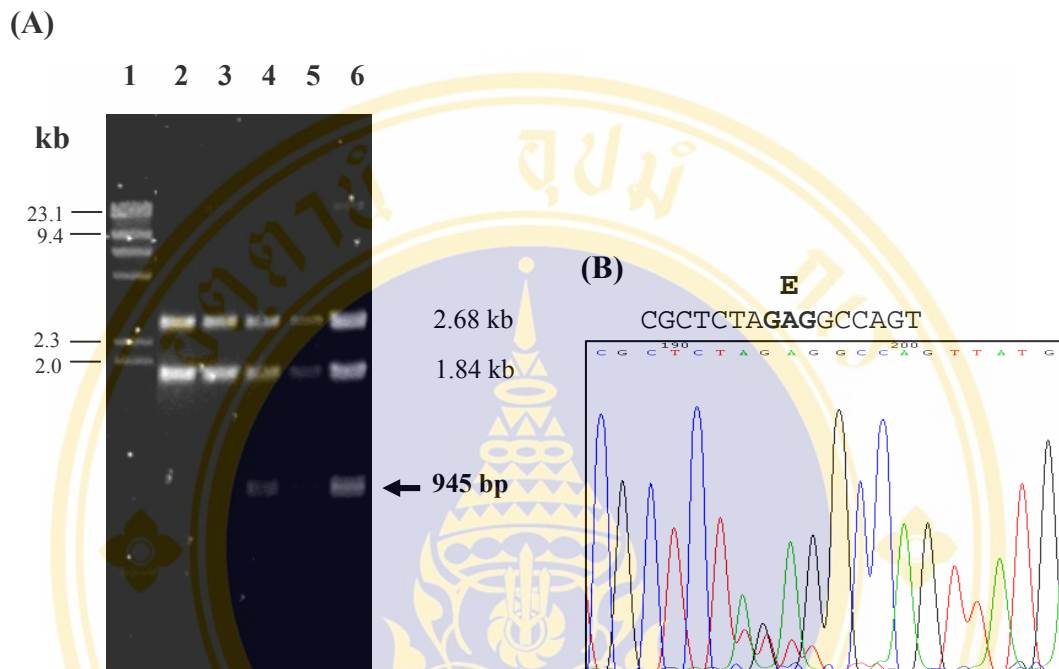


**Figure 4.21 Restriction digestion and DNA sequence analysis of pF264E**

The figure shows (A) 1.0 % agarose gel electrophoresis of *Xba*I digestion patterns of the wild-type and mutant plasmids. The 945-bp mutant DNA band is indicated with the arrow.

Lane 1:  $\lambda$ /*Hind*III digested DNA marker

Lane 2: The *Xba*I digested wild-type plasmid, pMU388

Lane 3: The *Xba*I digested mutant plasmid, pF264E clone no. 1

Lane 4: The *Xba*I digested mutant plasmid, pF264E clone no. 2

Lane 5: The *Xba*I digested mutant plasmid, pF264E clone no. 3

Lane 6: The *Xba*I digested mutant plasmid, pF264E clone no. 4

(B) The DNA sequencing chromatogram of pF264E (clone no. 4), using N195A-f as a sequencing primer. Part of the sense strand sequence is shown. The bold letter represents the substituted amino acid residue.

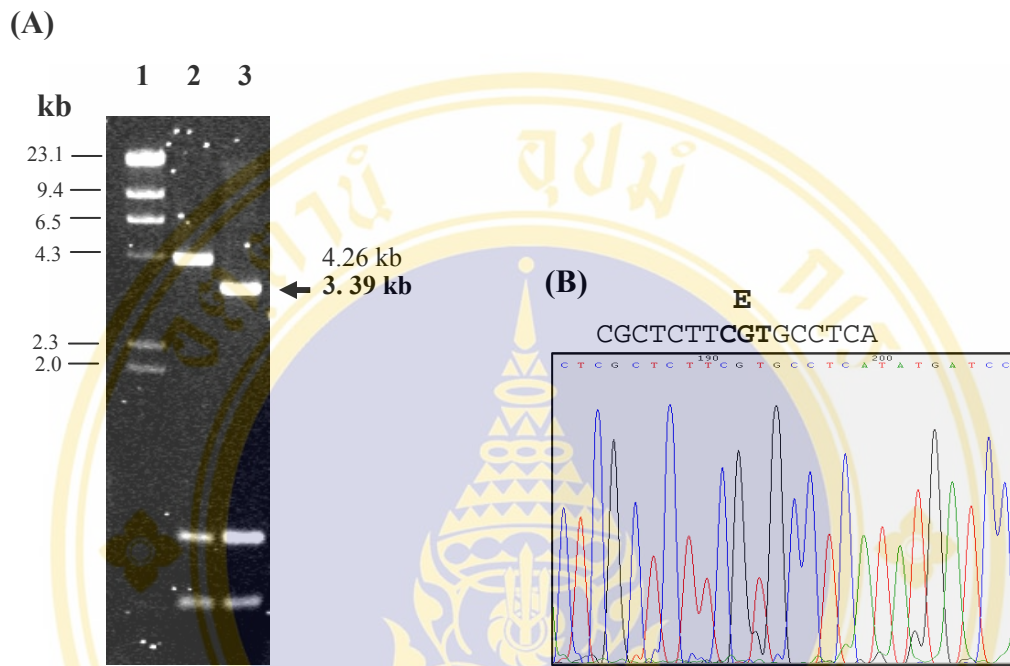


**Figure 4.22 Restriction digestion and DNA sequence analysis of pF264R**

The figure shows (A) 1.0 % agarose gel electrophoresis of *NdeI* digestion patterns of the wild-type and mutant plasmids. The 3.39-kb mutant DNA band is indicated with the arrow.

Lane 1:  $\lambda$ /*HindIII* digested DNA marker

Lane 2: The *NdeI* digested wild-type plasmid, pMU388

Lane 3: The *NdeI* digested mutant plasmid, pF264R

(B) The DNA sequencing chromatogram of pF264R, using N195A-f as a sequencing primer. Part of the sense strand sequence is shown. The bold letter represents the substituted amino acid residue.

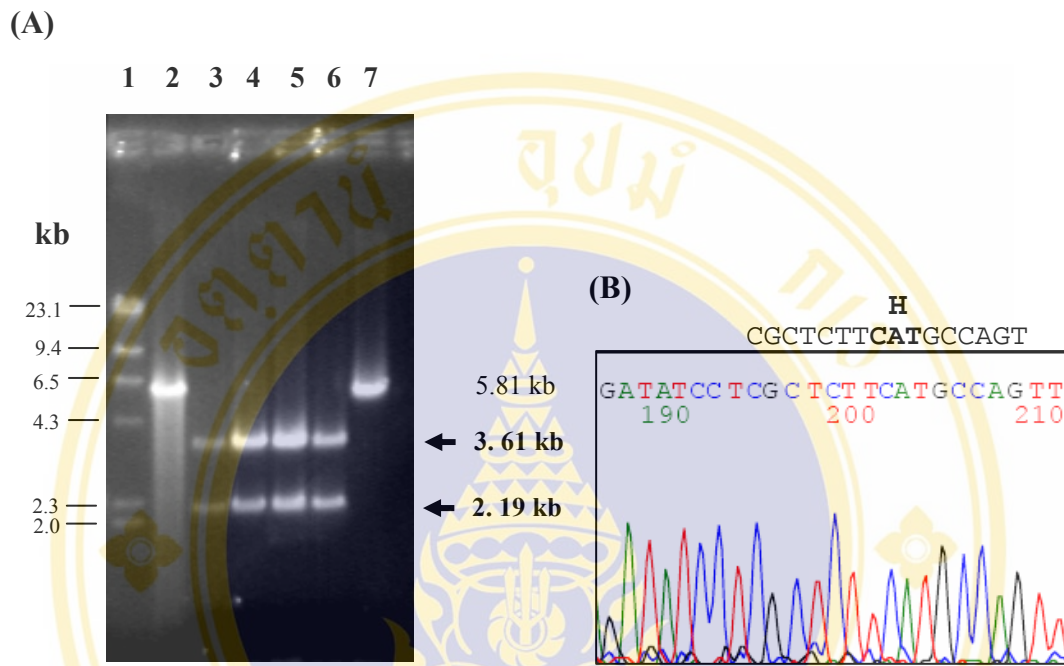


**Figure 4.23 Restriction digestion and DNA sequence analysis of pF264H**

The figure shows (A) 1.0 % agarose gel electrophoresis of *EcoRV* digestion patterns of the wild-type and mutant plasmids. The 3.61-kb and 2.19-kb mutant DNA bands are indicated with the arrows.

Lane 1:  $\lambda$ /*Hind*III digested DNA marker

Lane 2: The *EcoRV* digested wild-type plasmid, pMU388

Lane 3: The *EcoRV* digested mutant plasmid, pF264H clone no. 1

Lane 4: The *EcoRV* digested mutant plasmid, pF264H clone no. 2

Lane 5: The *EcoRV* digested mutant plasmid, pF264H clone no. 3

Lane 6: The *EcoRV* digested mutant plasmid, pF264H clone no. 4

Lane 7: The *EcoRV* digested mutant plasmid, pF264H clone no. 5

(B) The DNA sequencing chromatogram of pF264H (clone no. 4), using N195A-f as a sequencing primer. Part of the sense strand sequence is shown. The bold letter represents the substituted amino acid residue.

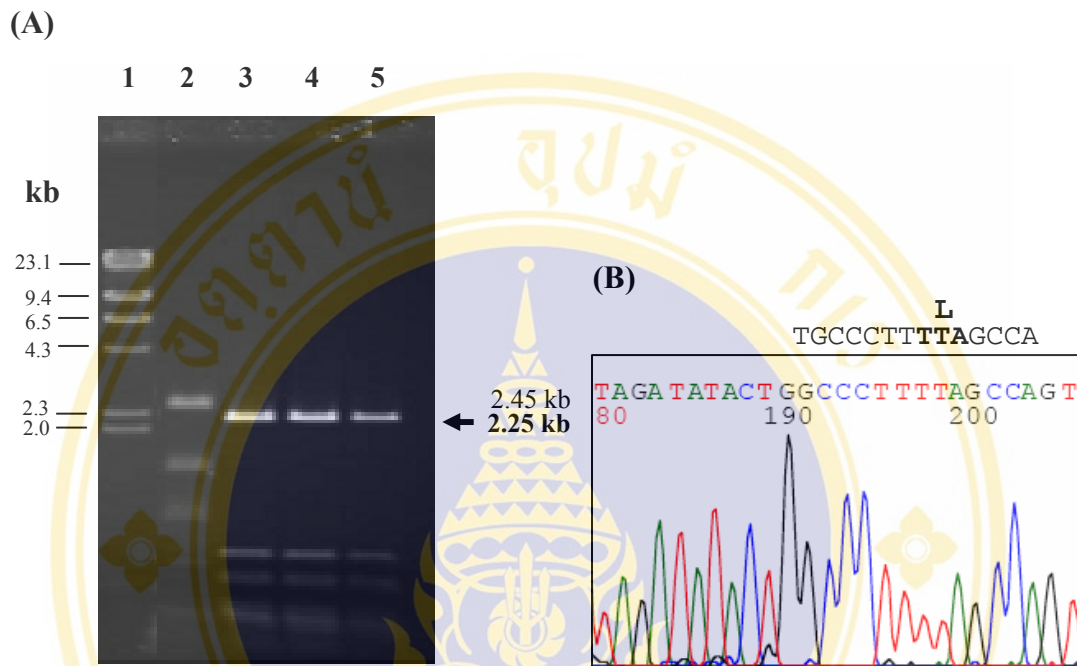


**Figure 4.24 Restriction digestion and DNA sequence analysis of pF264L**

The figure shows (A) 1.0 % agarose gel electrophoresis of *Sau96I* digestion patterns of the wild-type and mutant plasmids. The 2.25-kb mutant DNA band is indicated with the arrow.

Lane 1:  $\lambda$ /*HindIII* digested DNA marker

Lane 2: The *Sau96I* digested wild-type plasmid, pMU388

Lane 3: The *Sau96I* digested mutant plasmid, pF264L clone no. 1

Lane 4: The *Sau96I* digested mutant plasmid, pF264L clone no. 2

Lane 5: The *Sau96I* digested mutant plasmid, pF264L clone no. 3

(B) The DNA sequencing chromatogram of pF264L (clone no. 1), using N195A-f as a sequencing primer. Part of the sense strand sequence is shown. The bold letter represents the substituted amino acid residue.

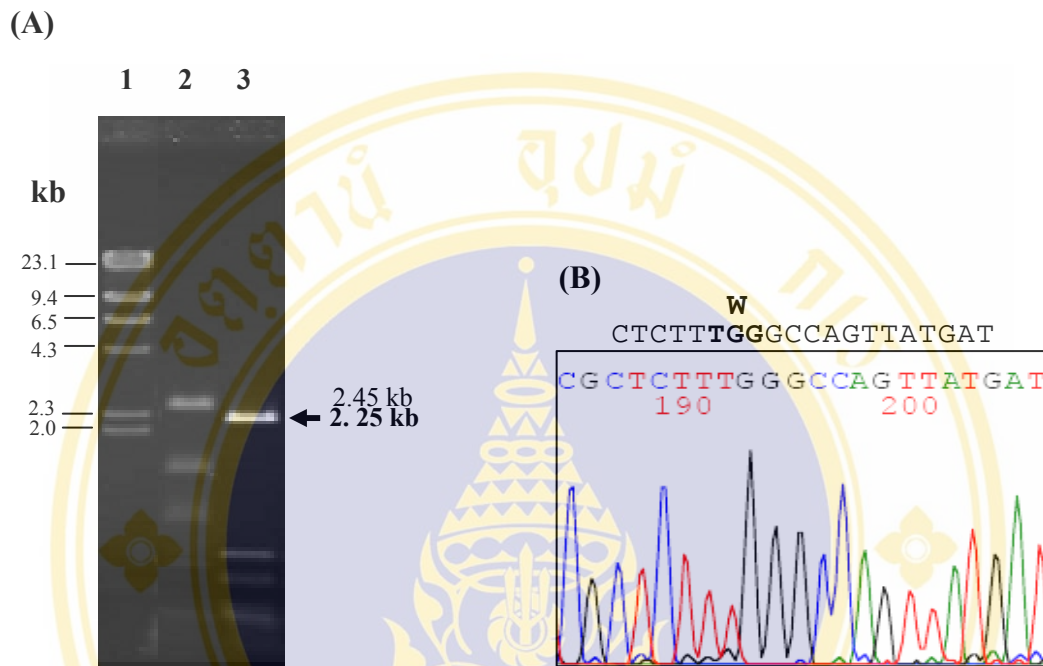


**Figure 4.25 Restriction digestion and DNA sequence analysis of pF264W**

The figure shows (A) 1.0 % agarose gel electrophoresis of *Sau96I* digestion patterns of the wild-type and mutant plasmids. The 2.25-kb mutant DNA band is indicated with the arrow.

Lane 1:  $\lambda$ /*HindIII* digested DNA marker

Lane 2: The *Sau96I* digested wild-type plasmid, pMU388

Lane 3: The *Sau96I* digested mutant plasmid, pF264W

(B) The DNA sequencing chromatogram of pF264W, using N195A-f as a sequencing primer. Part of the sense strand sequence is shown. The bold letter represents the substituted amino acid residue.

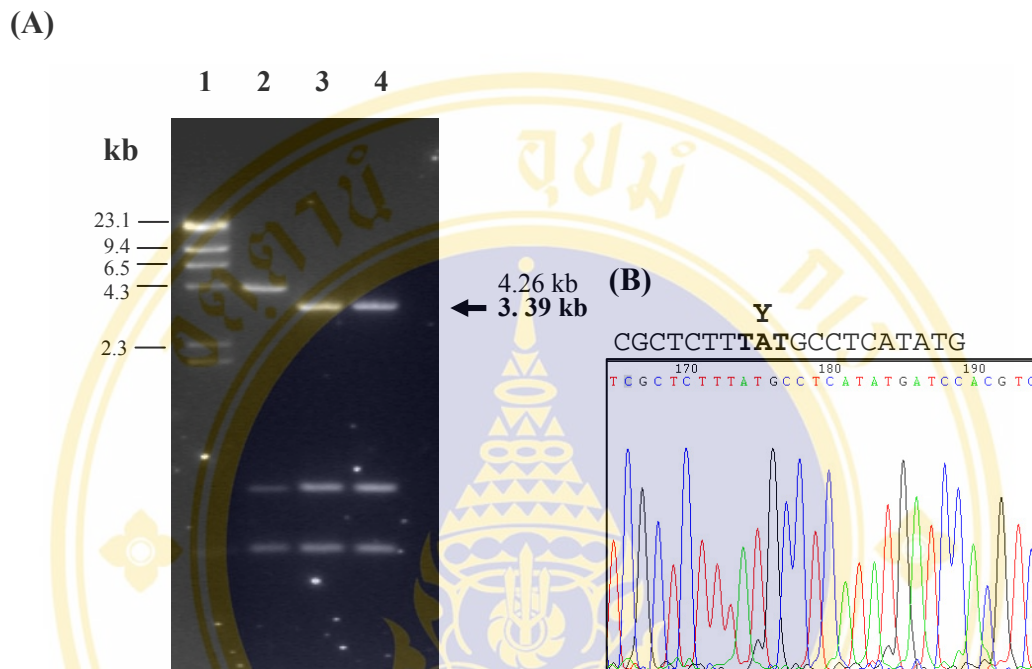


**Figure 4.26 Restriction digestion and DNA sequence analysis of pF264Y**

The figure shows (A) 1.0 % agarose gel electrophoresis of *NdeI* digestion patterns of the wild-type and mutant plasmids. The 3.39-kb mutant DNA band is indicated with the arrow.

Lane 1:  $\lambda$ /*HindIII* digested DNA marker

Lane 2: The *NdeI* digested wild-type plasmid, pMU388

Lane 3: The *NdeI* digested mutant plasmid, pF264Y clone no.1

Lane 4: The *NdeI* digested mutant plasmid, pF264Y clone no.2

(B) The DNA sequencing chromatogram of pF264Y (clone no. 1), using N195A-f as a sequencing primer. Part of the sense strand sequence is shown. The bold letter represents the substituted amino acid residue.

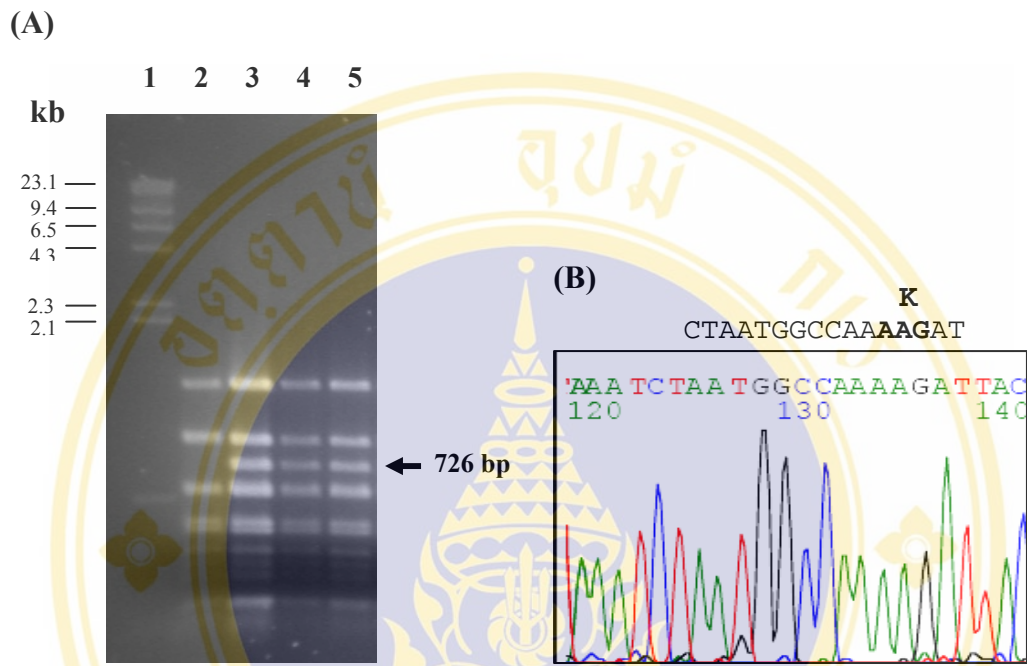


**Figure 4.27 Restriction digestion and DNA sequence analysis of pW243K**

The figure shows (A) 1.0 % agarose gel electrophoresis of *Hae*III digestion patterns of the wild-type and mutant plasmids. The 726-bp mutant DNA band is indicated with the arrow.

Lane 1:  $\lambda$ /*Hind*III digested DNA marker

Lane 2: The *Hae*III digested wild-type plasmid, pMU388

Lane 3: The *Hae*III digested mutant plasmid, pW243K clone no. 1

Lane 4: The *Hae*III digested mutant plasmid, pW243K clone no. 2

Lane 5: The *Hae*III digested mutant plasmid, pW243K clone no. 3

(B) The DNA sequencing chromatogram of pW243K (clone no. 3), using N195A-f as a sequencing primer. Part of the sense strand sequence is shown. The bold letter represents the substituted amino acid residue.

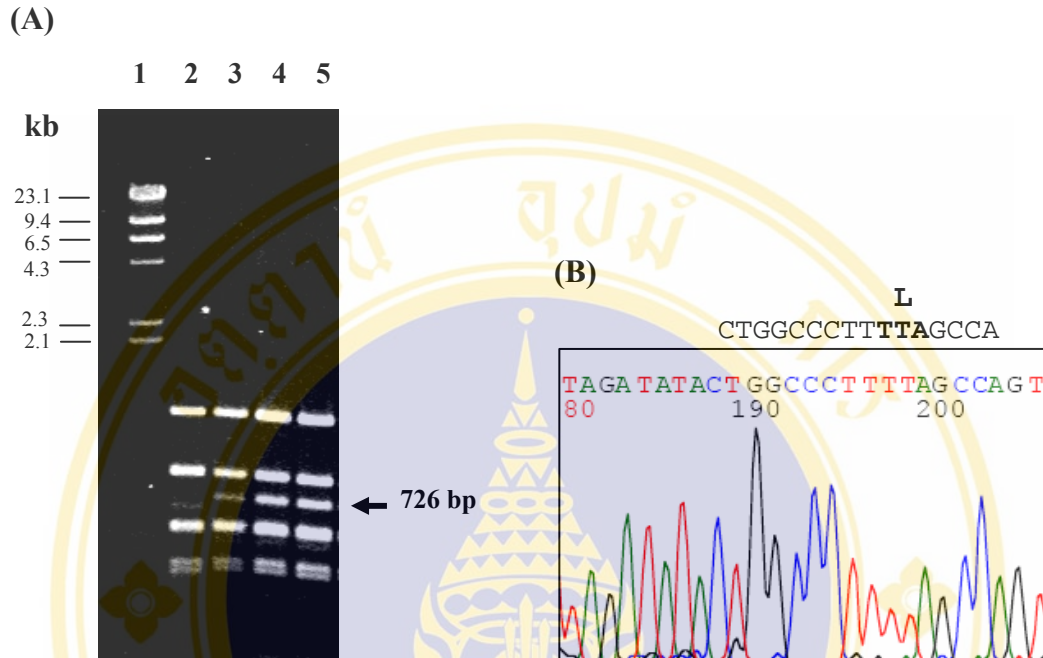


**Figure 4.28 Restriction digestion and DNA sequence analysis of pW243L**

The figure shows (A) 1.0 % agarose gel electrophoresis of *Hae*III digestion patterns of the wild-type and mutant plasmids. The 726-bp mutant DNA band is indicated with the arrow.

Lane 1:  $\lambda$ /*Hind*III digested DNA marker

Lane 2: The *Hae*III digested wild-type plasmid, pMU388

Lane 3: The *Hae*III digested mutant plasmid, pW243L clone no. 1

Lane 4: The *Hae*III digested mutant plasmid, pW243L clone no. 2

Lane 5: The *Hae*III digested mutant plasmid, pW243L clone no. 3

(B) The DNA sequencing chromatogram of pW243L (clone no. 2), using N195A-f as a sequencing primer. Part of the sense strand sequence is shown. The bold letter represents the substituted amino acid residue.

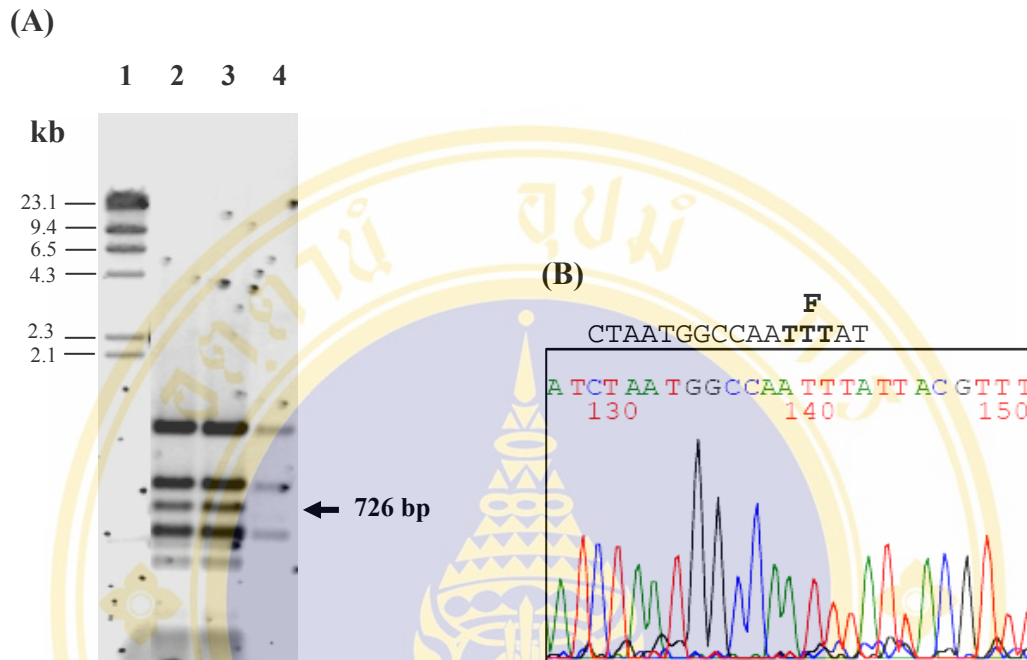


**Figure 4.29 Restriction digestion and DNA sequence analysis of pW243F**

The figure shows (A) 1.0 % agarose gel electrophoresis of *Hae*III digestion patterns of the wild-type and mutant plasmids. The 726-bp mutant DNA band is indicated with the arrow.

Lane 1:  $\lambda$ /*Hind*III digested DNA marker

Lane 2: The *Hae*III digested mutant plasmid, pW243F clone no. 1

Lane 3: The *Hae*III digested mutant plasmid, pW243F clone no. 2

Lane 4: The *Hae*III digested wild-type plasmid, pMU388

(B) The DNA sequencing chromatogram of pW243F (clone no. 1), using N195A-f as a sequencing primer. Part of the sense strand sequence is shown. The bold letter represents the substituted amino acid residue.

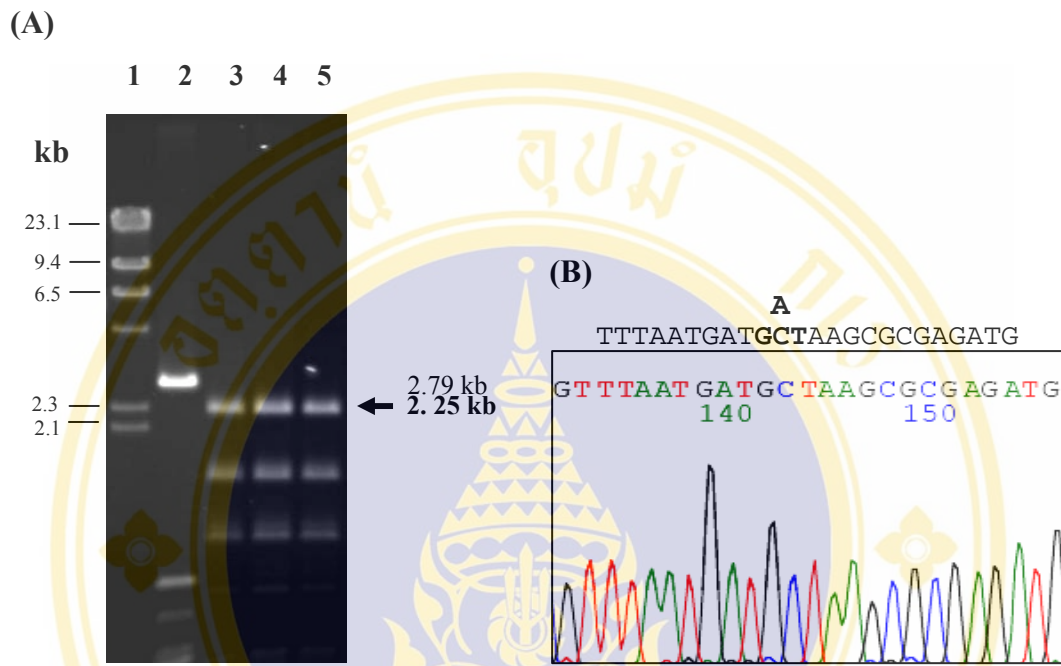


**Figure 4.30 Restriction digestion and DNA sequence analysis of pF264A/Y249A**

The figure shows (A) 1.0 % agarose gel electrophoresis of *HhaI* digestion patterns of the wild-type and mutant plasmids. The 2.25-bp mutant DNA band is indicated with the arrow.

Lane 1:  $\lambda$ /*HindIII* digested DNA marker

Lane 2: The *HhaI* digested wild-type plasmid, pMU388

Lane 3: The *HhaI* digested mutant plasmid, pF264A/Y249A clone no. 1

Lane 4: The *HhaI* digested mutant plasmid, pF264A/Y249A clone no. 2

Lane 5: The *HhaI* digested mutant plasmid, pF264A/Y249A clone no. 3

(B) The DNA sequencing chromatogram of pF264A/Y249A (clone no. 1), using N195A-f as a sequencing primer. Part of the sense strand sequence is shown. The bold letter represents the substituted amino acid residue.

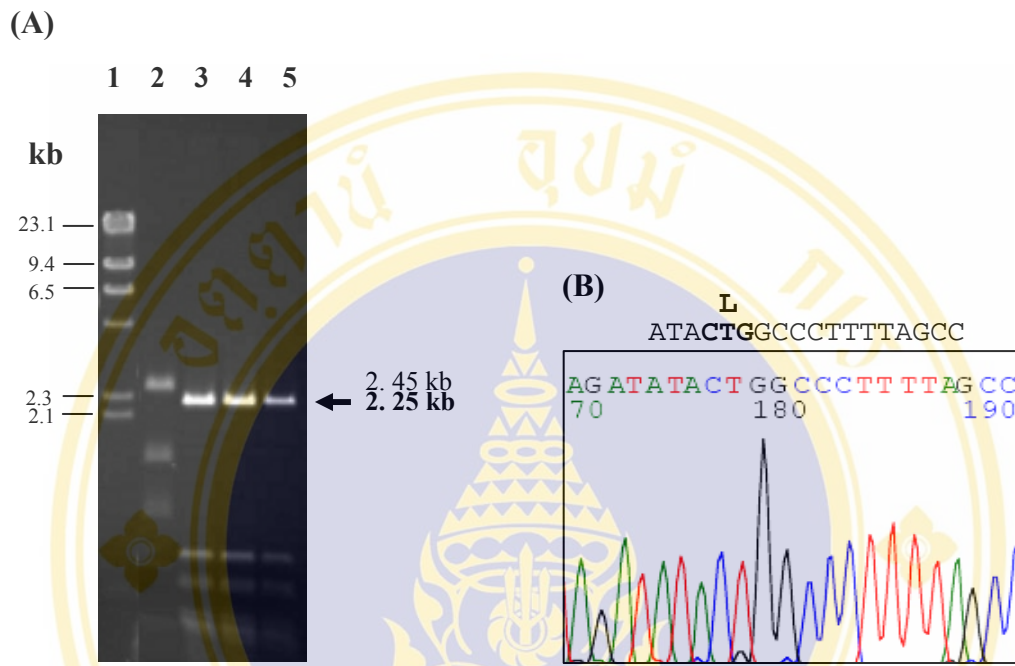


**Figure 4.31 Restriction digestion and DNA sequence analysis of pY249L/F264L**

The figure shows (A) 1.0 % agarose gel electrophoresis of *Sau*96I digestion patterns of the wild-type and mutant plasmids. The 2.25-bp mutant DNA band is indicated with the arrow.

Lane 1:  $\lambda$ /*Hind*III digested DNA marker

Lane 2: The *Sau*96I digested wild-type plasmid, pMU388

Lane 3: The *Sau*96I digested mutant plasmid, pY249L/F264L clone no. 1

Lane 4: The *Sau*96I digested mutant plasmid, pY249L/F264L clone no. 2

Lane 5: The *Sau*96I digested mutant plasmid, pY249L/F264L clone no. 3

(B) The DNA sequencing chromatogram of pY249L/F264L (clone no. 2), using N195A-f as a sequencing primer. Part of the sense strand sequence is shown. The bold letter represents the substituted amino acid residue.

#### 4.6 Expression of the Cry4Ba mutant toxins

When each mutant toxin was expressed in *E. coli* upon IPTG induction at 30°C for 10 h, all were produced as inclusion bodies, and the expression level of the 130-kDa mutant protoxins was approximately the same as that of the wild-type toxin as shown in **Figures 4.32-4.34**.

#### 4.7 Larvicidal activity of Cry4Ba mutant toxins

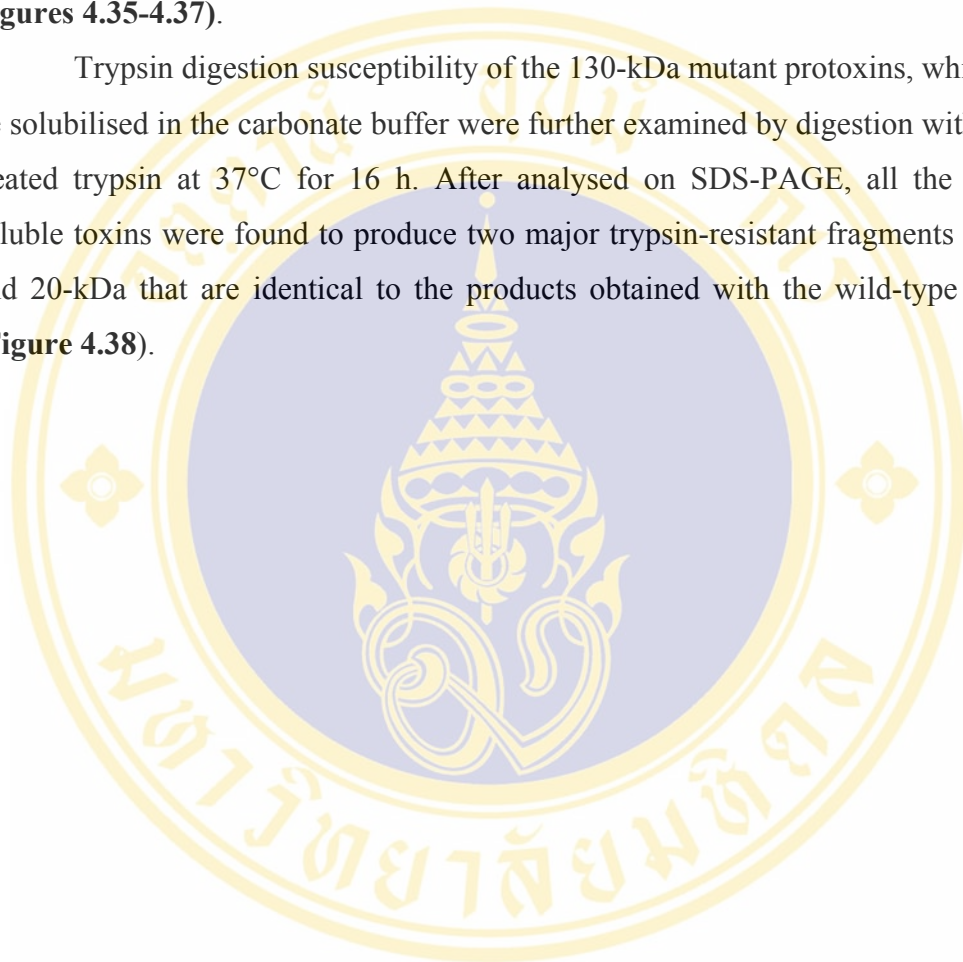
*E. coli* cells expressing each mutant toxin were tested for their relative biological activity against *S. aegypti* mosquito larvae. The mortality data recorded after 24-h incubation revealed that only *E. coli* cells expressing the mutants that were replaced with an aromatic residue, Y249F or Y249W and F264Y or F264W, still retained relatively high levels of larvicidal activity. On the other hand, single substitutions of either Tyr<sup>249</sup> or Phe<sup>264</sup> with a hydrophobic residue (*i.e.* Leu) showed an adverse effect on larvicidal activity comparable to the single-alanine substitutions (Y249A and F264A) (see **Figure 4.10**), whilst replacements with charged (*i.e.* Glu or Arg) or non-charged polar (*i.e.* His) residues almost completely abolished the larvicidal activity. In addition, two double mutants, Y249L/F264L and F264A/Y249A revealed a drastically higher loss in mosquito-larvicidal activity when compared to their corresponding single mutants. Interestingly, while *E. coli* cells expressing the W243K mutant showed a severe loss in larvicidal activity, the cells expressing either W243L or W243F still exerted high toxicity apparently at the same level (approximately 60% of the wild-type control value). As can be observed that protoxin inclusions gave similar results for the observed activity (see **Figures 4.39-4.40**).

#### 4.8 Solubilisation and proteolytic processing of the Cry4Ba mutant toxins

Experiments were also conducted to assess the solubility *in vitro* of the mutant protein inclusions in comparison with that of the wild-type. It was found that all the toxin inclusions of the larvicidal-active mutants that were substituted with an aromatic residue (W243F, Y249F, Y249W, F264Y and F264W) were found to be soluble in the carbonate buffer, giving at least 70-80% solubility which is comparable to that of the wild-type and the F246A larvicidal-active mutant under similar conditions. In addition, toxin inclusions of the W243K, W243L, Y249L, F264L and

Y249L/F264L mutants were also observed to be relatively soluble in this buffer (approximately 60% solubility). On the other hand, a complete loss of the inclusion solubility was found for all the remaining mutants (Y249E, Y249R, Y249H, F264E, F264R, F264H and F264A/Y249A, which all exhibited a severe loss in toxicity. (see **Figures 4.35-4.37**).

Trypsin digestion susceptibility of the 130-kDa mutant protoxins, which could be solubilised in the carbonate buffer were further examined by digestion with TPCK-treated trypsin at 37°C for 16 h. After analysed on SDS-PAGE, all the 130-kDa soluble toxins were found to produce two major trypsin-resistant fragments of ca. 47 and 20-kDa that are identical to the products obtained with the wild-type protoxin (**Figure 4.38**).



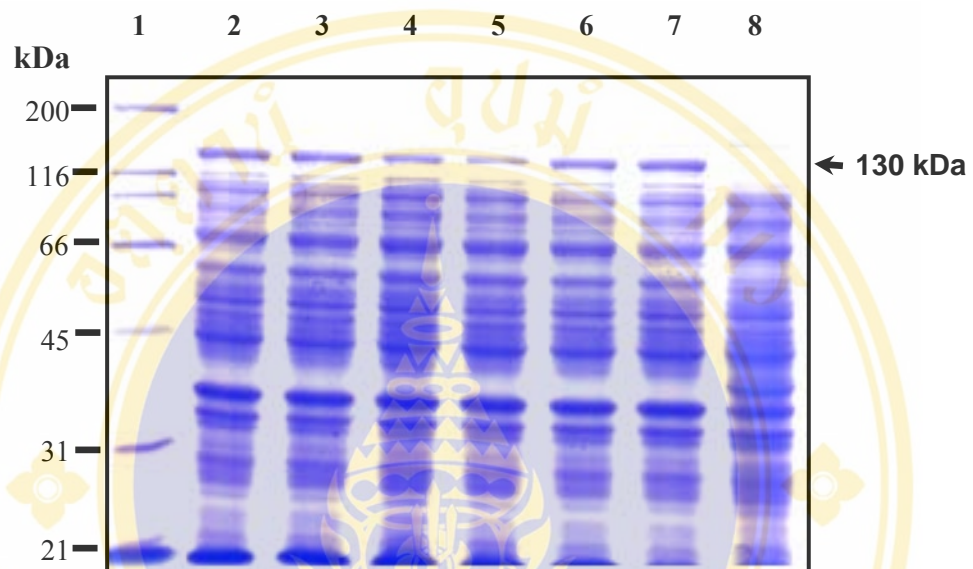


**Figure 4.32 Expression of the Trp-243 and double mutants**

The figure shows SDS-PAGE protein profile (Coomassie blue-stained 10% gel) of crude extracts from IPTG induced *E. coli* containing different mutant plasmids. The expected 130-kDa protoxin band is indicated by the arrow.

Lane 1: Molecular mass protein standards

Lane 2: Crude extracted proteins of *E. coli* containing pMU388

Lane 3: Crude extracted proteins of *E. coli* containing pW243K

Lane 4: Crude extracted proteins of *E. coli* containing pW243L

Lane 5: Crude extracted proteins of *E. coli* containing pW243F

Lane 6: Crude extracted proteins of *E. coli* containing pY249L/F264L

Lane 7: Crude extracted proteins of *E. coli* containing pF264A/Y249A

Lane 8: Crude extracted proteins of *E. coli* containing pUC12

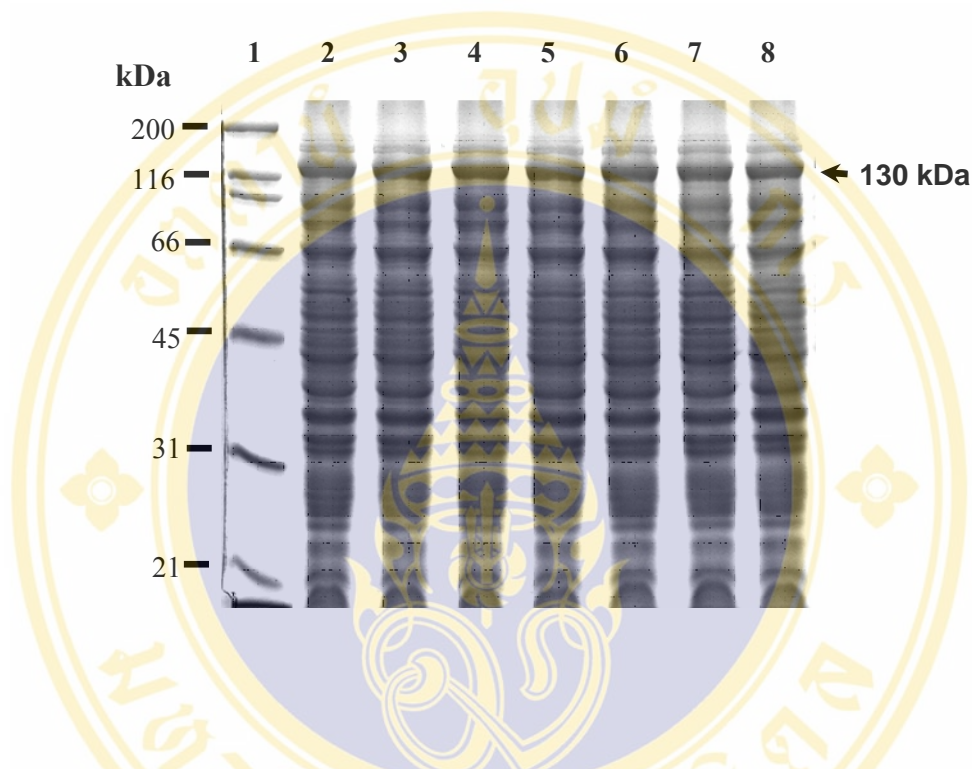


**Figure 4.33 Expression of the Tyr-249 mutants**

The figure shows SDS-PAGE protein profile (Coomassie blue-stained 10% gel) of crude extracts from IPTG induced *E. coli* containing different mutant plasmids. The expected 130-kDa protoxin band is indicated by the arrow.

Lane 1: Molecular mass protein standards

Lane 2: Crude extracted proteins of *E. coli* containing pMU388

Lane 3: Crude extracted proteins of *E. coli* containing pY249E

Lane 4: Crude extracted proteins of *E. coli* containing pY249R

Lane 5: Crude extracted proteins of *E. coli* containing pY249H

Lane 6: Crude extracted proteins of *E. coli* containing pY249F

Lane 7: Crude extracted proteins of *E. coli* containing pY249W

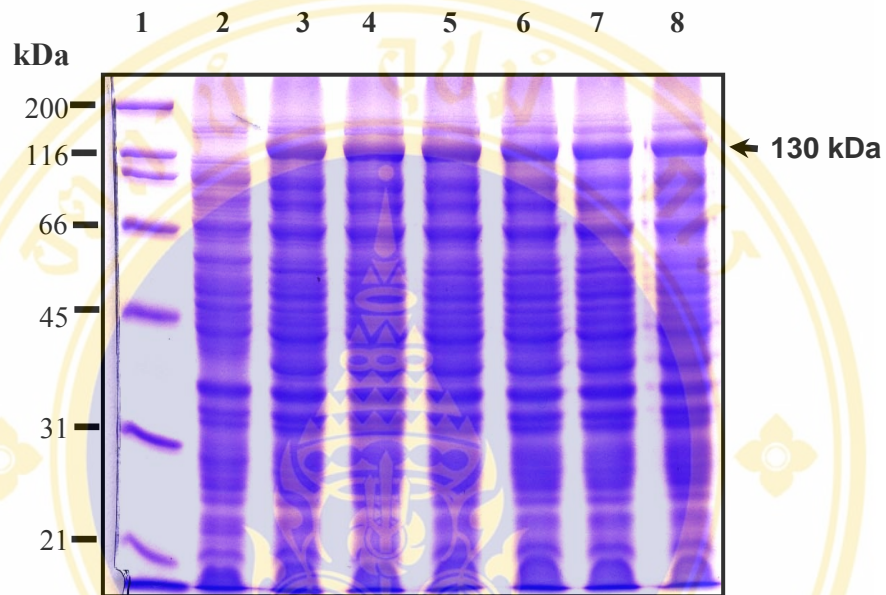


**Figure 4.34 Expression of the Phe-264 mutants**

The figure shows SDS-PAGE protein profile (Coomassie blue-stained 10% gel) of crude extracts from IPTG induced *E. coli* containing different mutant plasmids. The expected 130-kDa protoxin band is indicated by the arrow.

Lane 1: Molecular mass protein standards

Lane 2: Crude extracted proteins of *E. coli* containing pUC12

Lane 3: Crude extracted proteins of *E. coli* containing pMU388

Lane 4: Crude extracted proteins of *E. coli* containing pF264E

Lane 5: Crude extracted proteins of *E. coli* containing pF264R

Lane 6: Crude extracted proteins of *E. coli* containing pF264H

Lane 7: Crude extracted proteins of *E. coli* containing pF264Y

Lane 8: Crude extracted proteins of *E. coli* containing pF264W

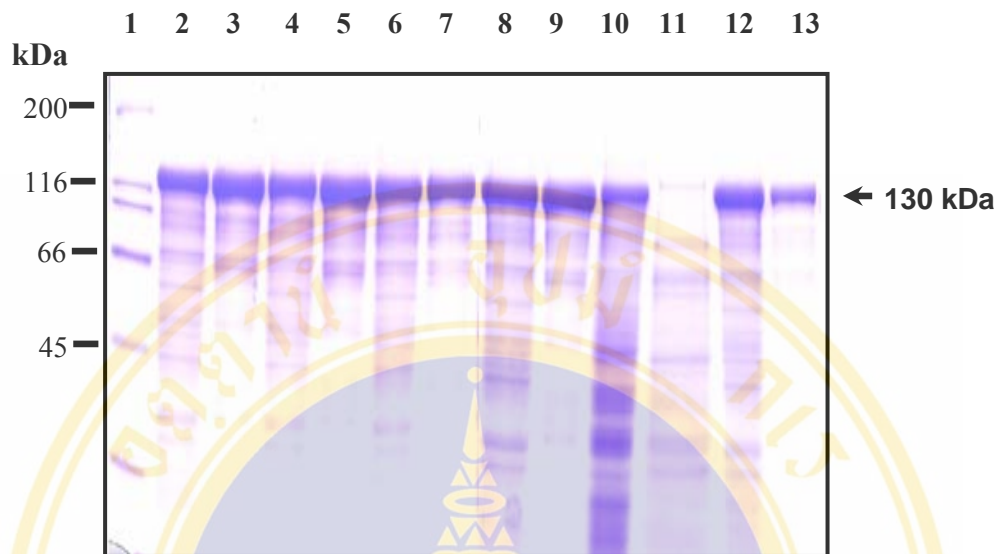


**Figure 4.35 Solubility of Trp-243 and double mutant inclusions**

The figure shows SDS-PAGE (Coomassie blue-stained 10% gel) comparing the solubility of the mutant inclusions in 50 mM carbonate buffer, pH 10.0 at 37°C for 1 h. The expected 130-kDa protoxin band is indicated by the arrow.

- Lane 1: Molecular mass protein standards
- Lane 2: The partially purified Cry4Ba inclusion
- Lane 3: The solubilised Cry4Ba fraction
- Lane 4: The partially purified W243F inclusion
- Lane 5: The solubilised fraction of W243F
- Lane 6: The partially purified W243K inclusion
- Lane 7: The solubilised fraction of W243K
- Lane 8: The partially purified W243L inclusion
- Lane 9: The solubilised fraction of W243L
- Lane 10: The partially purified F264A/Y249A inclusion
- Lane 11: The solubilised fraction of F264A/Y249A
- Lane 12: The partially purified Y249L/F264L inclusion
- Lane 13: The solubilised fraction of Y249L/F264L

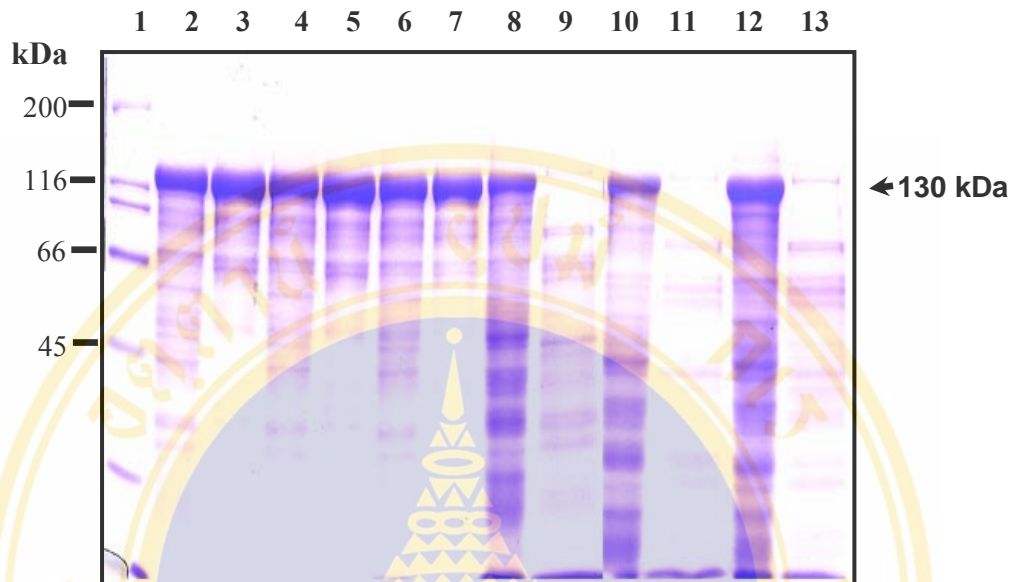


**Figure 4.36 Solubility of Tyr-249 mutant inclusions**

The figure shows SDS-PAGE (Coomassie blue-stained 10% gel) comparing the solubility of the mutant inclusions in 50 mM carbonate buffer, pH 10.0 at 37°C for 1 h. The expected 130-kDa protoxin band is indicated by the arrow.

- Lane 1: Molecular mass protein standards
- Lane 2: The partially purified Y249F inclusion
- Lane 3: The solubilised fraction of Y249F
- Lane 4: The partially purified Y249W inclusion
- Lane 5: The solubilised fraction of Y249W
- Lane 6: The partially purified Y249L inclusion
- Lane 7: The solubilised fraction of Y249L
- Lane 8: The partially purified Y249E inclusion
- Lane 9: The solubilised fraction of Y249E
- Lane 10: The partially purified Y249R inclusion
- Lane 11: The solubilised fraction of Y249R
- Lane 12: The partially purified Y249H inclusion
- Lane 13: The solubilised fraction of Y249H

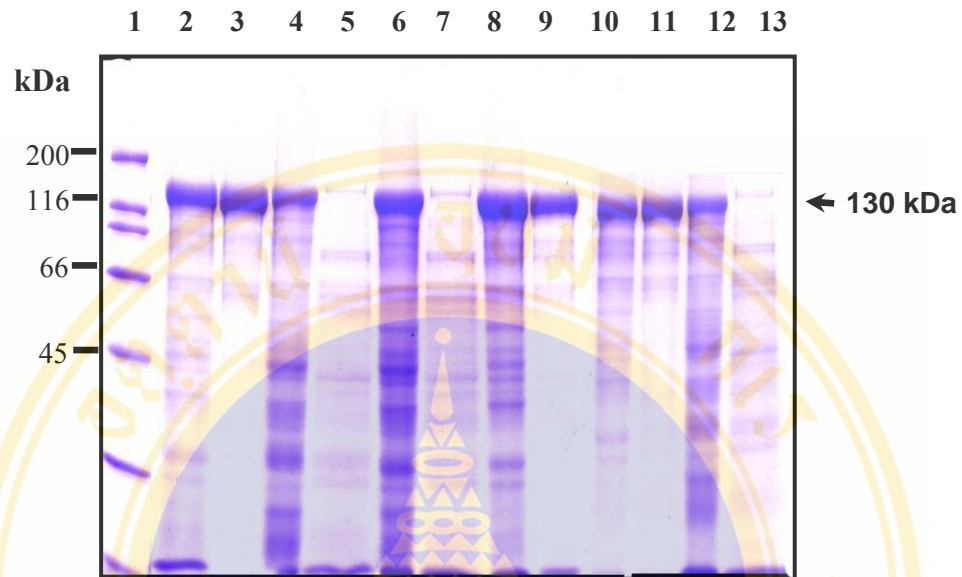


**Figure 4.37 Solubility of Phe-264 mutant inclusions**

The figure shows SDS-PAGE (Coomassie blue-stained 10% gel) comparing the solubility of the mutant inclusions in 50 mM carbonate buffer, pH 10.0 at 37°C for 1 h. The expected 130-kDa protoxin band is indicated by the arrow.

- Lane 1: Molecular mass protein standards
- Lane 2: The partially purified F264Y inclusion
- Lane 3: The solubilised fraction of F264Y
- Lane 4: The partially purified F264E inclusion
- Lane 5: The solubilised fraction of F264E
- Lane 6: The partially purified F264R inclusion
- Lane 7: The solubilised fraction of F264R
- Lane 8: The partially purified F264W inclusion
- Lane 9: The solubilised fraction of F264W
- Lane 10: The partially purified F264L inclusion
- Lane 11: The solubilised fraction of F264L
- Lane 12: The partially purified F264H inclusion
- Lane 13 :The solubilised fraction of F264H

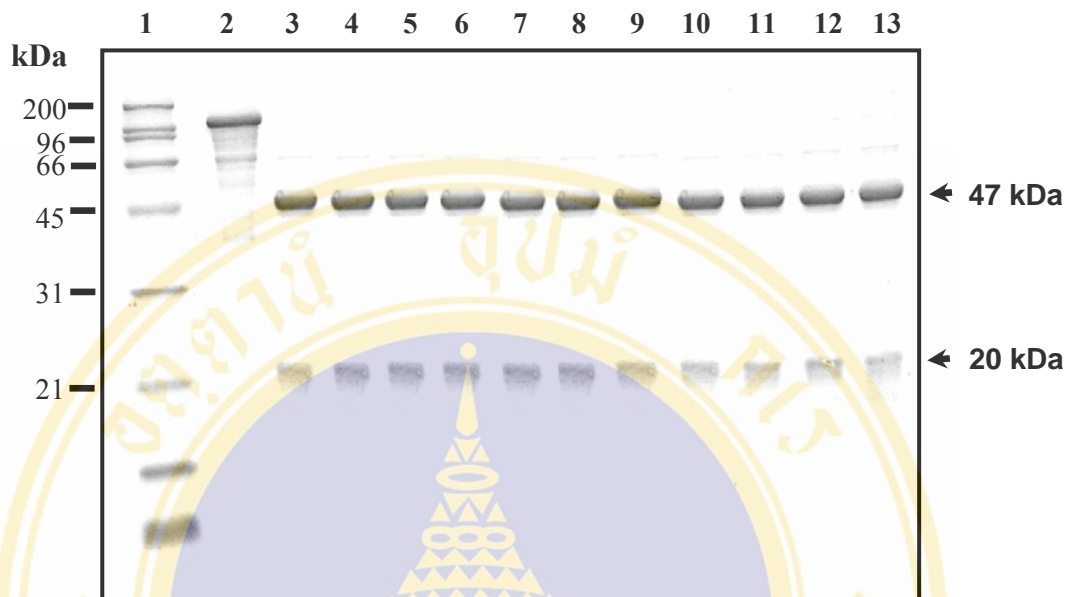


**Figure 4.38** Trypsinised products of the Cry4Ba toxin and its mutants

The figure shows SDS-PAGE (15% Coomassie blue-stained gel) of the trypsin treated products of Cry4Ba and its mutants. The expected bands of ca. 47 and ca. 20-kDa are indicated.

- Lane 1: Molecular mass protein standards
- Lane 2: The 130-kDa trypsin-untreated product
- Lane 3: Trypsin treated products of Cry4Ba wild-type
- Lane 4: Trypsin treated products of W243K
- Lane 5: Trypsin treated products of W243L
- Lane 6: Trypsin treated products of W243F
- Lane 7: Trypsin treated products of Y249L
- Lane 8: Trypsin treated products of Y249F
- Lane 9: Trypsin treated products of Y249W
- Lane 10: Trypsin treated products of F264L
- Lane 11: Trypsin treated products of F264Y
- Lane 12: Trypsin treated products of F264W
- Lane 13: Trypsin treated products of Y249L/F264L

Toxin	% Mortality										
	pUC12	pMU388	W243F	W243L	W243K	Y249E	Y249R	Y249H	Y249F	Y249W	Y249L
Mean	2.3	81.3	62.0	46.0	16.0	3.0	3.0	12.3	71.3	61.7	26.0
SEM	1.5	6.6	5.5	10.7	3.2	1.3	1.6	2.0	4.5	4.5	8.6

Toxin	% Mortality									
	pUC12	pMU388	F264E	F264R	F264H	F264L	F264Y	F264W	Y249L/F264L	F264A/Y249A
Mean	2.3	81.3	3.3	2.5	6.3	29.3	70.0	70.9	2.0	2.0
SEM	1.5	6.6	1.5	2.0	3.2	8.9	5.7	5.1	1.0	1.0

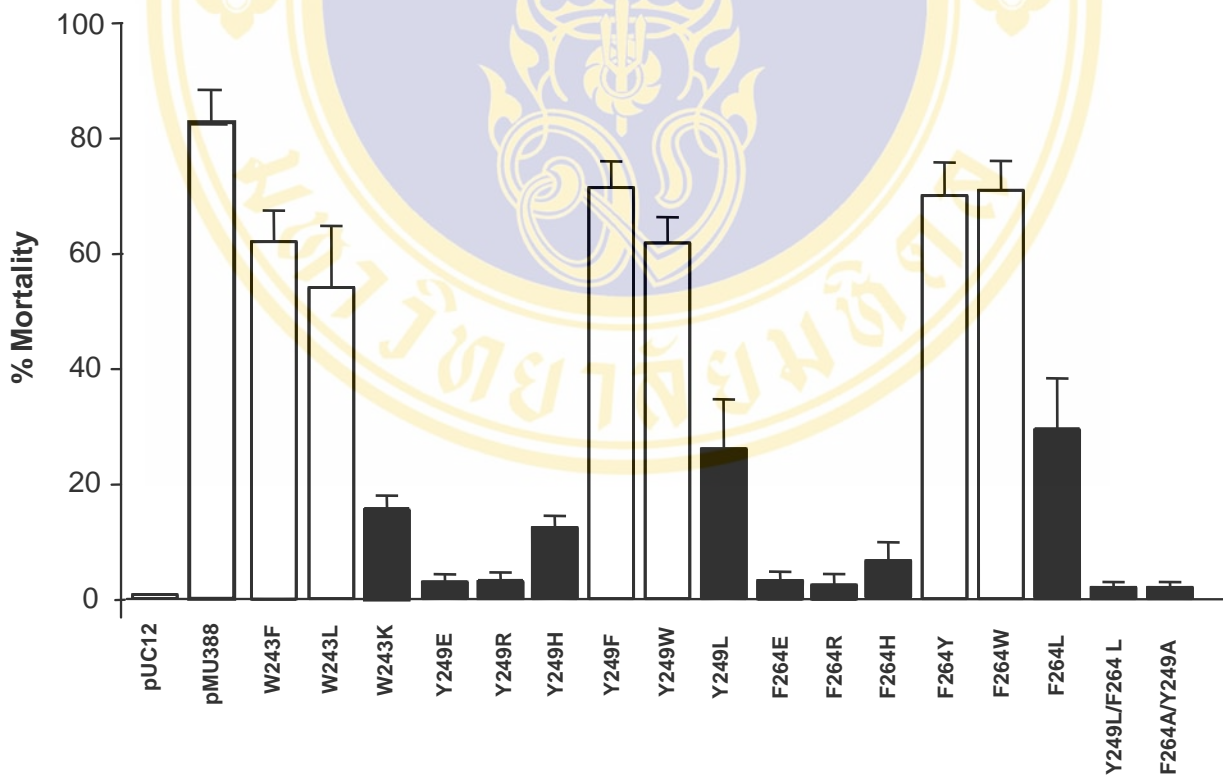


**Figure 4.39 Larvicidal activity using Cry4Ba mutant toxins**

The figure shows larvicidal activity of the wild-type Cry4Ba and its mutant toxins against *S. aegypti* larvae using *E. coli* cells. Error bars represent standard errors of the mean from three independent experiments.

Toxin	% Mortality									
	pMU388	W243F	W243L	W243K	Y249E	Y249R	Y249H	Y249F	Y249W	Y249L
Mean	100.0	86.6	75.0	10.0	8.3	5.0	4.2	65.0	61.7	6.7
SEM	0.0	5.0	6.7	4.5	2.2	3.1	1.7	7.6	4.0	3.3

Toxin	% Mortality								
	pMU388	F264E	F264R	F264H	F264Y	F264W	F264L	Y249L/F264L	F264A/Y249A
Mean	100.0	3.3	8.3	3.3	72.9	72.5	26.7	6.7	3.3
SEM	0.0	2.1	3.1	2.1	6.0	8.6	6.2	3.3	3.1

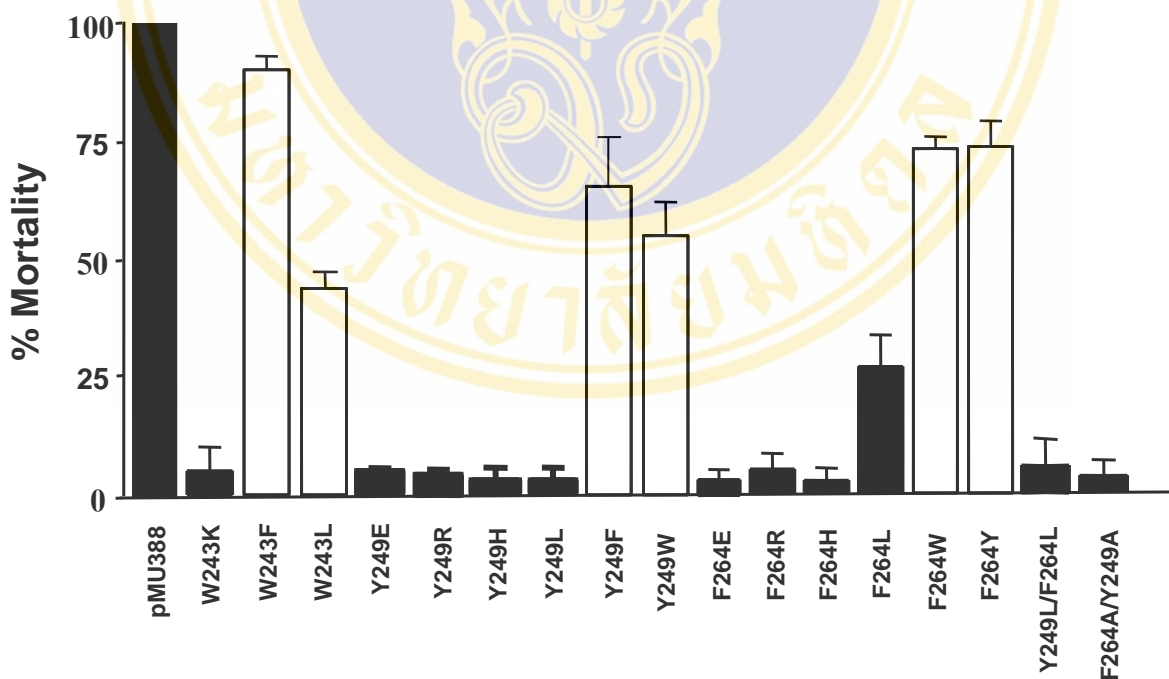


**Figure 4.40 Larvicidal activity Cry4Ba mutants**

The figure shows larvicidal activity of the wild-type Cry4Ba and its mutant toxins against *S. aegypti* larvae using 5 µg protoxin inclusions. Error bars represent standard errors of the mean from three independent experiments.

## CHAPTER V

### RESULTS: FUNCTIONAL CHARACTERISATION OF CONSERVED AROMATICITY IN CRY4Ba-HELIX 7

As mentioned earlier,  $\alpha 7$  may serve as a binding sensor that could initiate the binding of the pore-forming domain to the lipid membrane, facilitating the membrane insertion of the  $\alpha 4$ - $\alpha 5$  hairpin (78). This helix has also been implicated in ion-channel activity and receptor-binding affinity of Cry1A toxins (23,85), or structural stability and crystallisation of Cry3Aa (86). However, the functional importance for toxicity of the structurally conserved aromaticity in this helix has not been clearly highlighted.

#### 5.1 Purification of Cry4Ba and its mutant toxins

The 65-kDa trypsin-activated Cry4Ba wild-type and three selected mutant toxins were subjected to size-exclusion FPLC (Superdex 200), which was equilibrated with carbonate buffer (pH 10.0). Similar to the Cry4Ba wild-type toxin, the purified trypsin-treated mutant toxins (Y249L, F264L and Y249L/F264L) that are composed of 47 and 20-kDa fragments were eluted from the column in a distinct single peak corresponding to the eluted fractions of the 66-kDa BSA protein marker (**Figure 5.1A**). These fractions were then analysed on SDS-PAGE (see **Figure 5.1B**).

#### 5.2 Secondary structure of Cry4Ba and its mutants

To further determine if the leucine substitutions would induce structural changes in these three mutants, the sum of the secondary structure components of the FPLC-purified trypsin-treated mutants, Y249L, F264L and Y249L/F264L, were studied by far-UV CD spectroscopy in comparison with that of the 65-kDa purified wild-type toxin. As shown in **Figure 5.2**, it is found that all the CD profiles are basically similar, particularly the spectrum of F264L is identical to that of the wild-type. Nonetheless, both Y249L and Y249L/F264L, whose CD spectra were much the same, had small reduced CD intensity in the region between 210 and 222 nm compared to the wild-type and F264L mutant.

### 5.3 Fluorescence emission spectra of the Cry4Ba and its mutants

To determine whether the leucine substitutions would cause any tertiary structural changes in these three mutants, the intrinsic tryptophan fluorescence spectroscopy was performed. It was found that the FPLC-purified trypsin-treated mutants, Y249L, F264L and Y249L/F264L yielded the same maximum fluorescence emission at 346 nm in comparison with that of the 65-kDa purified wild-type toxin (see **Figure 5.3**).

### 5.4 Membrane perturbing activity of Cry4Ba and its mutant toxins

The effect of the 65-kDa purified Cry4Ba and its mutant toxins on the integrity of membrane vesicles, it was investigated by using calcein release assays as described in **Method 3.2.18**. It is found that upon adding 3  $\mu\text{g}$  of the purified activated Cry4Ba toxin dissolved in carbonate buffer was able to fast induce the release of entrapped calcein from LUVs with approximately 50% release (see **Figure 5.4**). In contrast, the ability of the 65-kDa inactivated mutants, Y249L, F264L and Y249L/F264L exhibited less perturbing activity with approximately 29%, 25% and 9%, respectively.

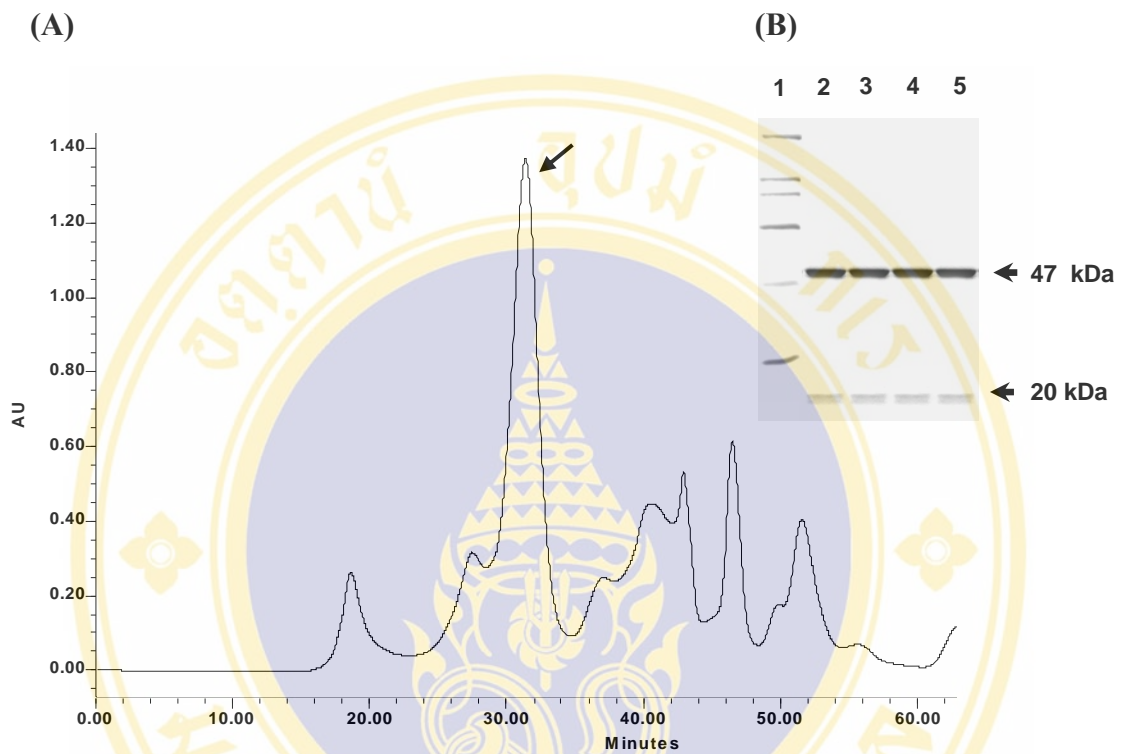


**Figure 5.1** Size-exclusion chromatogram and SDS-PAGE analysis of purified trypsin-treated Cry4Ba and its mutants

The figure shows (A) one of the FPLC chromatogram of the 65-kDa Cry4Ba and its derivative toxins passed through the Superdex 200 column. (B) 15% Coomassie blue-stained SDS-PAGE of Cry4Ba and its derivative toxins.

- Lane 1: Molecular mass protein standards
- Lane 2: Eluted fraction of the Cry4Ba wild-type toxin
- Lane 3: Eluted fraction of the Y249L toxin
- Lane 4: Eluted fraction of the F264L toxin
- Lane 5: Eluted fraction of the Y249L/F264L toxin

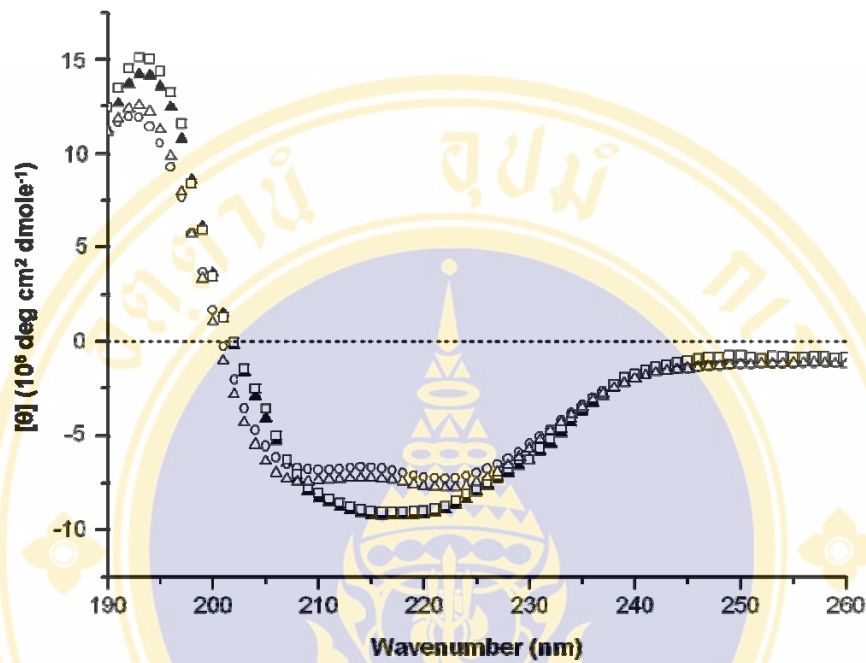


**Figure 5.2 CD spectra of the wild-type Cry4Ba and its mutant toxins**

The figure shows CD spectra of the 65-kDa purified Cry4Ba toxin ( $\blacktriangle$ ) in comparison with that of the mutant toxins, Y249L ( $\circ$ ), F264L ( $\square$ ) and Y249L/F264L ( $\triangle$ ), in 50 mM carbonate buffer, pH 10.0.

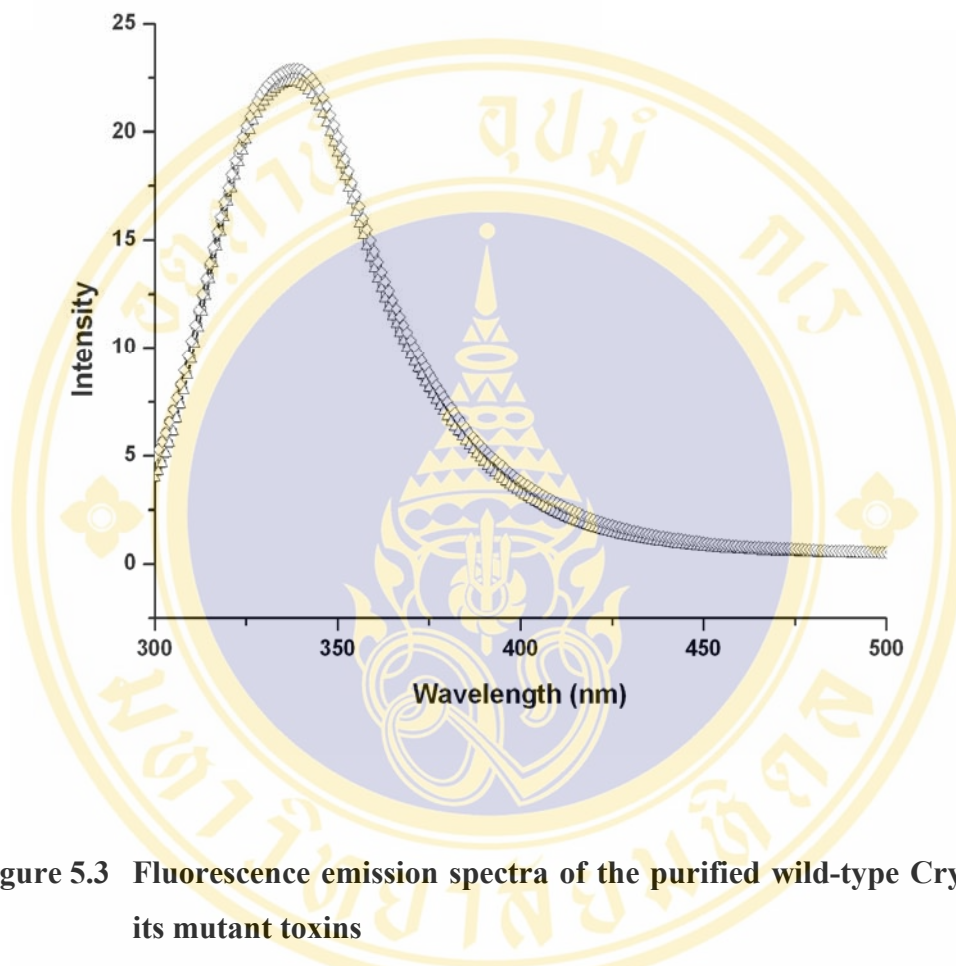


**Figure 5.3 Fluorescence emission spectra of the purified wild-type Cry4Ba and its mutant toxins**

The figure shows intrinsic fluorescence spectra displayed with 340 nm excitation at room temperature of the Cry4Ba toxin (□), Y249L (○), F264L (△) and Y249L/F264L (◇).

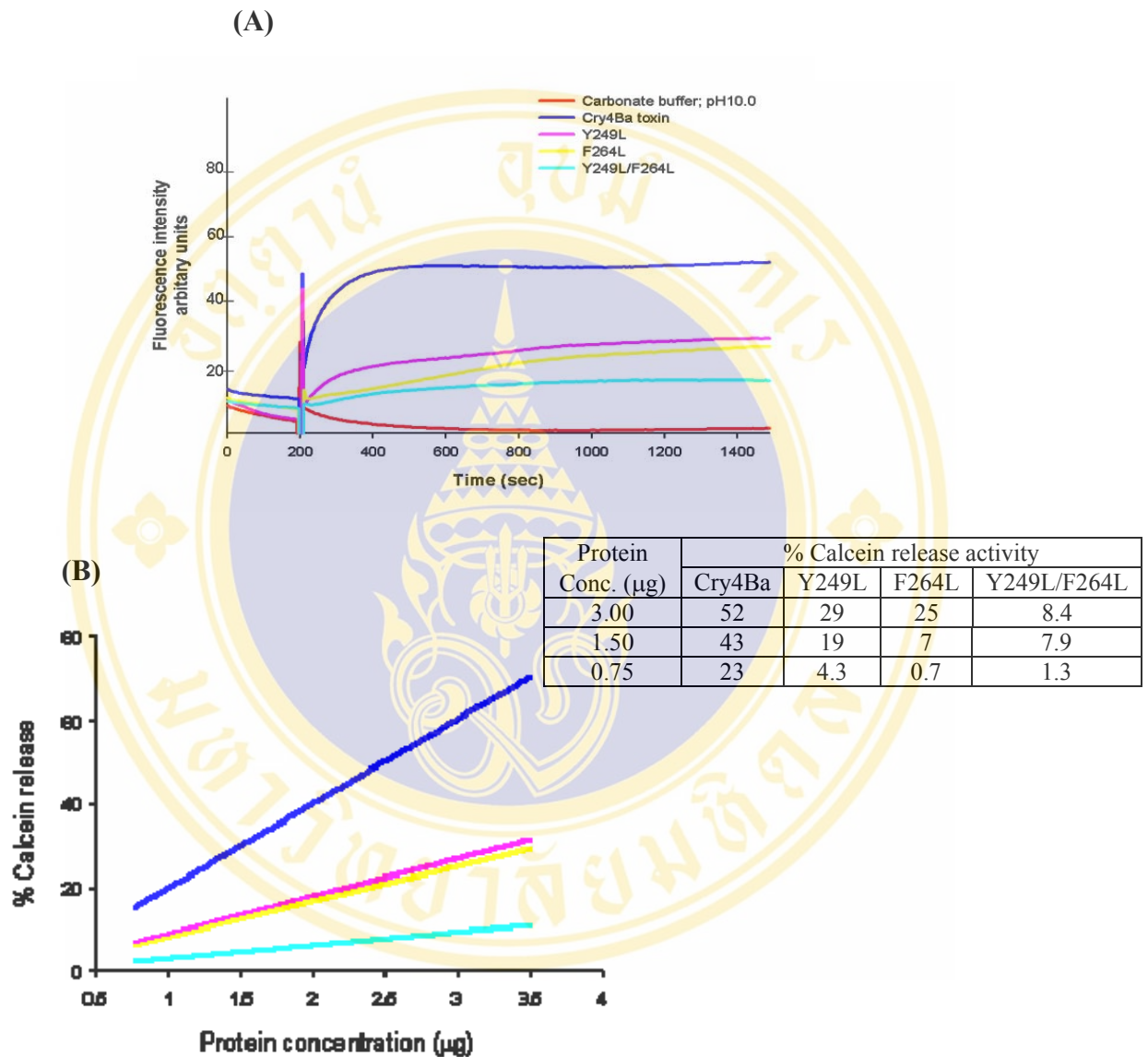


**Figure 5.4 Membrane perturbation activity of the Cry4Ba and its mutant toxins**

The figure shows (A) fluorescence intensity traces after adding the activated toxins into calcein entrapped LUVs. The curves were obtained at each 3µg 65-kDa Cry4Ba wild-types and its mutant toxins. (B) The relative release activity of each protein sample with different concentrations.

## 5.5 ATR-FTIR measurement of the helix 7 peptide

It is also interesting to investigate a possible involvement in toxicity of the two highly conserved aromatic residues, Tyr<sup>249</sup> and Phe<sup>264</sup> in  $\alpha 7$  within the Cry4Ba pore-forming domain, particularly in the steps of membrane-protein interactions. ATR-FTIR spectroscopy was employed to determine the secondary structure and orientation of secondary structural elements of a synthetic peptide corresponding to  $\alpha 7$  of Cry4Ba (see **Figure 5.5**) when incorporated into DMPC (1,2-dimyristoyl-sn-glycero-3-phosphocholine), DMPG (1,2-dimyristoyl-sn-glycero-3-phosphocholine) and DDPC (1,2-didecanoyl-sn-Glycero-3-phosphocholine). In addition, polarised ATR-FTIR measurements were carried out for the <sup>13</sup>C=O carbonyl vibration of a specifically labeled residue at Val<sup>18</sup> position so as to determine helix tilt and rotational orientation. The CN stretching vibration at Phe<sup>7</sup> position for reporting local environment of a particular amino acid in protein or local environmental changes upon binding was also characterised.

### 5.5.1 Quantification of secondary structure of the $\alpha 7$ peptide

At the peptide-to-lipid molar ratio 1:5 and 1:30, non-polarised spectra of the amide I region of helix 7 showed two major component bands at 1633 and 1654 cm<sup>-1</sup> that are assigned to  $\beta$ -sheet and  $\alpha$ -helical structures, respectively (see **Figure 5.6A**). However, it was found that the helix 7 peptide revealed a distinct  $\alpha$ -helical structure at the peptide-to-lipid molar ratio of 1:100. In similar experiments using negatively charged DMPG membranes, the main amide I maximum of helix 7 was observed to be centered at 1655 cm<sup>-1</sup> (see **Figure 5.6B**). **Figure 5.6C** shows the main amide I maximum centered at 1631 cm<sup>-1</sup> with small shoulders at 1654 cm<sup>-1</sup> after mixing the peptide with short-chain phospholipid membrane, DDPC. Like in DMPC membranes, the helix 7 peptide showed a distinct  $\alpha$ -helical structure at the peptide-to-lipid molar ratio of 1:100. The quantitative results of the amide I band decomposition are summarised in **Table 5.1**.

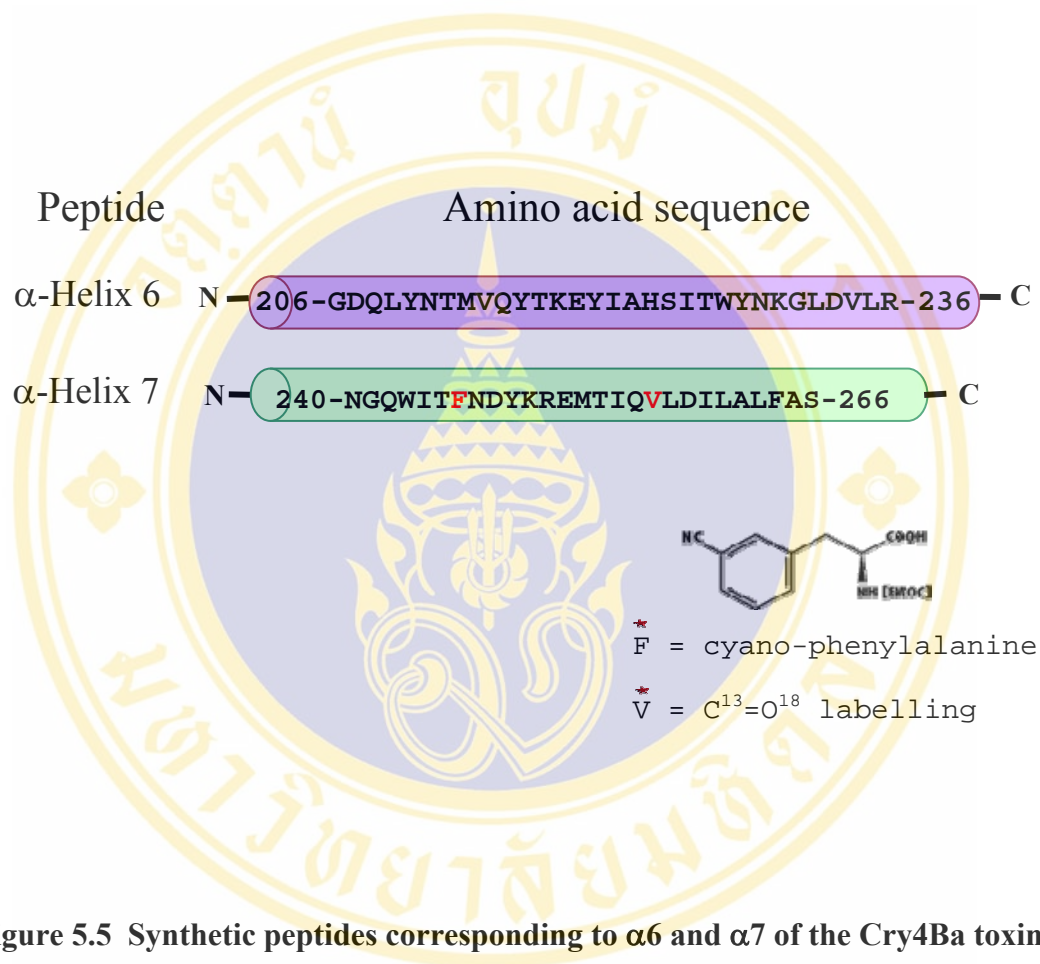


**Figure 5.5 Synthetic peptides corresponding to  $\alpha$ 6 and  $\alpha$ 7 of the Cry4Ba toxin**

The figure shows sequences and designations of peptides corresponding to helices 6 and 7. These sequences are derived from the crystal structures of Cry4Ba (21).

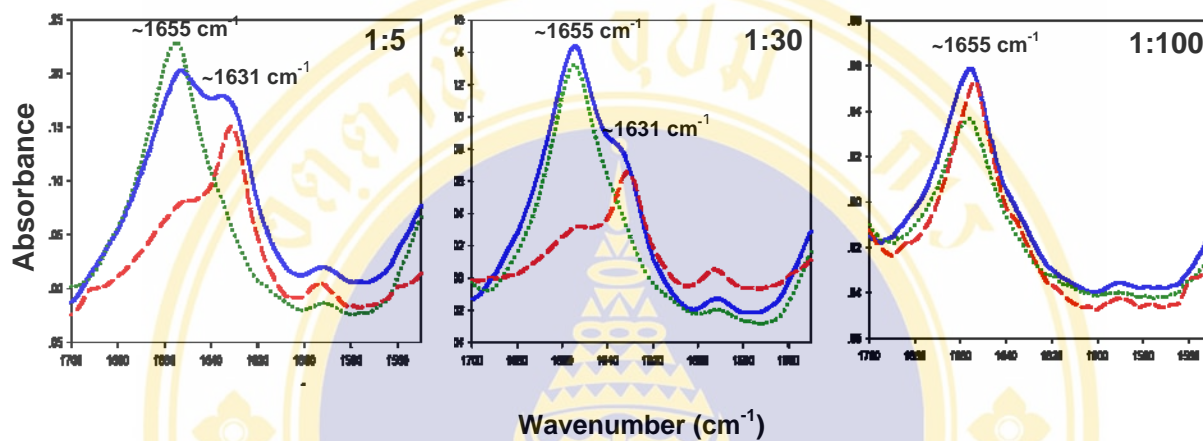


**Figure 5.6 Secondary structural contents of helix 7 in different lipid membranes**

The figure shows non-polarised spectra of the amide I band for helix 7 peptide incorporated in DMPC (—), DMPG (⋯) and DDPC (---) at peptide-to-lipid molar ratio of 1:5, 1:30 and 1:100.

**Table 5.1** Estimated percentage of secondary structural contents of helix 7 in DMPC, DMPG and DDPC with different peptide-to-lipid ratios

Sample (peptide-to-lipid)	Secondary structure (%)					
	DMPC		DMPG		DDPC	
	$\alpha$ -helix	$\beta$ -sheet	$\alpha$ -helix	$\beta$ -sheet	$\alpha$ -helix	$\beta$ -sheet
Helix 7 (1:5)	50	50	100	-	23	77
Helix 7 (1:30)	65	35	100	-	43	57
Helix 7 (1:100)	90	10	100	-	87	12

Standard deviation of each value is < 5%

### 5.5.2 Orientations of helix 7 incorporated into lipid membranes

After secondary structures of the helix 7 peptides incorporated into different lipid membranes were determined, further analysis was performed so as to quantify how many residues would be embedded in the membrane by using amide-H/D exchange experiment. It was followed by monitoring the amide II absorption peak at  $1544\text{ cm}^{-1}$  and amide A at about  $3300\text{ cm}^{-1}$  as a function of the time when exposure to  $\text{D}_2\text{O}$ -saturated  $\text{N}_2$  until exchange was complete.

As shown in **Figure 5.7**, it was found that the amide II of helix 7 peptides in the DMPC membrane are still present after 1-h exchange in  $\text{D}_2\text{O}$ . Since the decrease of the amide II region is proportional to the number of hydrogen atom that have been exchanged by deuterium (red arrow in **Figure 5.7**) indicating that part of the peptide samples are protected from exchange and embedded in the lipid membrane at all peptide-to-lipid molar ratios. Moreover, the measurements by examination of the ratio between non-polarised amide II and amide I before and after  $\text{D}_2\text{O}$  exchange revealed that approximately 90% (24 amino acids) of the 27-residue helix 7 peptide, which exists in  $\beta$ -form was inserted in DMPC. In contrast,  $\alpha$ -helical form showed an approximately 40% insert (11 amino acids) in the hydrophobic region of the lipid membrane. The DMPC lipid-induced  $\alpha$ -structure was more inserted into the membrane at the lipid-to-protein ratio of 1:100.

To determine the orientation of the helix 7 peptide with respect to the lipid membrane, the phospholipid membrane should be well ordered by looking at the dichroic ratio of the methylene asymmetric and symmetric stretching modes at  $2924$  and  $2852\text{ cm}^{-1}$ , respectively. The dichroic ratio at  $2850\text{ cm}^{-1}$  from the DMPC lipid, which was incorporated with peptides, was typically 1.1. For helix 7 peptides reconstituted in DMPC at ratios of 1:5, 1:30 and 1:100, the dichroic ratios obtained under different conditions used and the helix tilts showed in **Table 5.2**. For the  $\beta$ -sheet form of the 27-residue helix 7 peptide, when bulk water was removed, the amide I band dichroism (1.28 and 1.47 at the lipid-to-peptide ratios of 1:5 and 1:30, respectively) indicates that the peptide is inserted into the DMPC membrane normal. Interestingly, after hydration in  $\text{D}_2\text{O}$ , the dichroism of the amide A (1.76 and 1.56 at the ratios of 1:5 and 1:30, respectively, see **Table 5.2**) is more reliable which gives an

average helix tilt of  $43^{\circ} \pm 5.0$ . For the  $\alpha$ -helical form of helix 7, the amide I band dichroism (see **Table 5.2**) shows that the peptide is localised at the DMPC membrane surface. On the other hand, all predominant  $\alpha$ -helical structures were observed and to be inserted into the DMPC at the lipid-to-protein ratio of 1:100 by a tilt angle of  $41^{\circ}$ . For the 31-residue helix 6 peptide that is used as a control, the dichroic ratio of amide I and amide A of both before and after D<sub>2</sub>O hydration (see **Table 5.2**) indicated that this peptide that exists only in the form of  $\alpha$ -helical conformation is placed on the surface and approximately 54% (17 amino acids) is embedded in the lipid membrane (see **Figure 5.10**).

Like in the DMPC conditions, the amide II has not shifted after hydrated with D<sub>2</sub>O (**Figure 5.8**). Moreover, amide A of helix 7 peptides in the DMPG membrane are still present after 1-h exchange in D<sub>2</sub>O, indicating that the peptide samples are protected from exchange and embedded in the lipid membrane at all peptide-to-lipid molar ratios. It was found that 72% (19 amino acids) of the  $\alpha$ -helical peptide, as inserted in DMPG systems. To determine the orientation of the helix 7 peptide with respect to the lipid membrane, the dichroic ratio at  $2850\text{ cm}^{-1}$  from the DMPG lipid incorporated with peptides was typically 1.2. For helix 7 peptides reconstituted in DMPG membranes at peptide-to-lipid ratios of 1:5, 1:30 and 1:100, the helical structure as observed to be inserted in negatively charged DMPG at all peptide-to-lipid ratios. The dichroic ratios obtained under different conditions used and the helix tilts are shown in **Table 5.2**.

After D<sub>2</sub>O exposure, 61%, 100% and 48% of the helix 7 peptide was protected from exchange at peptide-to-lipid ratio of 1:5, 1:30 and 1:100, respectively. It was confirmed by presence of the amide II bands (**Figure 5.9**). When the short-chain phospholipid (DDPC) was employed, the bandshape of amide I obtained was similar to that was observed in DMPC system. Although it displayed the  $\beta$ -sheet more than  $\alpha$ -helix of the amide I contour for peptide-to-lipid ratios of 1:5 and 1:30, the amide I band dichroism of helix 7 in DDPC indicated that  $\alpha$ -helical conformation are absolutely located at the membrane surface at peptide-to-lipid ratio of 1:30. This is consistent with 48% insertion of this peptide at peptide-to-lipid ratio of 1:100. In addition, the presence of DDPC lipid also exhibited  $\beta$ -structure penetrating into lipid

membrane, giving a helix tilt of  $33^\circ \pm 1$  at protein-to-lipid ratio of 1:5 and 1:30, respectively (see **Table 5.2**).

### 5.5.3 Secondary structures and orientation determination of helix 7 peptide using $C^{13}=O^{18}$ probe

As mentioned previously, the helix 7 peptide was labelled with  $C^{13}=O^{18}$  at Val<sup>18</sup> to relay site-specific orientational information. The peptide which contains a  $C^{13}=O^{18}$  label has an additional peak that is present next the amide I band (102). Here, the frequency shift obtained for the  $C^{13}=O^{18}$  was at  $\sim 1591\text{ cm}^{-1}$  (**Figure 5.11**) for all different conditions. The isotope edited shift of  $-63\text{ cm}^{-1}$  was observed from the original frequency at  $1654\text{ cm}^{-1}$ , corresponding to an  $\alpha$ -helical structure and that of  $-44\text{ cm}^{-1}$  was from the original frequency at  $1632\text{ cm}^{-1}$ , corresponding to a  $\beta$ -sheet structure. The dichroic ratio obtained for the  $C^{13}=O^{18}$  isotope was significantly larger than that obtained for the main amide I peak (see **Table 5.2**). The orientational information of helix 7 peptide in lipid environment from isotopic probe revealed in the same direction as that obtained from the natural amide I band.

### 5.5.4 Localisation of Tyr<sup>249</sup> and Phe<sup>264</sup> in helix 7 of the Cry4Ba toxin

To further determine the spatial orientations of the  $\alpha$ -helical peptide that is localised on the membrane, CN stretching vibration was measured for the helix 7 peptide labelled with cyano group at Phe<sup>7</sup> (Phe<sub>CN</sub>) (see **Figure 5.5**). The result revealed that the CN stretching vibration is centred at  $\sim 2228\text{ cm}^{-1}$  (**Figure 5.12**), indicating that the Phe<sub>CN</sub> side chain in the peptide is buried in the hydrophobic region of the membrane.

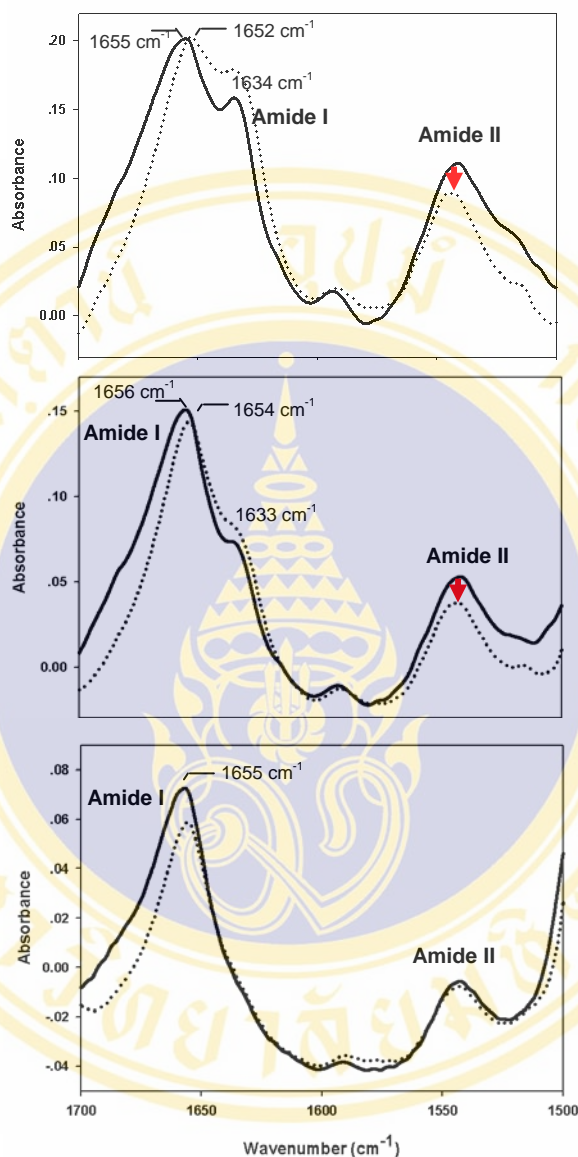


**Figure 5.7** ATR-FTIR spectra of helix 7 peptide in DMPC membranes

The figure shows non-polarised infrared-attenuated total reflection spectra of amide I and II when helix 7 was added to DMPC membranes. Top panel: amide I and II before (—) and after (·····) hydration with D<sub>2</sub>O at peptide-to-lipid molar ratio of 1:5. Middle panel: at peptide-to-lipid molar ratio of 1:30. Bottom panel: at peptide-to-lipid molar ratio of 1:100. The red arrow indicates the decrease of amide II region after hydration with D<sub>2</sub>O.

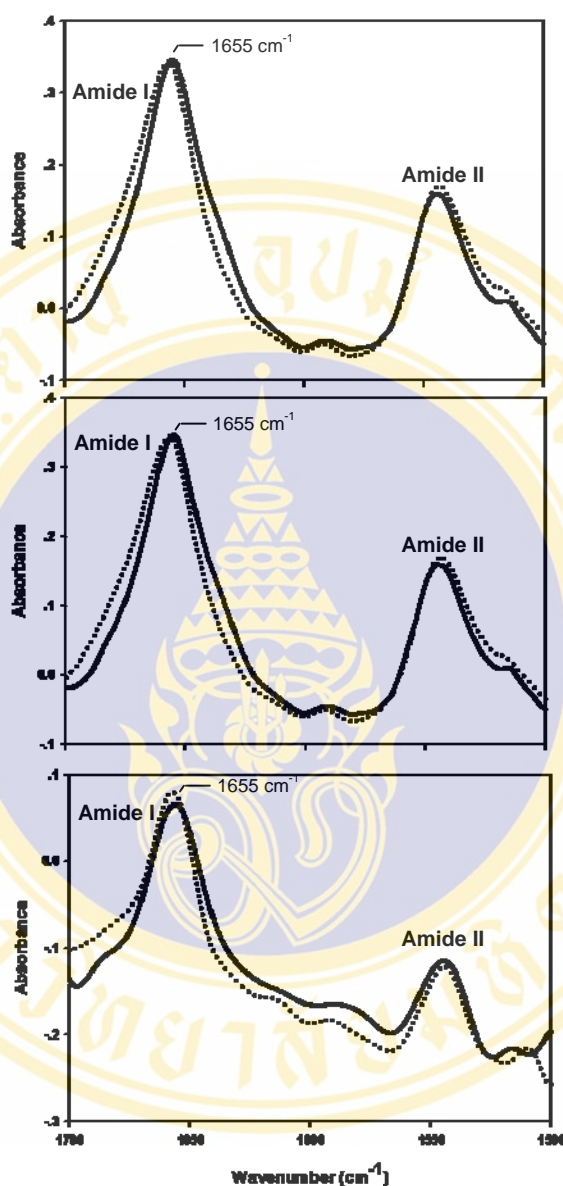


**Figure 5.8** ATR-FTIR spectra of helix 7 peptide in DMPG membranes

The figure shows non-polarised infrared-attenuated total reflection spectra of amide I and II when helix 7 was added to DMPG membranes. Top panel: amide I and II before (—) and after (.....) hydration with D<sub>2</sub>O at peptide-to-lipid molar ratio of 1:5. Middle panel: at peptide-to-lipid molar ratio of 1:30. Bottom panel: at peptide-to-lipid molar ratio of 1:100. The red arrow indicates the decrease of amide II region after hydration with D<sub>2</sub>O.

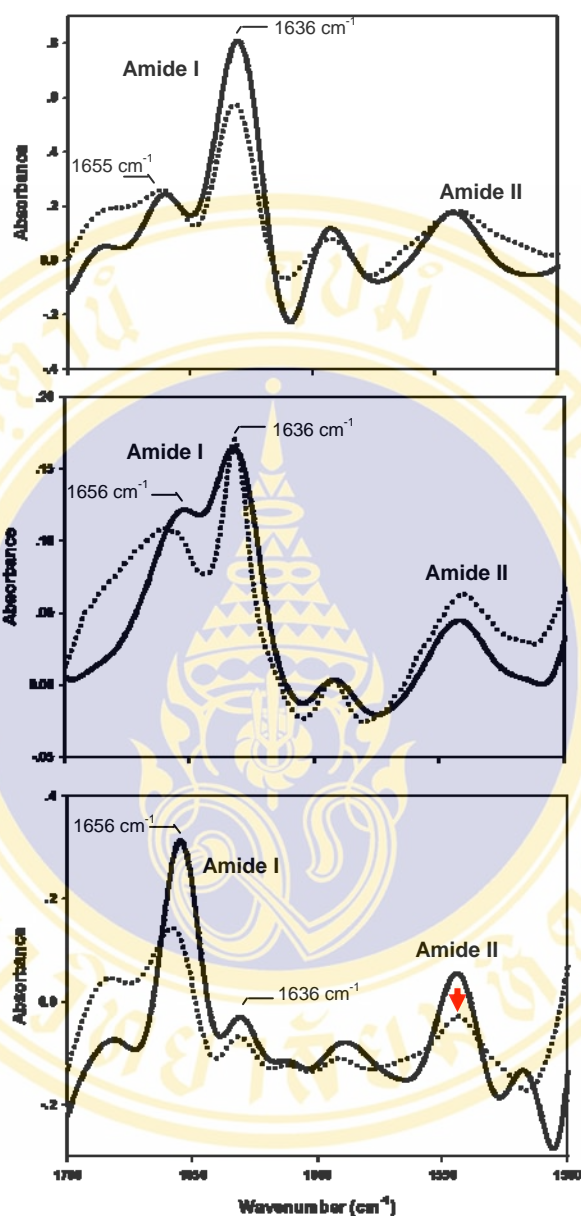


**Figure 5.9** ATR-FTIR spectra of helix 7 peptide in DDPC membranes

The figure shows non-polarised infrared-attenuated total reflection spectra of amide I and II when helix 7 was added to DDPC membranes. Top panel: amide I and II before (—) and after (·····) hydration with D<sub>2</sub>O at peptide-to-lipid molar ratio of 1:5. Middle panel: at peptide-to-lipid molar ratio of 1:30. Bottom panel: at peptide-to-lipid molar ratio of 1:100. The red arrow indicates the decrease of amide II region after hydration with D<sub>2</sub>O.

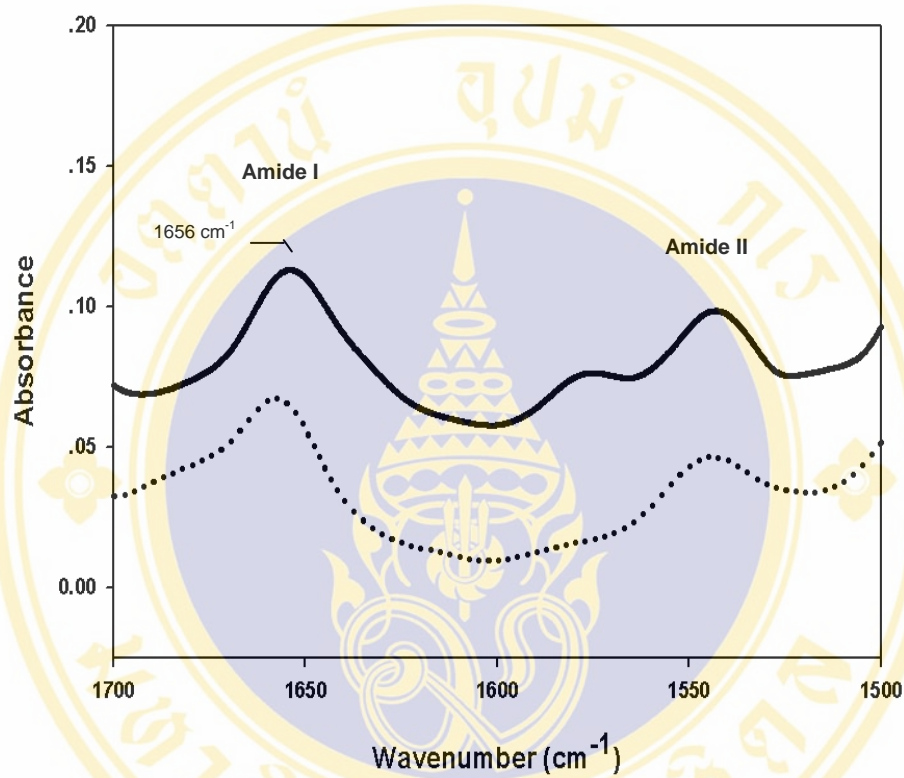


**Figure 5.10** ATR-FTIR spectra of helix 6 peptide in DMPC membranes

The figure shows non-polarised infrared-attenuated total reflection spectra of helix 6 with DMPC membranes. Amide I and II before (—) and after (·····) hydration with D<sub>2</sub>O at peptide-to-lipid molar ratio of 1:30.

**Table 5.2 Orientation analysis of helix 7 peptide of Cry4Ba in DMPC, DMPG and DDPC with different peptide-to-lipid ratios**

Lipid system	Bulk water removed (H <sub>2</sub> O)			Hydrated membrane (D <sub>2</sub> O)					
	R <sub>AI</sub>		R <sub>AA</sub>	R <sub>AI</sub>		R <sub>AA</sub>	R <sub>iso</sub>	β	
	R <sub>α</sub>	R <sub>β</sub>		R <sub>α</sub>	R <sub>β</sub>			α	β <sub>hairpin</sub>
DMPC (peptide-to-lipid)									
1:5	1.86	1.28	1.72	1.82	1.54	1.76	1.87	60°	43°
1:30	1.51	1.47	1.80	1.82	1.78	1.56	1.85	60°	37°
1:100	2.41	-	1.95	2.78	-	2.38	2.43	-	41°
DMPG (peptide-to-lipid)									
1:5	2.26	-	2.45	2.40	-	3.08	2.78	51°	-
1:30	3.71	-	2.00	2.58	-	2.00	3.19	43°	-
1:100	2.78	-	2.86	2.66	-	2.86	3.13	42°	-
DDPC (peptide-to-lipid)									
1:5	1.32	1.18	1.35	1.83	1.26	1.19	1.11	59°	33°
1:30	1.73	1.02	1.46	1.13	1.18	1.62	1.18	64°	32°
1:100	1.00	1.32	1.82	1.89	1.92	1.96	1.61	57°	54°
Helix 6	1.66	-	1.61	1.54	-	1.85	-	77°	-

The table shows measured dichroic ratios of amide I (R<sub>AI</sub>), amide A (R<sub>AA</sub>) and isotopic labelling C<sup>13</sup>=O<sup>18</sup> (R<sub>iso</sub>). R is the dichroic ratio from helix formation (R<sub>α</sub>) and β-sheet formation (R<sub>β</sub>). β represents tilt angle of either α-helix or β-structure peptides in DMPC, DDPC and DMPG with different peptide-to-lipid ratios.

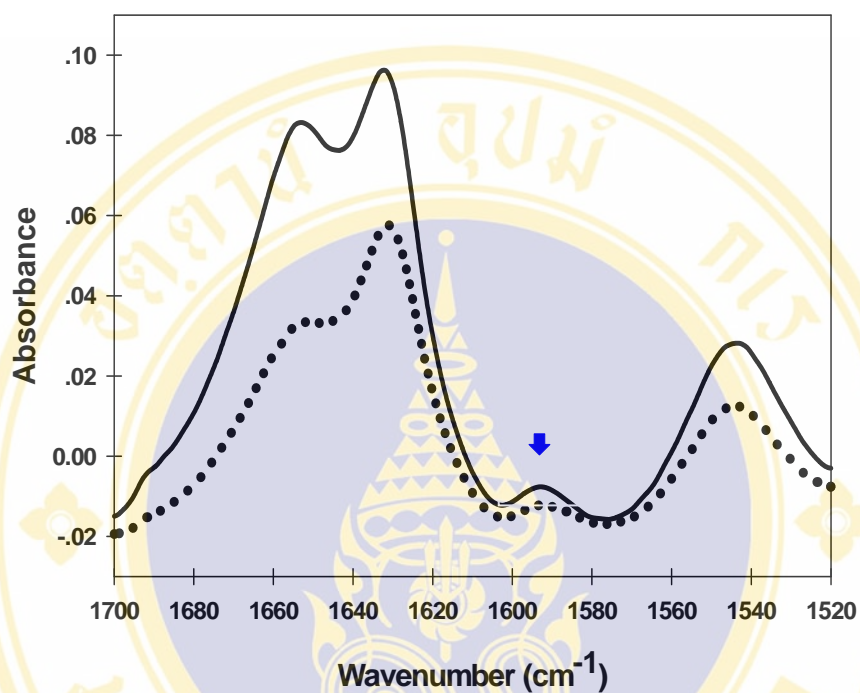


**Figure 5.11** Polarised ATR-FTIR spectra of the isotope probe  $^{13}\text{C}=\text{}^{18}\text{O}$  at Val<sup>18</sup>

The figure shows infrared spectra of helix 7 peptide in DMPC labelled with  $\text{C}^{13}=\text{O}^{18}$  at positions Val<sup>18</sup>, collected with parallel ( $\parallel$ , solid line) or perpendicular ( $\perp$ , dotted line) polarisation light at ca.  $1591\text{ cm}^{-1}$ . The blue arrow indicates the position of the isotope edited peak.

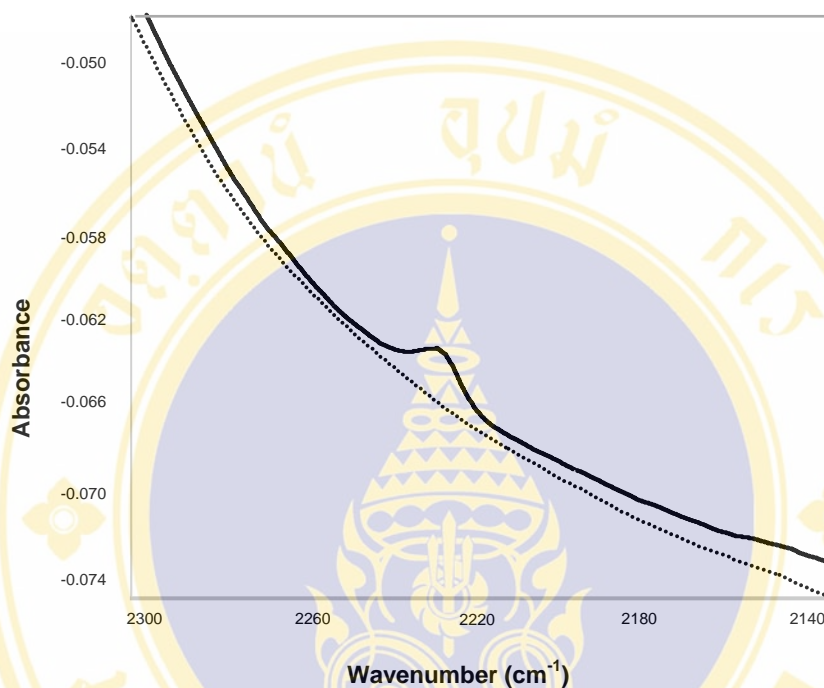


**Figure 5.12** Polarised ATR-FTIR spectra of the nitrile-derivatised probe at Phe<sup>7</sup> (Phe<sub>CN</sub>)

The figure shows FTIR spectra of Phe<sub>CN</sub> (CN stretching region) in lipid environment as indicated with solid line (—) and unlabelling spectra (.....) at a position of ca. 2228 cm<sup>-1</sup>.

## 5.6 Peptide-induced membrane perturbation

Further characterisation of the effect on the integrity of membrane vesicles, entrapped dye-release experiments were used to access peptide-induced perturbation of liposomes. LUVs of PC/PE/Ch compositions were created with self-quenched fluorescence dye calcein entrapped in their interior cavity. Membrane perturbation was monitored by the increase in fluorescence after adding peptide sample dissolved in DMSO. It was found that the membrane perturbing ability of both helix 7 and helix 6 peptides (2.3  $\mu\text{M}$ ) was relatively the same, with maximally release of  $\sim 15\%$  (see **Figure 5.13**).

## 5.7 Structure and dynamics of the helix 7 peptide in DMPC bilayers

Synthetic phospholipids, DMPC, membranes were chosen as a model since they are more relevant to the phospholipids found in the insect cell membranes (136,137). MD simulations in the DMPC bilayer system of the helix 7 peptide were carried out based upon the ATR-FTIR data. Two possible models for the helix 7 peptide were generated (see **Figure 5.14**). In the simulation systems, an  $\alpha$ -helical model was placed at the membrane water-interface region with an aromatic side chain of Phe<sup>7</sup> pointing towards the membrane while a  $\beta$ -structure model was inserted transversely into a bilayer membrane. An overall measurement of two possible models was observed by the time-dependent  $C_{\alpha}$  atoms root mean square deviations (RMSDs) from the starting structure. For  $\alpha$ -helical model/DMPC surface, the RMSD was found to be  $\sim 0.18$  nm over the first  $\sim 4.75$  ns, it then fluctuated between  $\sim 0.18$  and 0.3 nm for the remaining 10-ns simulation (**Figure 5.15A**). The diagrams of secondary structure versus time for the conformational dynamics of  $\alpha$ -helical models revealed that the  $\alpha$ -helical conformation was largely preserved throughout the simulation time (**Figure 5.15B**). Moreover, the helix orientation was nearly parallel to the membrane surface, with an average angle of  $\sim 90^{\circ}$ .

The  $C_{\alpha}$  RMSDs of  $\beta$ -structure model/DMPC was found to be largely fluctuated around  $\sim 0.33$  nm after 2 ns (see **Figure 5.16A**). However, beta-hairpin structure was retained in residues 1-10 and 20-27 like the starting structure throughout 10 ns (**Figure 5.16B**). In addition, it can be seen that an average orientation angle of

$\beta$ -sheet structure model with the plane of the bilayer is at  $\sim 39^\circ$ . For helix 6 peptide, the peptide formed a stable helix at the DMPC bilayer interface throughout 8 ns, with rmsd values of ca. 0.3 nm. (**Figure 5.17-5.18**).



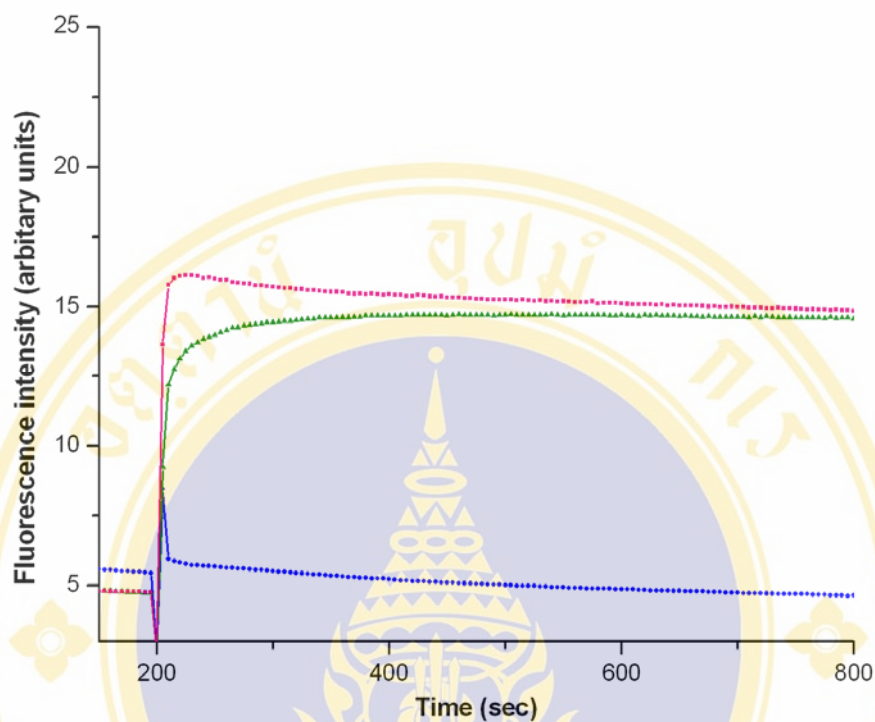


**Figure 5.13 Effects of Cry4Ba-helical peptides on the entrapped calcein released from LUVs**

The figure shows the fluorescence intensity of the entrapped calcein upon release from LUVs, which were continuously monitored as a function of time after incubation with the helix peptides (7.5  $\mu\text{g}/\text{ml}$ ). 4  $\mu\text{l}$  of DMSO was used as a negative control. The helix 7 peptide of Cry4Ba is indicated by  $\blacksquare$ , while the helix 6 peptide and DMSO are indicated by  $\blacktriangle$  and  $\bullet$ , respectively.

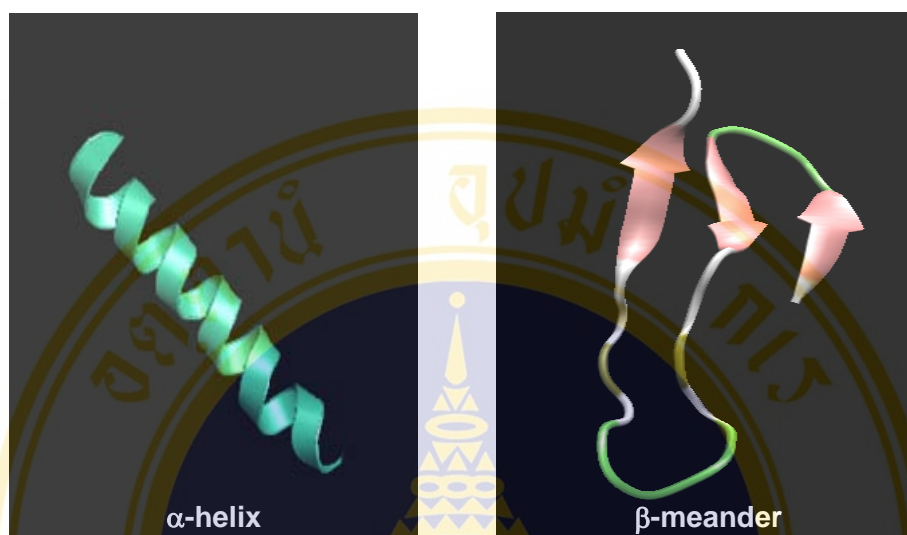
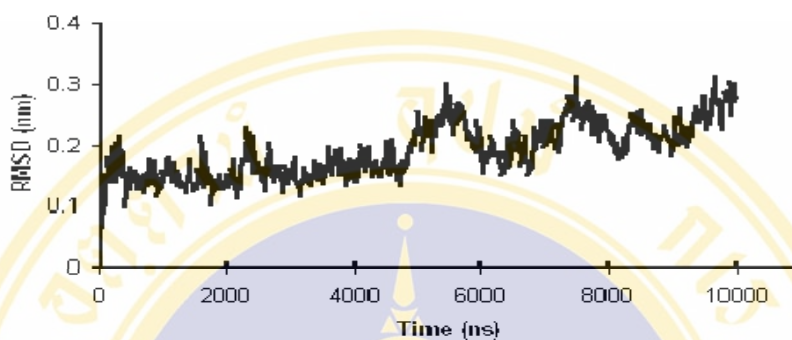


**Figure 5.14 Schematic ribbon representations of  $\alpha$ -helical and  $\beta$ -meander conformations of the helix 7 peptide**

The figure shows schematic ribbon representations of  $\alpha$ -helical and  $\beta$ -meander conformations the helix 7 peptide used in MD simulations. Both conformations were generated by Xplor and Whatif program.

(A)



(B)

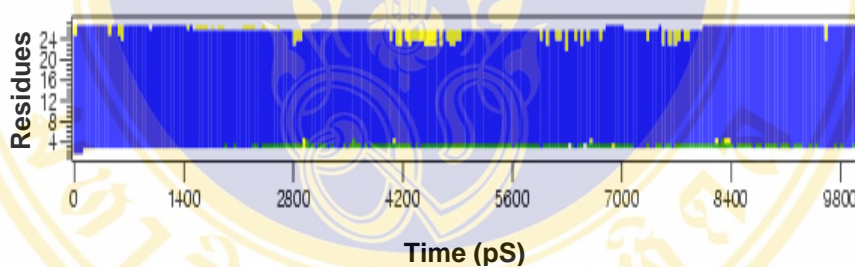


**Figure 5.15 Trajectory analysis of  $\alpha$ -helical structure of the helix 7 peptide in DMPC bilayers**

The figure shows (A) RMSDs versus time for the  $C_{\alpha}$  atoms in alpha-helical conformation of the helix 7 peptide of Cry4Ba for 10 ns in DMPC bilayers. (B) observed secondary structures as a function of simulation time, analysed by using DSSP, showing  $\alpha$ -helix at the membrane water-interface region for 10 ns.

Grayscale: blue,  $\alpha$ -helix; yellow, turn; red,  $\beta$ -sheet; green, bending, as indicated at the bottom of the diagram

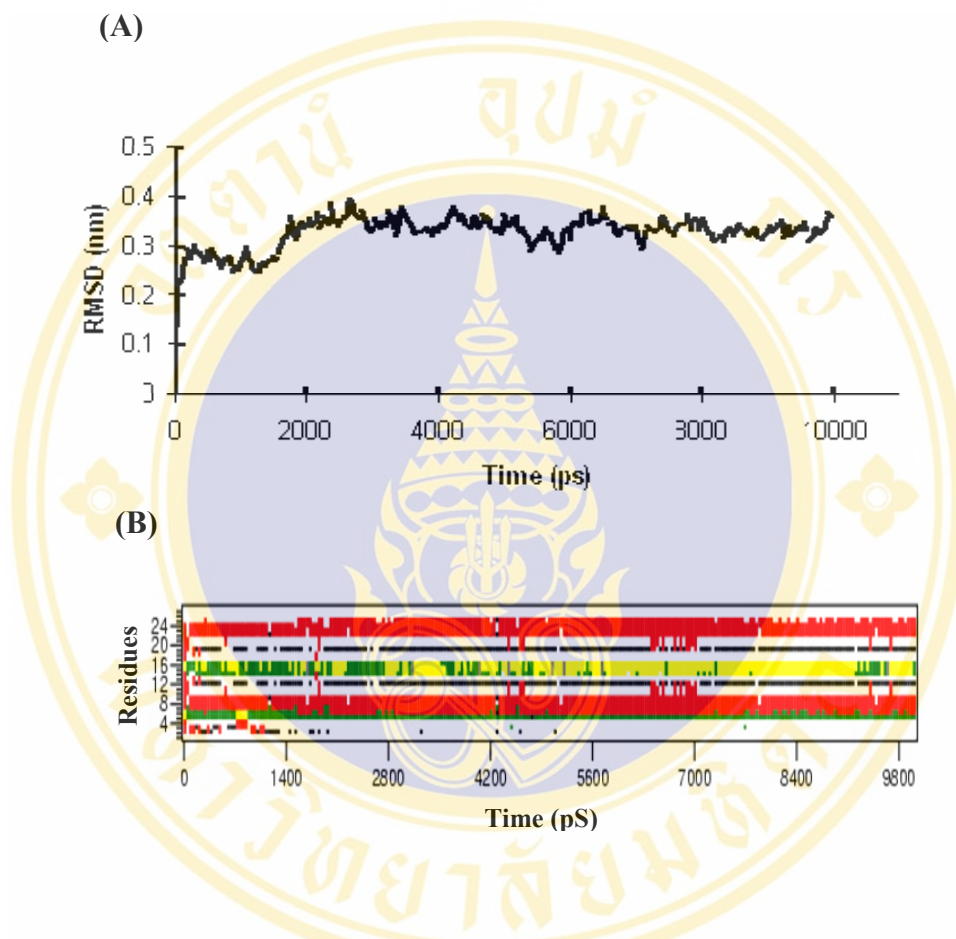


**Figure 5.16 Trajectory analysis of  $\beta$ -hairpin structure of the helix 7 peptide in DMPC bilayers**

The figure shows (A) RMSDs versus time for the  $C_{\alpha}$  atoms in  $\beta$ -hairpin conformation of the helix 7 peptide of Cry4Ba for 10 ns in DMPC bilayers. (B) observed secondary structures as a function of simulation time, analysed by using DSSP, showing  $\beta$ -form when inserted transversely into DMPC bilayers for 10 ns. Grayscale: blue,  $\alpha$ -helix; yellow, turn; red,  $\beta$ -sheet; green, bending, as indicated at the bottom of the diagram.

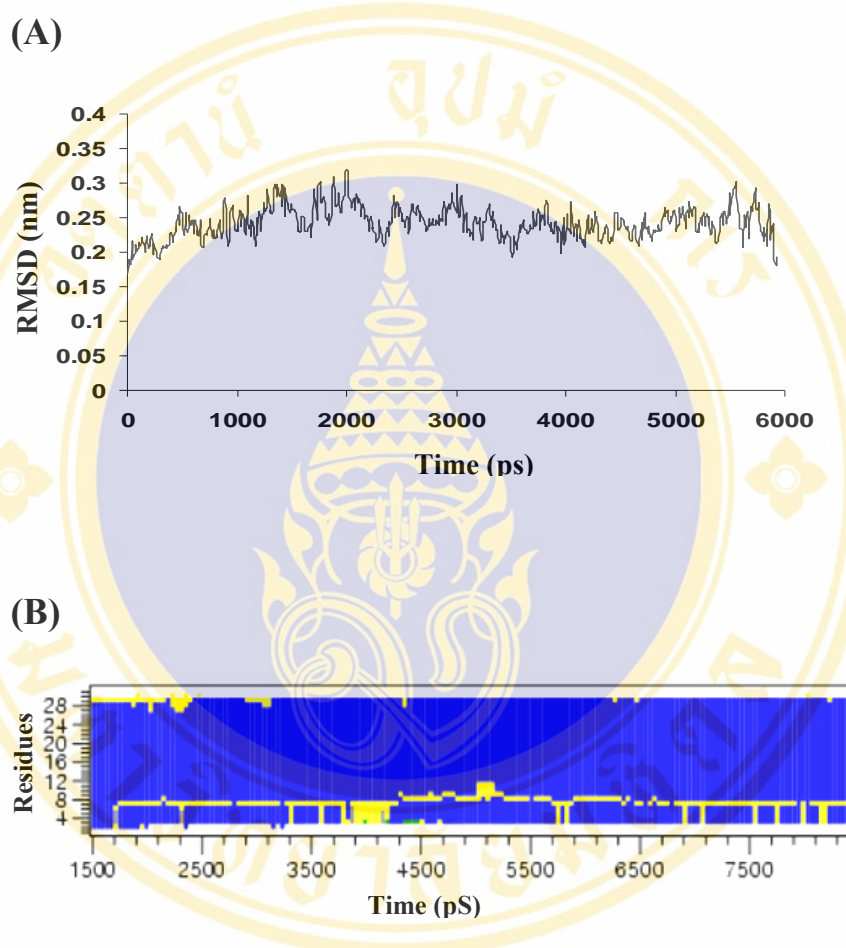


**Figure 5.17 Trajectory analysis of  $\alpha$ -helical structure of the helix 6 peptide in DMPC bilayers**

The figure shows (A) RMSDs versus time for the  $C_{\alpha}$  atoms in  $\alpha$ -helical conformation of the helix 6 peptide of Cry4Ba for 6 ns in DMPC bilayers. (B) observed secondary structures as a function of simulation time, analysed by using DSSP, showing  $\alpha$ -form at the membrane water-interface region for 8 ns.

Grayscale: blue,  $\alpha$ -helix; yellow, turn; red,  $\beta$ -sheet; green, bending, as indicated at the bottom of the diagram.

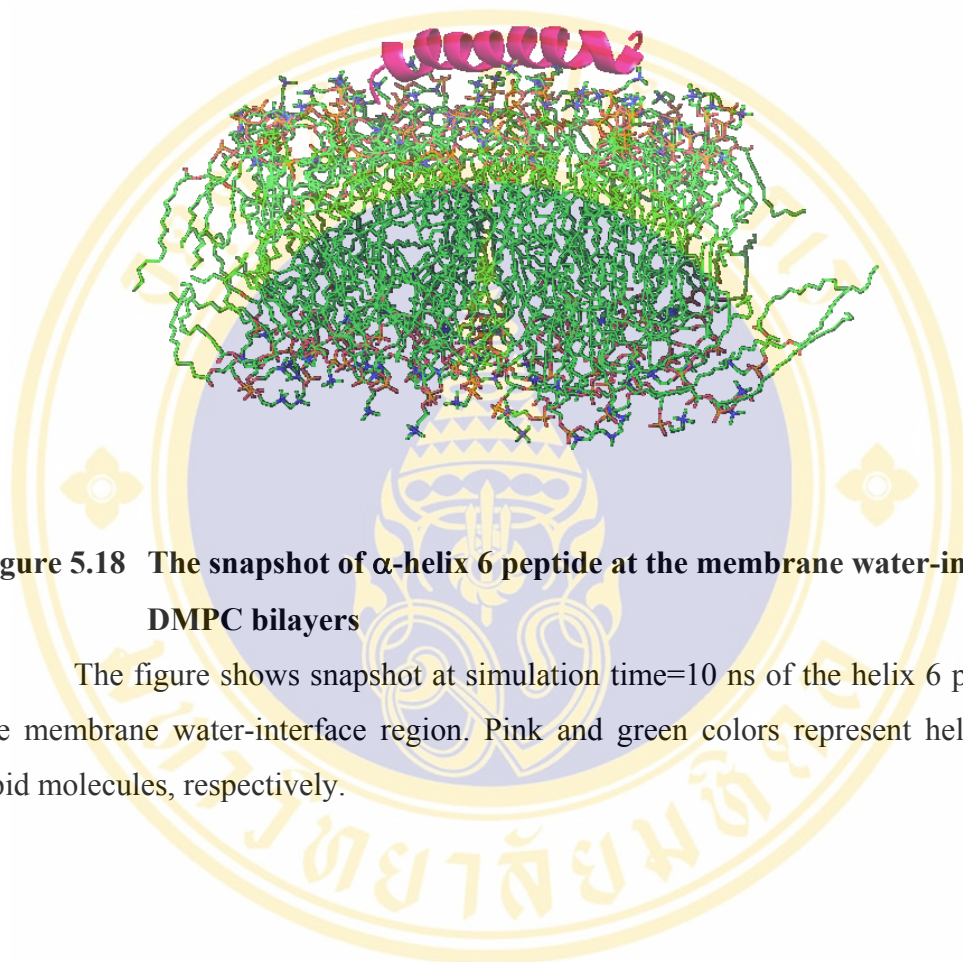


**Figure 5.18 The snapshot of  $\alpha$ -helix 6 peptide at the membrane water-interface DMPC bilayers**

The figure shows snapshot at simulation time=10 ns of the helix 6 peptide at the membrane water-interface region. Pink and green colors represent helix 6 and lipid molecules, respectively.

## CHAPTER VI

### DISCUSSIONS

Thus far, the umbrella model that has been strengthened with several studies (79,84,91,92,132) seems to be the best description for the membrane-associated state of the *Bt* Cry  $\delta$ -endotoxins. This model suggested that  $\alpha 7$  may serve as a binding sensor that could initiate the binding of the pore-forming domain to the lipid membrane, facilitating the membrane insertion of the  $\alpha 4$ - $\alpha 5$  hairpin (78). Moreover, as was shown by numerous studies, the binding of membrane-inserting proteins to the lipid membrane surface *via* an aromatic cluster is a prerequisite for their membrane insertion and pore formation (129,130,131). In addition, studies on a variety of membrane proteins indicated that the preference location of aromatic residues was observed to be at or near the membrane-water interface (133,134). In this study, functional significance in toxicity mechanism of Trp<sup>243</sup>, Tyr<sup>249</sup> and Phe<sup>264</sup>, which are highly conserved within helix 7 of the Cry4Ba toxin was characterised.

#### 6.1 Solubilisation and proteolytic processing of the Cry4Ba mutants

When each Cry4Ba mutant toxin was expressed in *E. coli* upon IPTG induction, all were produced as inclusion bodies, and the expression level of the 130-kDa mutant protoxins was approximately the same as that of the wild-type toxin (see **Figures 4.7, 4.32-4.34**). However, although these mutations did not result in low levels of protein expression, the possibility cannot be excluded whether the mutations would affect the folding of the mutant molecules, as protein misfolding can lead to the formation of an insoluble inclusion. After determining the percentage of toxin solubility in carbonate buffer, pH 10.0, the amounts of the 130-kDa soluble proteins in the supernatant were compared with those of the total protein inclusions that were initially used. All the toxin inclusions of the larvicidal-active mutants that were substituted with an aromatic residue (W243F, Y249F, Y249W, F264Y and F264W) were found to be soluble in the carbonate buffer, giving at least 70-80% solubility which is comparable to that of the wild-type and the F246A larvicidal-active mutant

under similar conditions. In addition, toxin inclusions of the W243K, W243L, Y249L, F264L and Y249L/F264L mutants were also observed to be relatively soluble in this buffer (approximately 60% solubility), although they all with exception for the W243L mutant showed drastically reduced larvicidal activity.

On the other hand, a complete loss of the inclusion solubility was found for all the remaining mutants (W243A, Y249A, Y249E, Y249R, Y249H, F264A, F264E, F264R, F264H and F264A/Y249A), which all exhibited a severe loss in toxicity. This indicate that specific substitutions, particularly with alanine or polar non-charged or charged residues at the two critical conserved aromatic residues (Tyr<sup>249</sup> and Phe<sup>264</sup>) in  $\alpha 7$  could disturb the structural characteristics of the Cry4Ba toxin that would result in improper folding of the mutant proteins, leading to the formation of an insoluble aggregate *in vivo*. In this context, the packing interactions of both Tyr<sup>249</sup> and Phe<sup>264</sup> with their neighbouring residues were therefore analysed in comparison with that of mutated residues. As illustrated in **Figure 6.1**, both critical aromatic residues are located inside packing areas made up of several hydrophobic residues within 4 Å. The packing interactions of the substituted Leu at each critical position showed much the same appearance as that observed in the wild-type and its conservative mutants (Y249F, Y249W, F264Y and F264W). However, there were diminished contacts or cavities (see **Figure 6.1, arrowed**) introduced inside each packing cluster of the other mutant proteins when substituted with Ala, Arg, His or Glu. These are due to large conformational rearrangements of certain residues to be away from the packing interactions (see **Figure 6.1, encircled**). Hence, a disruption of this hydrophobic packing would result in serious structural consequences, and thus prevent the correct folding of the molecule, affecting the toxin-inclusion formation as shown by a loss in protein solubility.

All the 130-kDa soluble toxins were further examined for trypsin digestion susceptibility of the mutant protoxins, which could be solubilised in the carbonate buffer. They were found to produce two major trypsin-resistant fragments of ca. 47 and 20 kDa that are identical to the products obtained with the wild-type protoxin (**Figure 4.9 and 4.38**), indicating that all these mutants were produced as structurally stable protoxins and that the mutations had no apparent effect on proteolytic processing of the solubilised mutant toxins. Therefore, the reduced larvicidal-activity

observed in particular for the Y249L, F264L and Y249L/F264L mutants is not caused by incomplete solubilisation or proteolytic activation.

## 6.2 Functional characterisation of the conserved aromaticity in Cry4Ba-helix 7

When the purified 65-kDa mutant toxins, Y249L, F264L and Y249L/F264L were examined for their secondary structural elements by far-UV CD spectroscopy, all the CD profiles are basically similar (see **Figure 5.2**). Particularly, the spectrum of F264L is identical to that of the wild-type, confirming that no dramatic structural changes had occurred as a result of these three mutations. Nonetheless, both Y249L and Y249L/F264L, whose CD spectra were much the same, had small reduced CD intensity in the region between 210 and 222 nm compared to the wild-type and F264L mutant, suggesting that there is a slight rearrangement in protein conformation of these two mutants. However, trypsin digestion assays as demonstrated earlier (see **Figure 4.38**) revealed that such little conformational changes did not cause misfolding of the Y249L and Y249L/F264L mutant proteins. In addition, intrinsic fluorescence spectroscopy indicated that these three mutants and wild-type Cry4Ba toxins displayed the same overall tertiary structure. Therefore, the loss of toxicity of Y249L, F264L and Y249L/F264L mutants did not cause by misfolding of the protein after substitution.

As illustrated in **Figure 6.2**, both Tyr<sup>249</sup> and Phe<sup>264</sup> are found partially exposed to the solvent, and therefore if both or either of them interact with the lipid membrane, major conformational changes must occur to ensure that these critical residues come in close contact with the membrane surface. It has been shown that the binding of the Cry1Ab toxin to its receptor resulted in a conformational change in the toxin molecule consequently promoting complete proteolytic activation and pre-pore formation (51). Also, one study *via* disulphide bond-cross linking within the Cry1Aa toxin demonstrated that its ion-channel forming activity required the helical domain to swing away from the rest of the toxin molecule thus exposing the conserved helix 7 for the initial interaction with the membrane prior to the insertion of the transmembrane region (135).

To validate the function of the 65-kDa activated mutant toxins on the integrity of membrane vesicles, LUVs of PC/PE/Ch compositions, which are more

relevant to the insect cell membranes (136,137), were created with fluorimetric calcein entrapped in their interior cavity. The ability of the Y249L and F264L mutants (7.5  $\mu\text{g/ml}$ ) to exert perturbing activity towards lipid vesicles decreased ca. 50%, which is comparable to that of the wild-type. In addition, two double mutants, Y249L/F264L, revealed a drastically higher loss, with decreasing ca. 84% in perturbing activity. Thus, Tyr<sup>249</sup> and Phe<sup>264</sup> are likely to be involved in membrane perturbation of the Cry4Ba toxin. However, the ability of the helix 7 peptide used at the same amount as that of the 65-kDa Cry4Ba toxin could induce membrane-perturbing activity, with maximally release of only ca. 15% (**Figure 5.12**). In contrast, the loop  $\alpha 4$ - $\alpha 5$  peptide of Cry4Ba has been shown to fast induce the releasing of entrapped calcein from liposomes with maximally 70-80% (92). This low permeating activity of helix 7 peptides is probably due to its inability to penetrate deeply into the membrane from  $\alpha$ -helix structure as previously suggested for the Cry3A toxin (138). However, additional experiments are required to verify definitively the functional role of these two conserved aromatic residues by using more refined substitutions at these two critical residues, Tyr<sup>249</sup> and Phe<sup>264</sup> in the helix 7 peptide.

### 6.3 Characterisation of the helix 7 peptide in lipid membranes

To gain a better understanding about the functional role of  $\alpha 7$  of Cry4Ba, 27-residue and 31-residue peptides corresponding to  $\alpha 7$  and  $\alpha 6$  of the Cry4Ba toxin, respectively, were chemically synthesised and structurally and functionally characterised by ATR-FTIR spectroscopy. After purified by reverse-phase high performance liquid chromatography (RP-HPLC) and their purity were confirmed by mass spectrometry (see **Appendix 1**). The secondary structure of these two peptides when incorporated into three different types of phospholipid bilayers, DMPC, DMPG and DDPC was determined. It was found that the changes in the lipid types (DMPC, DMPG and DDPC) at various ratios of peptide-to-lipid (see **Table 5.1**) showed different secondary structure ratio for helix 7. However, it should be noted that the helix 7 peptide revealed a distinct  $\alpha$ -helical structure within all three types of lipids at the peptide-to-lipid molar ratio of 1:100, indicating that this helix is rather stable in the  $\alpha$ -helical conformation at a much higher lipid concentration, independently from

lipid environment. This is in agreement with Gazit and coworkers' data that showed predominantly  $\alpha$ -helicity about  $63.2\pm 4.8\%$  of  $\alpha 7$  peptide of the coleopteran-specific Cry3Aa toxin within phospholipid multibilayers (78).

The possible transition of secondary structure of helix 7 peptides can be influenced by the presence of different types of lipid membranes and the lipid concentrations (139). For example, neuropeptide substance P (SP) and its SP derivative, (Nle<sup>9</sup>)SP, in the presence of negatively charged POPG, both peptides showed the  $\beta$ -sheet structure at a low peptide-to-lipid ratio (<1:30) but adopted the helix conformation at high protein-to-lipid ratio (>1:40) (140). The Alzheimer amyloid peptide  $\beta_{AP(1-40)}$  was found to exhibit reversibly between the random coil and  $\beta$ -structure at low lipid-to-peptide ratios, but a  $\beta$ -structure to  $\alpha$ -helix transition was observed at peptide-to-lipid ratio > 1:55 (141). Another experiment of  $\beta_{AP(25-35)}$  has demonstrated a shift of the peptide conformation from random coil to 40-60%  $\beta$ -structure after adding the negatively charged lipid (142,143).

The orientation of the helix 7 peptide with respect to the lipid membrane was also investigated and the dichroic ratios obtained under different conditions used and the helix tilts are shown in **Table 5.2**. For the  $\beta$ -sheet form of the 27-residue helix 7 peptide, when bulk water was removed (**Figure 5.7, top and middle panels**), the amide I band dichroism (1.28 and 1.47 at lipid-to-peptide ratios of 1:5 and 1:30, respectively) indicated that the peptide was inserted into the DMPC membrane normal. Interestingly, after hydration in D<sub>2</sub>O, the dichroism of the amide A (1.76 and 1.56 at peptide-to-lipid ratios of 1:5 and 1:30, respectively, see **Table 5.2**) is more reliable which gives an average helix tilt of  $47^\circ\pm 1.2$ . For the  $\alpha$ -helical form of helix 7, the amide I band dichroism (see **Table 5.2**) showed that the peptides was localised at the DMPC membrane surface. On the other hand, all predominantly  $\alpha$ -helical structures were observed to be inserted into the DMPC at a lipid-to-protein ratio of 1:100 by a tilt angle of  $39^\circ\pm 0.8$ . A similar alpha-helical structure was observed to be inserted in negatively charged phospholipids, DMPG, at all peptide-to-lipid ratios.

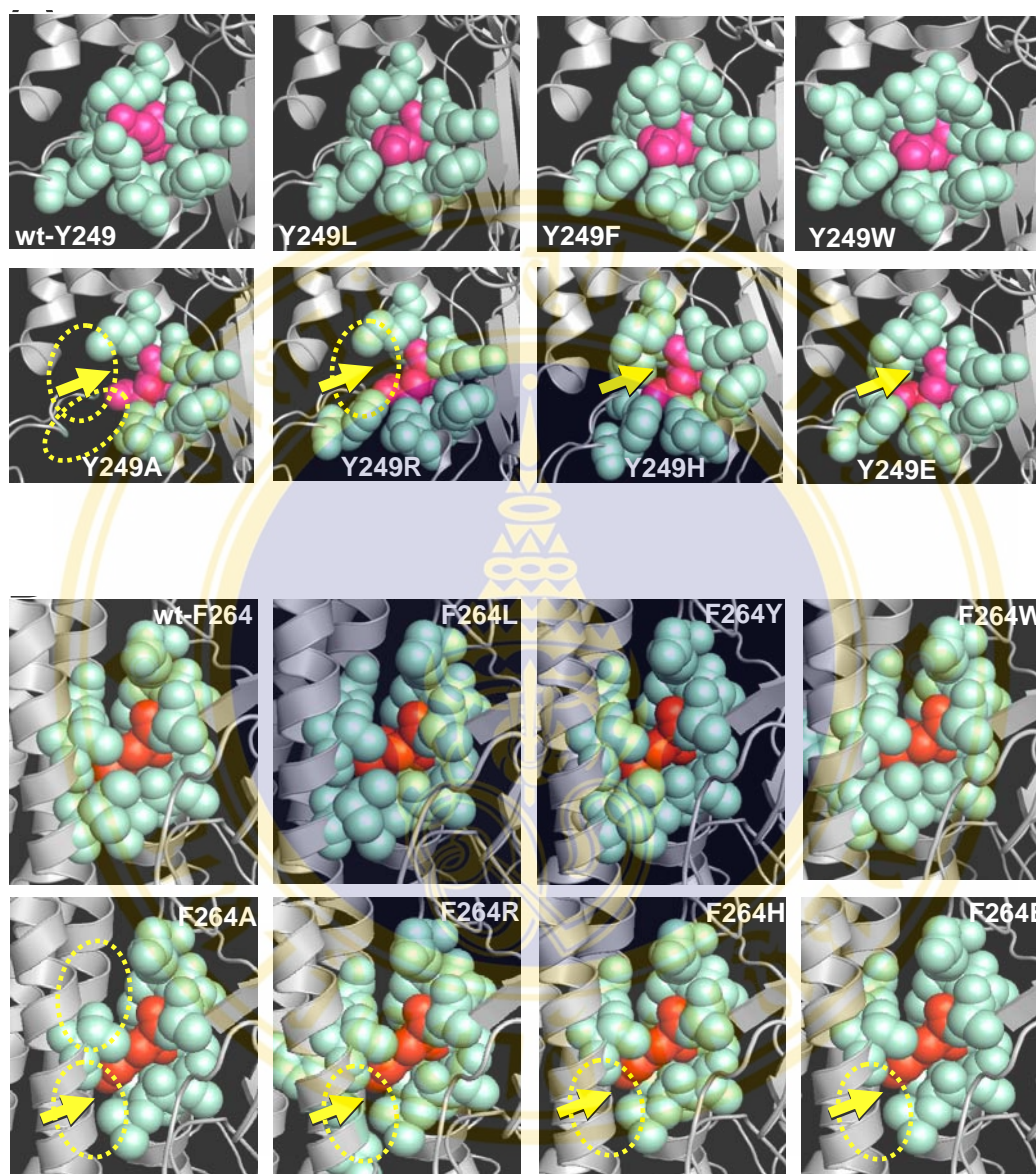


**Figure 6.1** Close-up views of part of the Cry4Ba crystal structure, illustrating the packing interactions

The figure shows the packing interactions (as shown in space-filling form) between residues at the two critical positions in  $\alpha 7$ , 249 (A) and 264 (B) and neighbouring hydrophobic residues within 4 Å, as analysed by Swiss-PdbViewer v.3.7. The arrows indicate cavities introduced inside the packing interactions of the mutant proteins. Positions of certain interacting residues that are absent from the packing clusters are encircled. The structures were generated by PyMOL program.

Evidence has shown that negatively charged phospholipids are crucial for changing the peptide conformation, e.g., the  $\alpha$ -helix formation of the  $\beta$ -amyloid peptide  $\beta_{AP(1-40)}$  was induced by the proper alignment of five positive charges in the presence of DMPG via mainly electrostatic interactions between the peptide and the lipid (141). Nevertheless, the helix 7 peptide has a net charge of -1 at physiological pH (see **Figure 5.5**), implying that the electrostatic interactions between peptide and the negatively charged DMPG was not effective. It is possible that  $\alpha$ -helix formation of helix 7 peptide could not be oriented essentially parallel to the membrane surface via these interactions. For this reason, the helix 7 peptide could penetrate into the DMPG membrane at all peptide-to-lipid molar ratios. However, when short-chain phospholipid membrane, DDPC, was employed, a bandshape of the amide I obtained was similar to that observed in DMPC system. Although it displayed the  $\beta$ -sheet more obviously than  $\alpha$ -helix of the amide I contour for two different protein-to-lipid ratios (1:5 and 1:30), the amide I band dichroism of helix 7-peptide/DDPC indicated that  $\alpha$ -helical conformation are absolutely located at the membrane surface at protein-to-lipid ratio of 1:30. This is consistent with 48% insertion of this peptide at protein-to-lipid ratio of 1:100. In addition, the presence of DDPC lipid, the peptide also exhibited  $\beta$ -structure, which could penetrate into lipid membrane, giving a helix tilt of  $62^\circ$  and  $41^\circ$  at protein-to-lipid ratios of 1:5 and 1:30, respectively. In these results, it was observed that the behaviors or orientations of the helix 7 peptide in either DMPC or DDPC are rather similar by showing  $\alpha$ -helix formation locating at the membrane surface and  $\beta$ -structure penetrating into the lipid membrane. Interestingly, one of major phospholipids found in the insect cell membranes is phosphatidylcholine (PC) (136,137). This feature might therefore imply a functional role for helix 7 of the Cry4Ba toxin in these lipid conditions. Further characterisation of the effect on the integrity of membrane vesicles of the  $\beta$ -structure peptide that was conceivably inserted in the membrane (see above) was also carried out. As was mentioned earlier that the ability of the helix 7 peptide ( $2.3 \mu\text{M}$ ) to induce membrane permeability was much lower than the full length active Cry4Ba toxin (see **Figure 5.13**). It might be possible that  $\beta$ -sheet structure form by helix 7 peptides could not span across the lipid bilayer for creating pores or channels (144).

For determining the spatial orientations of the  $\alpha$ -helical peptide that is localised on the membrane, CN stretching vibration was measured for the helix 7 peptide labelled with cyano group at Phe<sup>7</sup> (Phe<sub>CN</sub>) (see **Figure 5.5**). The result revealed that the CN stretching vibration is centred at  $\sim 2228 \text{ cm}^{-1}$  (**Figure 5.12**), indicating that the Phe<sub>CN</sub> side chain in the peptide is buried in the hydrophobic region of the membrane. It should be also noted that the CN stretching vibration of the peptide shifts to lower wavenumbers at the positions that are almost identical to those obtained on a Phe<sub>CN</sub> residue that is buried in a hydrophobic pocket (109). If this CN labelling peptide is in water, it would exhibit a CN stretching vibration centered at  $\sim 2235 \text{ cm}^{-1}$  (110). According to the position of the aromatic-side chain of Phe<sup>7</sup> (Phe<sub>CN</sub>), Tyr<sup>10</sup> and Phe<sup>25</sup> in the helix 7 peptide would be therefore believed to point towards the bilayer membrane (see **Figure 6.3**). It is noteworthy that Tyr<sup>10</sup> and Phe<sup>25</sup> in the helix 7 peptide correspond to the two highly conserved residues, Tyr<sup>249</sup> and Phe<sup>264</sup>, which are important for toxicity of Cry4Ba. Therefore, these two critical aromatic residues in helix 7 may indeed play a role in toxin-membrane interaction that is needed for an efficient membrane insertion and pore formation of the Cry4Ba toxin.

#### 6.4 Structure and dynamics of the helix 7 peptide in DMPC bilayers

MD simulations in the DMPC bilayer system of the helix 7 peptide were carried out based upon the ATR-FTIR data. An  $\alpha$ -helical model was placed at the membrane water-interface region with an aromatic side chain of Phe<sup>7</sup> pointing towards the membrane while a  $\beta$ -structure model was inserted transversely into a bilayer membrane. For  $\alpha$ -helical model/DMPC surface, the RMSD fluctuates between  $\sim 0.18$  and  $0.3 \text{ nm}$  after for simulation  $4.75 \text{ ns}$  (see **Figure 5.15A**). However, the diagrams of secondary structure versus time for the conformational dynamics of  $\alpha$ -helical models revealed that the  $\alpha$ -helical conformation is largely preserved throughout the simulation time (**Figure 5.15B**). This reflects a small conformational change in the helix when the peptide is at the membrane surface or the peptide is quite stable throughout simulations. Moreover, the helix orientation is nearly parallel to the membrane surface, with an average angle of  $\sim 90^\circ$ , as shown similar to the data in the previous studies (78,145). Interestingly, Tyr<sup>10</sup> and Phe<sup>25</sup> in the helix 7, corresponding

to the two highly conserved residues, Tyr<sup>249</sup> and Phe<sup>264</sup> of Cry4Ba still retained pointing their aromatic side chains towards the bilayers that is consistent with the results of ATR-FTIR measurements (**Figure 6.3**). For the  $\beta$ -structure model/DMPC, the position of Phe<sup>25</sup> is likely to be at the membrane water-interface, but Tyr<sup>10</sup> is pointing towards the hydrophobic region of the bilayers. However, this simulation was run for only 10 ns. Further significant changes in the position of Tyr<sup>10</sup> and Phe<sup>25</sup> might have occurred if the simulation lengths were extended.



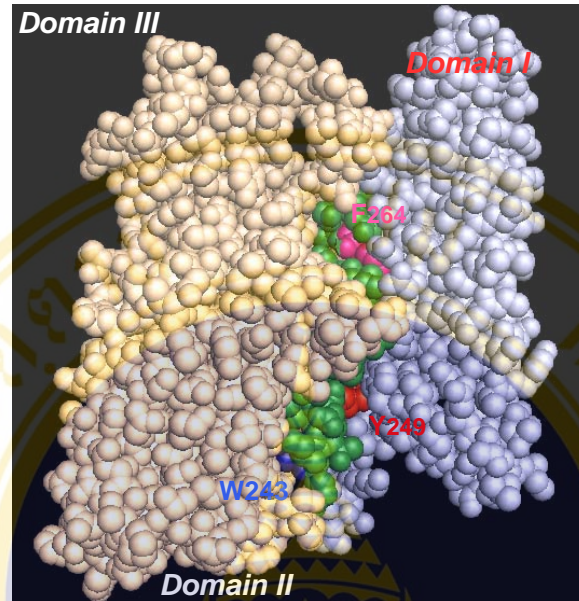


**Figure 6.2 Space-filling representation of the Cry4Ba structure**

The figure shows space-filling representation of the Cry4Ba structure showing locations of the two critical aromatic residues, Tyr<sup>249</sup> (red) and Phe<sup>264</sup> (pink) in helix 7 (green). The structures were generated by PyMOL program.

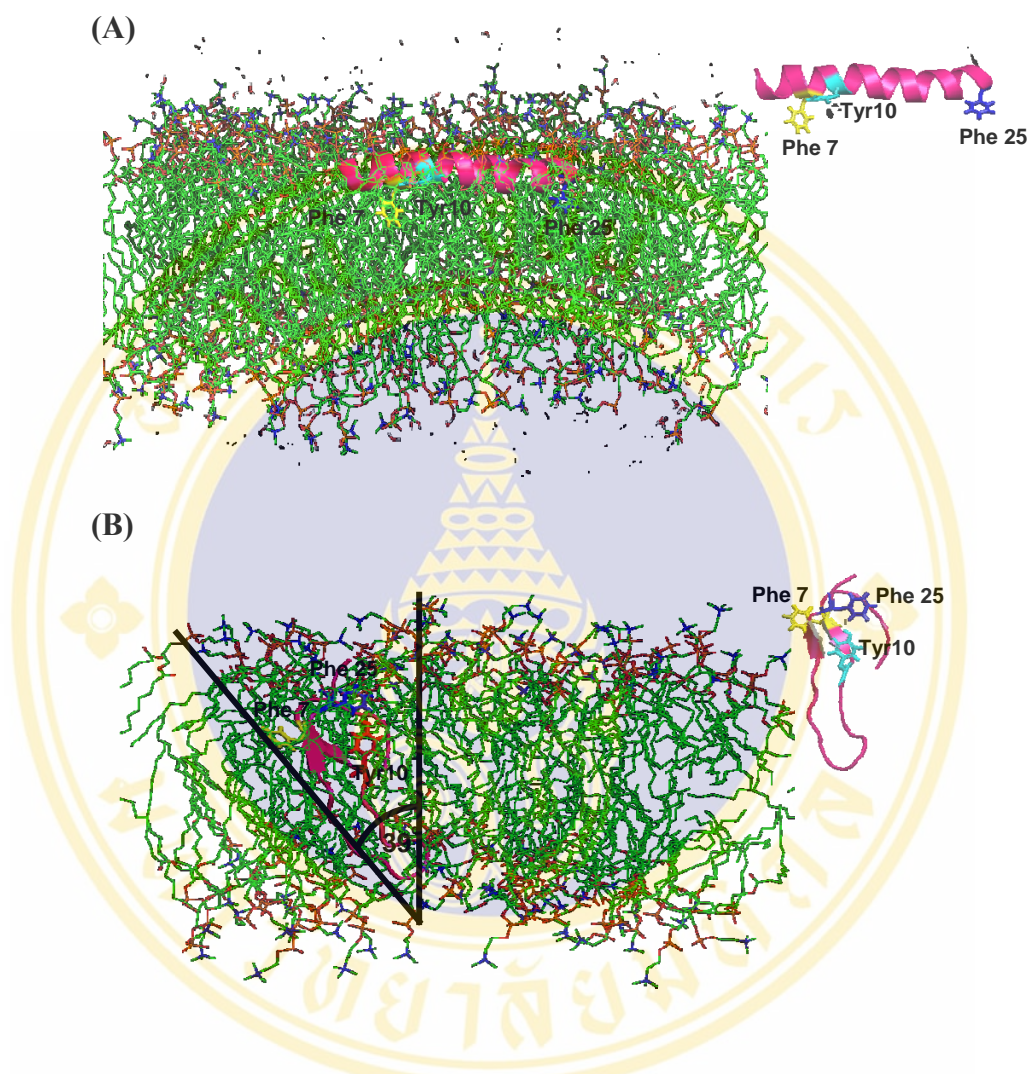


**Figure 6.3 The snapshot of helix 7 peptide at the membrane water-interface and in the DMPC bilayers**

The figure shows (A) snapshot at simulation time = 10 ns of the helical model at the membrane water-interface region and (B) at time = 10 ns of the  $\beta$ -hairpin model in the DMPC bilayers. Positions of two critical aromatic residues, Tyr<sup>249</sup> and Phe<sup>264</sup>, in the simulation system are indicated as Tyr<sup>10</sup> and Phe<sup>25</sup>, respectively and snapshot at  $t=10$ ns of the helical (A) and beta-hairpin (B) model without the membrane bilayers.

Recent studies with the bacterial toxin pneumolysin and the other members of the highly conserved of the cholesterol-dependent cytolysin (CDC) family. It has been shown that there is the transition from the prepore to the pore by an astonishing conformational change in the protein monomer between the prepore, which includes one part of the protein changing from an alpha helix into an extended beta structure to insert into a lipid environment (146) (see **Figure 6.4**). Thus, this may conceivably reflect our results that  $\alpha$ -helix formation of helix 7 peptide refold into an extended  $\beta$ -hairpin to insert into a lipid environment for the Cry4Ba toxicity. Interestingly, how  $\beta$ -hairpin structure folds and insert into the membrane, the rivet-like conformation was chosen to describe. Based on a revised alignment among putative transmembrane domains of different  $\beta$ -barrel pore-forming toxin (PFT) (147), in the middle of the predicted  $\beta$ -hairpin model used in MDs experiment, it found four hydrophobic residues, I<sub>16</sub>QVL sequence, which also seems relevant for aerolysin toxin and other  $\beta$ -barrel PFT (see **Figure 6.5**). It has been revealed that the turn of the  $\beta$ -hairpin is composed of a stretch of five hydrophobic residues (WPLVG) and this hydrophobic turn could drive to membrane insertion. Therefore, the four hydrophobic residues (I<sub>16</sub>QVL) in helix 7 peptides of Cry4Ba might be a factor to form  $\beta$ -hairpin structure of the peptide inserted in to the membrane.

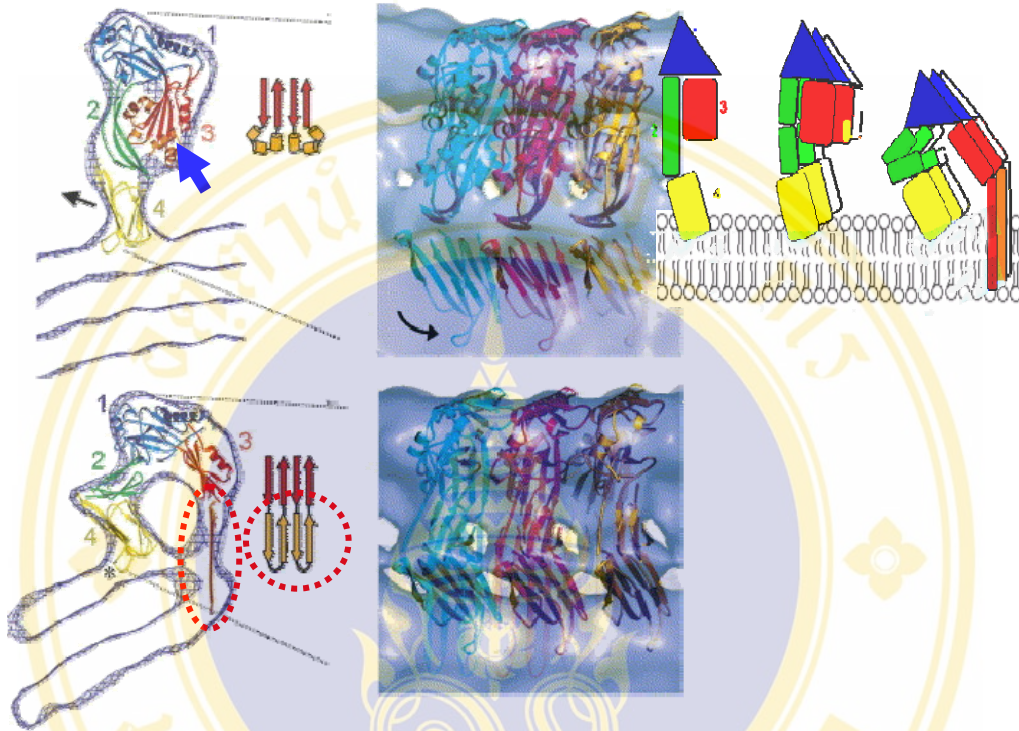
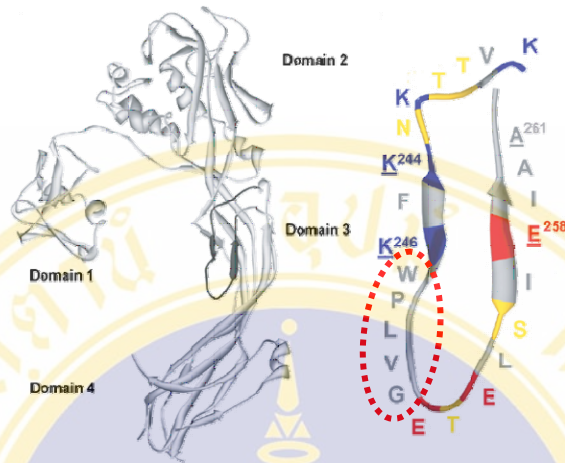


**Figure 6.4** Atomic structure fits of prepore and pore structures of the pneumolysin toxin (146)

The figure shows cross-section through one side of the prepore map with the fitted domains of one subunit. The part the protein changing of domain III from an alpha helix into an extended beta structure to insert into a lipid environment is indicated by blue arrow and red circle. Coloring: domain 1, blue; domain 2, green; domain 3, red (predicted transmembrane regions, orange); domain 4, yellow.

(A)



(B)

**Cry4Ba** NGQWITFNDYKREMTIQVLDILALFAS

	S	E	K	V	T	T	K	N	K	F	K	-	W	P	L	V	G	-	E	T	E	L	S	I	E	I	A	A	N	Q	
Aerolysin	T	V	G	T	S	-	Q	A	T	A	K	-	T	T	V	T	N	-	-	E	T	G	V	S	L	T	T	S	Y	S	F
Epsilon	G	V	K	T	S	-	K	V	G	L	E	-	A	I	A	-	-	-	-	D	S	K	V	E	T	S	F	E	F	N	A
Clost. α-toxin	W	F	N	F	K	Y	E	T	K	Q	E	V	S	I	G	T	A	-	R	Q	T	W	T	S	T	L	N	A	G	V	
Enterolysin	T	L	T	Y	G	F	N	G	N	V	T	G	D	D	T	G	K	I	G	G	L	I	G	A	N	V	S	I	G	H	
Staph. α-toxin	T	L	G	Y	N	I	G	G	K	F	Q	-	S	V	P	S	I	G	G	N	G	S	-	-	F	N	Y	S	K		
LukM	T	L	G	Y	N	I	G	G	N	F	Q	-	S	A	P	T	L	G	G	-	K	G	E	-	-	F	N	Y	S	K	
LukS-I	T	S	E	V	H	G	N	A	E	V	H	A	S	E	F	D	I	G	G	-	S	V	S	A	G	F	S	N	S	N	
Anthrax PA																															

	Q	I	S	S	A	L	N	V	N	A	-	K	-	V	L	-	-	E	N	S	L	G	V	D	F	N	A	V	A	
PFO	Q	I	E	A	A	L	N	V	N	S	-	K	-	L	-	-	D	G	T	L	G	I	D	F	K	S	I	S		
SLO	Q	I	A	K	F	G	T	A	F	-	K	-	A	V	-	-	N	N	S	L	N	V	N	F	G	A	I	S		
LLO	Q	L	K	V	K	F	G	S	D	F	E	K	T	G	N	S	L	D	-	D	E	N	S	V	H	S	G	E		
PLY	Q	L	Q	A	K	F	G	A	D	F	S	K	V	G	A	P	L	N	V	-	D	E	S	S	V	H	K	E		
ILY	T	S	S	S	K	D	V	Q	A	A	F	K	A	L	I	K	N	T	D	L	K	N	S	Q	Q	Y	K	D	I	
PFO	S	S	K	S	N	D	V	E	A	A	F	S	A	A	L	K	G	T	D	V	K	T	N	G	K	Y	S	D	I	
SLO	N	S	H	S	T	K	V	K	A	A	F	D	A	A	V	S	G	K	S	V	S	G	D	V	E	L	T	N	I	
LLO	T	S	K	S	D	E	V	E	A	A	F	E	A	L	I	K	G	V	K	V	A	P	Q	T	E	W	K	Q	I	
PLY	T	S	K	S	T	K	V	Q	A	A	I	D	A	V	V	K	G	A	K	L	K	A	G	T	E	Y	E	N	I	
ILY																														

**Figure 6.5 Proaerolysin structure and alignments of putative transmembrane domains of different β-barrel PFT (147)**

The figure shows (A) schematic representation of a stretch of five hydrophobic residues (WPSVG) driving membrane insertion that is indicated in red circle. (B) Sequence alignment of helix 7 peptide of Cry4Ba with among putative transmembrane domains of different β-barrel PFT. A stretch of five hydrophobic residues of aerolysin-like pore-forming toxins is indicated by blue box and four hydrophobic residues (I<sub>16</sub>QVL) is indicated by red letters.

## CHAPTER VII

### CONCLUSIONS

1. Alanine substitutions of four highly conserved aromatic residues, Trp<sup>243</sup>, Phe<sup>246</sup>, Tyr<sup>249</sup> and Phe<sup>264</sup>, in helix 7 of the *Bt* Cry4Ba mosquito-larvicidal protein was initially performed. Bioassays against *S. aegypti* mosquito-larvae revealed that only Trp<sup>243</sup>, Tyr<sup>249</sup> or Phe<sup>264</sup> are essential for larvicidal activity.
2. Further mutagenic analysis using more refined substitutions at two critical residues, Tyr<sup>249</sup> and Phe<sup>264</sup> that oriented their aromatic side chains face towards in the same direction, was performed. It showed that replacements with an aromatic residue at both positions still retained the high-level toxin activity. However, a nearly complete loss in larvicidal activity was found for Y249L/F264L or F264A/Y249A double mutants, confirming the involvement in toxicity of both aromatic residues which face towards the same direction. However, the exact role of Trp<sup>243</sup> that is buried within the domain I-II interface and located opposite to Tyr<sup>249</sup> and Phe<sup>264</sup> in the structure and function of the Cry4Ba toxin remains to be clearly elucidated.
3. All the toxin inclusions of the larvicidal-active mutants that were substituted with an aromatic and hydrophobic residue were found to be soluble in the carbonate buffer, pH 10.0. On the other hand, a complete loss of the inclusion solubility was found for all the remaining mutants possibly due to a disruption of hydrophobic packing of several hydrophobic residues within 4 Å. Altogether, the study provides the highly conserved aromaticity of Tyr<sup>249</sup> and Phe<sup>264</sup> within helix 7 playing an important role in larvicidal activity of the Cry4Ba toxin.
4. The far-UV CD spectroscopy revealed that all the CD profiles of the FPLC-purified trypsin-treated mutants, Y249L, F264L and Y249L/F264L, are basically similar. Although, both Y249L and Y249L/F264L, whose CD spectra were much the same, had small reduced CD intensity in the region between 210 and 222 nm

compared to the wild-type and F264L mutant, trypsin digestion assays as demonstrated earlier revealed that such little conformational changes did not cause misfolding of the Y249L and Y249L/F264L mutant proteins. In addition, it has been confirmed by their intrinsic fluorescence spectra displaying the same overall tertiary structure in both mutants and wild-type Cry4Ba toxin.

5. The entrapped dye-release experiments suggested that Tyr<sup>249</sup> and Phe<sup>264</sup> are involved in membrane perturbation of the Cry4Ba toxin since the membrane-perturbing ability of the bio-inactive mutants (Y249L, F264L and Y249L/F264L) was much weaker than the wild-type toxin.

6. For ATR-FTIR studies, the helix 7 peptide with DMPC showed two major component bands at 1633 and 1654 cm<sup>-1</sup> that are assigned to  $\beta$ -sheet and  $\alpha$ -helical structures, respectively. However, all helix 7 peptides mixing with DMPG and DDPC is predominantly centered at 1655 and 1631 cm<sup>-1</sup>, respectively. This indicates that the peptide incorporated in DMPG can be attributed to  $\alpha$ -helical structure, whilst the peptide within DDPC adopts a predominantly  $\beta$ -sheet structure. Moreover, changes in the peptide-lipid ratio revealed variations in the peptide conformational ratio of  $\alpha$ -helix to  $\beta$ -structure. Hydrogen/deuterium exchange suggested that the  $\beta$ -form was approximately 90% insertion into the DMPC membrane bilayers with an average tilt angle of 47°, whilst the  $\alpha$ -helical form was placed on the membrane surface with ~40% insertion by both critical aromatic residues, Tyr<sup>249</sup> and Phe<sup>264</sup> point towards the membrane.

7. 10-ns MD simulations of both conformations in the DMPC bilayers is consistent with that was observed in ATR-FTIR experiments. Moreover, Tyr<sup>10</sup> and Phe<sup>25</sup> in the helix 7, corresponding to the two highly conserved residues, Tyr<sup>249</sup> and Phe<sup>264</sup> of Cry4Ba still retained pointing their aromatic side chains towards the bilayers that is also consistent with the results of ATR-FTIR measurements.

## REFERENCES

1. Duche D, Izard J, Gonzalez-Manas JM, Parker MW, Crest M, Chartier M. Membrane topology of the colicin A pore-forming domain analyzed by disulfide bond engineering. *J Biol Chem* 1996;271(26):15401-15406.
2. Schwartz JL, Juteau M, Grochulski P, Cygler M, Prefontaine G, Brousseau R. Restriction of intramolecular movements within the Cry1Aa toxin molecule of *Bacillus thuringiensis* through disulfide bond engineering. *FEBS Lett* 1997;410(2-3):397-402.
3. Kawate T, Gouaux E. Arresting and releasing Staphylococcal alpha-hemolysin at intermediate stages of pore formation by engineered disulfide bonds. *Protein Sci* 2003;12(5):997-1006.
4. Kristan K, Podlesek Z, Hojnik V, Gutierrez-Aguirre I, Guncar G, Turk D. Pore formation by equinatoxin II, a eukaryotic pore-forming toxin, requires a flexible N-terminal region and a stable beta-sandwich. *J Biol Chem* 2004;279(45):46509-46517.
5. Parker MW, Feil SC. Pore-forming protein toxins: from structure to function. *Prog Biophys Mol Biol* 2005;88(1):91-142.
6. Lesieur C, Vecsey-Semjen B, Abrami L, Fivaz M, Gisou van der Goot F. Membrane insertion: The strategies of toxins (review). *Mol Membr Biol* 1997;14(2):45-64.
7. Gouaux E. Channel-forming toxins: tales of transformation. *Curr Opin Struct Biol* 1997;7(4):566-573.
8. Li J, Carroll J, Ellar DJ. Crystal structure of insecticidal delta-endotoxin from *Bacillus thuringiensis* at 2.5 Å resolution. *Nature* 1991;353(6347):815-821.
9. Bulla LA, Jr., Davidson LI, Kramer KJ, Jones BL. Purification of the insecticidal toxin from the parasporal crystal of *Bacillus thuringiensis* subsp. *kurstaki*. *Biochem Biophys Res Commun* 1979;91(3):1123-1130.
10. Aronson AI, Tyrell DJ, Fitz-James PC, Bulla LA, Jr. Relationship of the syntheses of spore coat protein and parasporal crystal protein in *Bacillus thuringiensis*. *J Bacteriol* 1982;151(1):399-410.

11. Schnepf E, Crickmore N, Van Rie J, Lereclus D, Baum J, Feitelson J. *Bacillus thuringiensis* and its pesticidal crystal proteins. *Microbiol Mol Biol Rev* 1998;62(3):775-806.
12. de Maagd RA, Bravo A, Crickmore N. How *Bacillus thuringiensis* has evolved specific toxins to colonize the insect world. *Trends Genet* 2001;17(4):193-199.
13. Bulla LA. Bacteria as insect pathogens. *Annu Rev Microbiol* 1975;29:163-190.
14. Becker N, Ludwig M. Investigations on possible resistance in *Aedes vexans* field populations after a 10-year application of *Bacillus thuringiensis israelensis*. *J Am Mosq Control Assoc* 1993;9(2):221-224.
15. Hofte H, Whiteley HR. Insecticidal crystal proteins of *Bacillus thuringiensis*. *Microbiol Rev* 1989;53(2):242-255.
16. Crickmore N, Zeigler DR, Feitelson J, Schnepf E, Van Rie J, Lereclus D. Revision of the nomenclature for the *Bacillus thuringiensis* pesticidal crystal proteins. *Microbiol Mol Biol Rev* 1998;62(3):807-813.
17. Chungjatupornchai W, Hofte H, Seurinck J, Angsuthanasombat C, Vaeck M. Common features of *Bacillus thuringiensis* toxins specific for Diptera and Lepidoptera. *Eur J Biochem* 1988; 173(1):9-16.
18. Grochulski P, Masson L, Borisova S, Pusztai-Carey M, Schwartz JL, Brousseau R. *Bacillus thuringiensis* CryIA(a) insecticidal toxin: crystal structure and channel formation. *J Mol Biol* 1995;254(3):447-464.
19. Derbyshire DJ, Ellar DJ, Li J. Crystallization of the *Bacillus thuringiensis* toxin Cry1Ac and its complex with the receptor ligand N-acetyl-D-galactosamine. *Acta Crystallogr D Biol Crystallogr* 2001;57(Pt 12):1938-1944.
20. Morse RJ, Yamamoto T, Stroud RM. Structure of Cry2Aa suggests an unexpected receptor binding epitope. *Structure* 2001;9(5):409-417.
21. Boonserm P, Davis P, Ellar DJ, Li J. Crystal structure of the mosquito-larvicidal toxin Cry4Ba and its biological implications. *J Mol Biol* 2005;348(2):363-382.

22. Boonserm P, Mo M, Angsuthanasombat C, Lescar J. Structure of the functional form of the mosquito larvicidal Cry4Aa toxin from *Bacillus thuringiensis* at a 2.8-angstrom resolution. *J Bacteriol* 2006;188(9):3391-3401.
23. Alcantara EP, Alzate O, Lee MK, Curtiss A, Dean DH. Role of alpha-helix seven of *Bacillus thuringiensis* Cry1Ab delta-endotoxin in membrane insertion, structural stability, and ion channel activity. *Biochemistry* 2001;40(8):2540-2547.
24. Nunez-Valdez M, Sanchez J, Lina L, Guereca L, Bravo A. Structural and functional studies of alpha-helix 5 region from *Bacillus thuringiensis* Cry1Ab delta-endotoxin. *Biochim Biophys Acta* 2001;1546(1):122-131.
25. Kumar AS, Aronson AI. Analysis of mutations in the pore-forming region essential for insecticidal activity of a *Bacillus thuringiensis* delta-endotoxin. *J Bacteriol* 1999;181(19):6103-6107.
26. Uawithya P, Tuntitippawan T, Katzenmeier G, Panyim S, Angsuthanasombat C. Effects on larvicidal activity of single proline substitutions in alpha3 or alpha4 of the *Bacillus thuringiensis* Cry4Ba toxin. *Biochem Mol Biol Int* 1998;44(4):825-832.
27. Rajamohan F, Lee MK, Dean DH. *Bacillus thuringiensis* insecticidal proteins: molecular mode of action. *Prog Nucleic Acid Res Mol Biol* 1998;60:1-27.
28. Shimizu T, Morikawa K. The beta-prism: a new folding motif. *Trends Biochem Sci* 1996;21(1):3-6.
29. Burton SL, Ellar DJ, Li J, Derbyshire DJ. N-acetylgalactosamine on the putative insect receptor aminopeptidase N is recognised by a site on the domain III lectin-like fold of a *Bacillus thuringiensis* insecticidal toxin. *J Mol Biol* 1999;287(5):1011-1022.
30. de Maagd RA, Bakker PL, Masson L, Adang MJ, Sangadala S, Stiekema W, et al. Domain III of the *Bacillus thuringiensis* delta-endotoxin Cry1Ac is involved in binding to *Manduca sexta* brush border membranes and to its purified aminopeptidase N. *Mol Microbiol* 1999;31(2):463-471.
31. Lee MK, You TH, Gould FL, Dean DH. Identification of residues in domain III of *Bacillus thuringiensis* Cry1Ac toxin that affect binding and toxicity. *Appl Environ Microbiol* 1999;65(10):4513-4520.

32. Masson L, Tabashnik BE, Mazza A, Prefontaine G, Potvin L, Brousseau R. Mutagenic analysis of a conserved region of domain III in the CryIAc toxin of *Bacillus thuringiensis*. *Appl Environ Microbiol* 2002;68(1):194-200.
33. Chen XJ, Curtiss A, Alcantara E, Dean DH. Mutations in domain I of *Bacillus thuringiensis* delta-endotoxin CryIAb reduce the irreversible binding of toxin to *Manduca sexta* brush border membrane vesicles. *J Biol Chem* 1995;270(11):6412-6419.
34. Schwartz JL, Potvin L, Chen XJ, Brousseau R, Laprade R, Dean DH. Single-site mutations in the conserved alternating-arginine region affect ionic channels formed by CryIAa, a *Bacillus thuringiensis* toxin. *Appl Environ Microbiol* 1997;63(10):3978-3984.
35. Wolfersberger MG, Chen XJ, Dean DH. Site-directed mutations in the third domain of *Bacillus thuringiensis* delta-endotoxin CryIAa affect its ability to increase the permeability of *Bombyx mori* midgut brush border membrane vesicles. *Appl Environ Microbiol* 1996;62(1):279-282.
36. Knowles BH. Mechanism of action of *Bacillus thuringiensis* insecticidal delta-endotoxins. *Adv Insect Physiol* 1994;24:275-308.
37. Whalon ME, Wingerd BA. *Bt*: mode of action and use. *Arch Insect Biochem Physiol* 2003;54(4):200-211.
38. Hofte H, de Greve H, Seurinck J, Jansens S, Mahillon J, Ampe C. Structural and functional analysis of a cloned delta endotoxin of *Bacillus thuringiensis* berliner 1715. *Eur J Biochem* 1986;161(2):273-280.
39. Choma CT, Surewicz WK, Carey PR, Pozsgay M, Raynor T, Kaplan H. Unusual proteolysis of the protoxin and toxin from *Bacillus thuringiensis*. Structural implications. *Eur J Biochem* 1990;189(3):523-527.
40. Angsuthanasombat C, Uawithya P, Leetachewa S, Pornwiroon W, Ounjai P, Kerdcharoen T, Katzenmeier GR, Panyim S. *Bacillus thuringiensis* Cry4A and Cry4B mosquito-larvicidal proteins: homology-based 3D model and implications for toxin activity. *J Biochem Mol Biol* 2004; 37(3):304-313.
41. Angsuthanasombat C, Crickmore N, Ellar DJ. Effects on toxicity of eliminating a cleavage site in a predicted interhelical loop in *Bacillus thuringiensis* CryIVB delta-endotoxin. *FEMS Microbiol Lett* 1993;111(2-3):255-261.

42. Carroll J, Li J, Ellar DJ. Proteolytic processing of a coleopteran-specific delta-endotoxin produced by *Bacillus thuringiensis* var. *tenebrionis*. *Biochem J* 1989;261(1):99-105.
43. Nicholls CN, Ahmad W, Ellar DJ. Evidence for two different types of insecticidal P2 toxins with dual specificity in *Bacillus thuringiensis* subspecies. *J Bacteriol* 1989; 171(9):5141-5147.
44. Sekar V, Held B, Tippett J, Amirhusin B, Robeff P, Wang K. Biochemical and molecular characterization of the insecticidal fragment of CryV. *Appl Environ Microbiol* 1997;63(7):2798-2801.
45. Bravo A, Gill SS, Soberon M. *Bacillus thuringiensis* mechanisms and use. In: *Comprehensive molecular insect science*. Elsevier B. V. 2005:175-206.
46. Hill CA, Pinnock DE. Histopathological effects of *Bacillus thuringiensis* on the alimentary canal of the sheep louse, *Bovicola ovis*. *J Invertebr Pathol* 1998;72(1):9-20.
47. Jurat-Fuentes JL, Adang MJ. Characterization of a Cry1Ac-receptor alkaline phosphatase in susceptible and resistant *Heliothis virescens* larvae. *Eur J Biochem* 2004;271(15):3127-3135.
48. Knight PJ, Crickmore N, Ellar DJ. The receptor for *Bacillus thuringiensis* Cry1A(c) delta-endotoxin in the brush border membrane of the lepidopteran *Manduca sexta* is aminopeptidase N. *Mol Microbiol* 1994;11(3):429-436.
49. Nagamatsu Y, Koike T, Sasaki K, Yoshimoto A, Furukawa Y. The cadherin-like protein is essential to specificity determination and cytotoxic action of the *Bacillus thuringiensis* insecticidal CryIAa toxin. *FEBS Lett* 1999;460(2):385-390.
50. Valaitis AP, Jenkins JL, Lee MK, Dean DH, Garner KJ. Isolation and partial characterization of gypsy moth BTR-270, an anionic brush border membrane glycoconjugate that binds *Bacillus thuringiensis* Cry1A toxins with high affinity. *Arch Insect Biochem Physiol* 2001;46(4):186-200.
51. Griffiths JS, Haslam SM, Yang T, Garczynski SF, Mulloy B, Morris H. Glycolipids as receptors for *Bacillus thuringiensis* Crystal toxin. *Science* 2005;307:922-925.

52. Chen J, Brown MR, Hua G, Adang MJ. Comparison of the localization of *Bacillus thuringiensis* Cry1A delta-endotoxins and their binding proteins in larval midgut of tobacco hornworm, *Manduca sexta*. *Cell Tissue Res* 2005;321(1):123-129.
53. Gahan LJ, Gould F, Heckel DG. Identification of a gene associated with *Bt* resistance in *Heliothis virescens*. *Science* 2001;293(5531):857-860.
54. Morin S, Biggs RW, Sisterson MS, Shriver L, Ellers-Kirk C, Higginson D. Three cadherin alleles associated with resistance to *Bacillus thuringiensis* in pink bollworm. *Proc Natl Acad Sci U S A* 2003;100(9):5004-5009.
55. Oltean DI, Pullikuth AK, Lee HK, Gill SS. Partial purification and characterization of *Bacillus thuringiensis* Cry1A toxin receptor A from *Heliothis virescens* and cloning of the corresponding cDNA. *Appl Environ Microbiol* 1999;65(11):4760-4766.
56. Herrero S, Gechev T, Bakker PL, Moar WJ, de Maagd RA. *Bacillus thuringiensis* Cry1Ca-resistant *Spodoptera exigua* lacks expression of one of four Aminopeptidase N genes. *BMC Genomics* 2005;6:96.
57. Rajagopal R, Sivakumar S, Agrawal N, Malhotra P, Bhatnagar RK. Silencing of midgut aminopeptidase N of *Spodoptera litura* by double-stranded RNA establishes its role as *Bacillus thuringiensis* toxin receptor. *J Biol Chem* 2002;277(49):46849-46851.
58. Gill M, Ellar D. Transgenic *Drosophila* reveals a functional in vivo receptor for the *Bacillus thuringiensis* toxin Cry1Ac1. *Insect Mol Biol* 2002;11(6):619-625.
59. Atsumi S, Mizuno E, Hara H, Nakanishi K, Kitami M, Miura N. Location of the *Bombyx mori* aminopeptidase N type 1 binding site on *Bacillus thuringiensis* Cry1Aa toxin. *Appl Environ Microbiol* 2005;71(7):3966-3977.
60. McNall RJ, Adang MJ. Identification of novel *Bacillus thuringiensis* Cry1Ac binding proteins in *Manduca sexta* midgut through proteomic analysis. *Insect Biochem Mol Biol* 2003;33(10):999-1010.
61. Munro S. Lipid rafts: elusive or illusive? *Cell* 2003;115(4):377-388.

62. Bravo A, Gomez I, Conde J, Munoz-Garay C, Sanchez J, Miranda R. Oligomerization triggers binding of a *Bacillus thuringiensis* Cry1Ab pore-forming toxin to aminopeptidase N receptor leading to insertion into membrane microdomains. *Biochim Biophys Acta* 2004;1667(1):38-46.
63. Zhuang M, Oltean DI, Gomez I, Pullikuth AK, Soberon M, Bravo A. *Heliothis virescens* and *Manduca sexta* lipid rafts are involved in Cry1A toxin binding to the midgut epithelium and subsequent pore formation. *J Biol Chem* 2002;277(16):13863-13872.
64. Gomez I, Sanchez J, Miranda R, Bravo A, Soberon M. Cadherin-like receptor binding facilitates proteolytic cleavage of helix alpha-1 in domain I and oligomer pre-pore formation of *Bacillus thuringiensis* Cry1Ab toxin. *FEBS Lett* 2002;513(2-3):242-246.
65. Rausell C, Munoz-Garay C, Miranda-CassoLuengo R, Gomez I, Rudino-Pinera E, Soberon M. Tryptophan spectroscopy studies and black lipid bilayer analysis indicate that the oligomeric structure of Cry1Ab toxin from *Bacillus thuringiensis* is the membrane-insertion intermediate. *Biochemistry* 2004;43(1):166-174.
66. Buzdin AA, Revina LP, Kostina LI, Zalunin IA, Chestukhina GG. Interaction of 65- and 62-kD proteins from the apical membranes of the *Aedes aegypti* larvae midgut epithelium with Cry4B and Cry11A endotoxins of *Bacillus thuringiensis*. *Biochemistry (Mosc)* 2002;67(5):540-546.
67. Fernandez LE, Aimanova KG, Gill SS, Bravo A, Soberon M. A GPI-anchored alkaline phosphatase is a functional midgut receptor of Cry11Aa toxin in *Aedes aegypti* larvae. *Biochem J* 2006;394(Pt 1):77-84.
68. Fernandez LE, Perez C, Segovia L, Rodriguez MH, Gill SS, Bravo A. Cry11Aa toxin from *Bacillus thuringiensis* binds its receptor in *Aedes aegypti* mosquito larvae through loop alpha-8 of domain II. *FEBS Lett* 2005;579(17):3508-35014.
69. Wu SJ, Dean DH. Functional significance of loops in the receptor binding domain of *Bacillus thuringiensis* CryIII delta-endotoxin. *J Mol Biol* 1996;255(4):628-640.

70. Lu H, Rajamohan F, Dean DH. Identification of amino acid residues of *Bacillus thuringiensis* delta-endotoxin CryIAa associated with membrane binding and toxicity to *Bombyx mori*. J Bacteriol 1994;176(17):5554-5559.
71. Lee MK, Rajamohan F, Jenkins JL, Curtiss AS, Dean DH. Role of two arginine residues in domain II, loop 2 of Cry1Ab and Cry1Ac *Bacillus thuringiensis* delta-endotoxin in toxicity and binding to *Manduca sexta* and *Lymantria dispar* aminopeptidase N. Mol Microbiol 2000;38(2):289-298.
72. Tuntitippawan T, Boonserm P, Katzenmeier G, Angsuthanasombat C. Targeted mutagenesis of loop residues in the receptor-binding domain of the *Bacillus thuringiensis* Cry4Ba toxin affects larvicidal activity. FEMS Microbiol Lett 2005;242(2):325-332.
73. Abdul-Rauf M, Ellar DJ. Mutations of loop 2 and loop 3 residues in domain II of *Bacillus thuringiensis* Cry1C delta-endotoxin affect insecticidal specificity and initial binding to *Spodoptera littoralis* and *Aedes aegypti* midgut membranes. Curr Microbiol 1999;39(2):94-98.
74. Smedley DP, Ellar DJ. Mutagenesis of three surface-exposed loops of a *Bacillus thuringiensis* insecticidal toxin reveals residues important for toxicity, receptor recognition and possibly membrane insertion. Microbiology 1996;142 ( Pt 7):1617-16124.
75. Chayaratanasin P, Moonsom S, Sakdee S, Chaisri U, Katzenmeier G, Angsuthanasombat C. High level of soluble expression in *Escherichia coli* and characterisation of the cloned *Bacillus thuringiensis* Cry4Ba domain III fragment. J Biochem Mol Biol 2007;40(1):58-64.
76. Knowles BH, Ellar D. Colloid-osmotic lysis is a general feature of the mechanism of action of *Bacillus thuringiensis* delta-endotoxin with different insect specificity. Biochim Biophys Acta 1987;924:509-518.
77. Von Tersch MA, Slatin SL, Kulesza CA, English LH. Membrane-permeabilizing activities of *Bacillus thuringiensis* coleopteran-active toxin CryIIIB2 and CryIIIB2 domain I peptide. Appl Environ Microbiol 1994;60(10):3711-3717.
78. Gazit E, La Rocca P, Sansom MS, Shai Y. The structure and organization within the membrane of the helices composing the pore-forming domain of

- Bacillus thuringiensis* delta-endotoxin are consistent with an "umbrella-like" structure of the pore. Proc Natl Acad Sci U S A 1998;95(21):12289-12294.
79. Masson L, Tabashnik BE, Liu YB, Brousseau R, Schwartz JL. Helix 4 of the *Bacillus thuringiensis* Cry1Aa toxin lines the lumen of the ion channel. J Biol Chem 1999;274(45):31996-2000.
  80. Feng Q, Becktel WJ. pH-induced conformational transitions of Cry IA(a), Cry IA(c), and Cry IIIA delta-endotoxins in *Bacillus thuringiensis*. Biochemistry 1994;33(28):8521-8526.
  81. Guereca L, Bravo A. The oligomeric state of *Bacillus thuringiensis* Cry toxins in solution. Biochim Biophys Acta 1999;1429(2):342-350.
  82. Aronson AI, Geng C, Wu L. Aggregation of *Bacillus thuringiensis* Cry1A toxins upon binding to target insect larval midgut vesicles. Appl Environ Microbiol 1999;65(6):2503-2507.
  83. Cooper MA, Carroll J, Travis E, Williams DH, Ellar DJ. *Bacillus thuringiensis* Cry1Ac toxin interaction with *Manduca sexta* aminopeptidase N in a model membrane environment. Biochem J 1998;333:677-683.
  84. Sramala I, Uawithya P, Chanama U, Leetachewa S, Krittanai C, Katzenmeier G, Panyim S, Angsuthanasombat C. Single proline substitutions of selected helices of the *Bacillus thuringiensis* Cry4Ba toxin effect inclusion solubility and larvicidal activity. J Biochem Mol Biol Biophys 2000;4:187-193.
  85. Chandra A, Ghosh P, Mandaokar AD, Bera AK, Sharma RP, Das S. Amino acid substitution in alpha-helix 7 of Cry1Ac delta-endotoxin of *Bacillus thuringiensis* leads to enhanced toxicity to *Helicoverpa armigera* Hubner. FEBS Lett 1999;458(2):175-179.
  86. Park HW, Federici BA. Effect of specific mutations in helix alpha7 of domain I on the stability and crystallization of Cry3A in *Bacillus thuringiensis*. Mol Biotechnol 2004;27(2):89-100.
  87. Puntheeranurak T, Leetachewa S, Katzenmeier G, Panyim S, Angsuthanasombat C. Expression and biochemical characterisation of the *Bacillus thuringiensis* Cry4B  $\alpha$ 4- $\alpha$ 5 pore-forming fragment. J Biochem Mol Biol Biophys 2001;34:293-298.

88. Sramala I, Leetachewa S, Krittanai C, Katzenmeier G, Panyim S, Angsuthanasombat C. Charged residues screening in helix 4 of the *Bacillus thuringiensis* Cry4Ba toxin reveals on critical residue for larvicidal activity. *J Biochem Mol Biol Biophys* 2001;5:219-225.
89. Vachon V, Prefontaine G, Rang C, Coux F, Juteau M, Schwartz JL, Brousseau R, Frutos R, Laprade R. Helix 4 mutants of the *Bacillus thuringiensis* insecticidal toxin Cry1Aa display altered pore-forming abilities 2004;70(10):6123-6130.
90. Kanintronkul Y, Sramala I, Katzenmeier G, Panyin S, Angsuthanasombat C. specific mutations within the  $\alpha$ 4- $\alpha$ 5 loop of the *Bacillus thuringiensis* Cry4B toxin reveal a crucial role for Asn-166 and Tyr-170. *Mol Biotechnol* 2003;24(1):11-20.
91. Tapaneeyakorn S, Pornwiroon W, Katzenmeier G, Angsuthanasombat C. Structural requirements of the unique disulphide bond and the proline-rich motif within the alpha4-alpha5 loop for larvicidal activity of the *Bacillus thuringiensis* Cry4Aa delta-endotoxin. *Biochem Biophys Res Commun* 2005;330(2):519-525.
92. Leetachewa S, Katzenmeier G, Angsuthanasombat C. Novel preparation and characterization of the alpha4-loop-alpha5 membrane-perturbing peptide from the *Bacillus thuringiensis* Cry4Ba delta-endotoxin. *J Biochem Mol Biol* 2006;39(3):270-277.
93. Tomimoto K, Hayakawa T, Hori H. Pronase digestion of brush border membrane-bound Cry1Aa shows that almost the whole activated Cry1Aa molecule penetrates into the membrane. *Comp Biochem Physiol B Biochem Mol Biol* 2006;144(4):413-422.
94. Haris PI, Chapman D. The conformational analysis of peptides using Fourier transform IR spectroscopy. *Biopolymers* 1995;37(4):251-263.
95. Goormaghtigh E, Raussens V, Ruyschaert JM. Attenuated total reflection infrared spectroscopy of proteins and lipids in biological membranes. *Biochim Biophys Acta* 1999;1422(2):105-185.

96. Chia CS, Torres J, Cooper MA, Arkin IT, Bowie JH. The orientation of the antibiotic peptide maculatin 1.1 in DMPG and DMPC lipid bilayers. Support for a pore-forming mechanism. *FEBS Lett* 2002;512(1-3):47-51.
97. Anderluh G, Dalla Serra M, Viero G, Guella G, Macek P, Menestrina G. Pore formation by equinatoxin II, a eukaryotic protein toxin, occurs by induction of nonlamellar lipid structures. *J Biol Chem* 2003;278(46):45216-45223.
98. le Coutre J, Narasimhan LR, Patel CK, Kaback HR. The lipid bilayer determines helical tilt angle and function in lactose permease of *Escherichia coli*. *Proc Natl Acad Sci U S A* 1997;94(19):10167-10171.
99. Vie V, Van Mau N, Pomarede P, Dance C, Schwartz JL, Laprade R. Lipid-induced pore formation of the *Bacillus thuringiensis* Cry1Aa insecticidal toxin. *J Membr Biol* 2001;180(3):195-203.
100. Arrondo JL, Muga A, Castresana J, Goni FM. Quantitative studies of the structure of proteins in solution by Fourier-transform infrared spectroscopy. *Prog Biophys Mol Biol* 1993;59(1):23-56.
101. Tamm LK, Tatulian SA. Infrared spectroscopy of proteins and peptides in lipid bilayers. *Q Rev Biophys* 1997;30(4):365-429.
102. Torres J, Kukol A, Goodman JM, Arkin IT. Site-specific examination of secondary structure and orientation determination in membrane proteins: the peptidic  $^{13}\text{C}=\text{O}$  group as a novel infrared probe. *Biopolymers* 2001;59(6):396-401.
103. Torres J, Adams PD, Arkin IT. Use of a new label,  $^{13}\text{C}=\text{O}$ , in the determination of a structural model of phospholamban in a lipid bilayer. Spatial restraints resolve the ambiguity arising from interpretations of mutagenesis data. *J Mol Biol* 2000;300(4):677-685.
104. Torres J, Kukol A, Arkin IT. Use of a single glycine residue to determine the tilt and orientation of a transmembrane helix. A new structural label for infrared spectroscopy. *Biophys J* 2000;79(6):3139-3143.
105. Torres J, Parthasarathy K, Lin X, Saravanan R, Kukol A, Liu DX. Model of a putative pore: the pentameric alpha-helical bundle of SARS coronavirus E protein in lipid bilayers. *Biophys J* 2006;91(3):938-947.

106. Forrest LR, Kukol A, Arkin IT, Tieleman DP, Sansom MS. Exploring models of the influenza A M2 channel: MD simulations in a phospholipid bilayer. *Biophys J* 2000;78(1):55-69.
107. Kukol A, Arkin IT. Structure of the influenza C virus CM2 protein transmembrane domain obtained by site-specific infrared dichroism and global molecular dynamics searching. *J Biol Chem* 2000;275(6):4225-4229.
108. Kukol A, Arkin IT. Vpu transmembrane peptide structure obtained by site-specific fourier transform infrared dichroism and global molecular dynamics searching. *Biophys J* 1999;77(3):1594-1601.
109. Getahun Z, Huang CY, Wang T, Leon BD, DeGrado WF, Gai F. Using nitrile-derivatized amino acids as infrared probes of local environment. *JACS* 2002;125:405-411.
110. Tucker MJ, Getahun Z, Nanda V, DeGrado WF, Gai F. A new method for determining the local environment and orientation of individual side chains of membrane-binding peptides. *J Am Chem Soc* 2004;126(16):5078-5079.
111. Sumandea M, Das S, Sumandea C, Cho W. Roles of aromatic residues in high interfacial activity of *Naja naja atra* phospholipase A2. *Biochemistry* 1999;38(49):16290-16297.
112. Arbuzova A, Wang L, Wang J, Hangyas-Mihalyne G, Murray D, Honig B. Membrane binding of peptides containing both basic and aromatic residues. Experimental studies with peptides corresponding to the scaffolding region of caveolin and the effector region of MARCKS. *Biochemistry* 2000;39(33):10330-10339.
113. Haga K, Kanai R, Sakamoto O, Aoyagi M, Harata K, Yamane K. Effects of essential carbohydrate/aromatic stacking interaction with Tyr100 and Phe259 on substrate binding of cyclodextrin glycosyltransferase from alkalophilic *Bacillus* sp. 1011. *J Biochem (Tokyo)* 2003;134(6):881-891.
114. Bemporad F, Taddei N, Stefani M, Chiti F. Assessing the role of aromatic residues in the amyloid aggregation of human muscle acylphosphatase. *Protein Sci* 2006;15(4):862-870.
115. Sambrook J, Russell DW. *Molecular cloning a laboratory manual*. ed 3, New York, Cold Spring Harbor Laboratory Press. 2001

116. Bradford MM. A rapid and sensitive method for the quantitation of microgram quantities of protein utilizing the principle of protein-dye binding. *Anal Biochem* 1976;72:248-254.
117. Angsuthanasombat C, Chungjatupornchai W, Kertbundit S, Luxananil P, Settasatian C, Wilairat P. Cloning and expression of 130-kd mosquito-larvicidal delta-endotoxin gene of *Bacillus thuringiensis* var. *israelensis* in *Escherichia coli*. *Mol Gen Genet* 1987;208(3):384-389.
118. Mrsny RJ, Volwerk JJ, Griffith OH. A simplified procedure for lipid phosphorus analysis shows that digestion rates vary with phospholipid structure. *Chem Phys Lipids* 1986;39(1-2):185-191.
119. Allen TM, Cleland LG. Serum-induced leakage of liposome contents. *Biochim Biophys Acta* 1980;597(2):418-426.
120. Braiman MS, Rothschild KJ. Fourier transform infrared techniques for probing membrane protein structure. *Annu Rev Biophys Biophys Chem* 1988;17:541-570.
121. Shnaper S, Sackett K, Gallo SA, Blumenthal R, Shai Y. The C- and the N-terminal regions of glycoprotein 41 ectodomain fuse membranes enriched and not enriched with cholesterol, respectively. *J Biol Chem* 2004;279(18):18526-18534.
122. Arkin IT, Russ WP, Lebendiker M, Schuldiner S. Determining the secondary structure and orientation of EmrE, a multi-drug transporter, indicates a transmembrane four-helix bundle. *Biochemistry* 1996;35(22):7233-7238.
123. Marsh D, Muller M, Schmitt FJ. Orientation of the infrared transition moments for an alpha-helix. *Biophys J* 2000;78(5):2499-2510.
124. Tsuboi M, Kyogoku Y, Shimanouchi T. Infrared absorption spectra of protonated and deprotonated nucleosides. *Biochim Biophys Acta* 1962;55:1-12.
125. Harrick NJ. Internal reflection spectroscopy. New York, Interscience Publishers, 1967
126. Marsh D. Quantitation of secondary structure in ATR infrared spectroscopy. *Biophys J* 1999;77(5):2630-2637.

127. Brunger AT. X-PLOR Version 3.1. A system for X-ray crystallography and NMR. Yale University Press, New Haven, 1992
128. Vriend G. WHAT IF: a molecular modeling and drug design program. *J Mol Graph* 1990;8:52-56.
129. Braun P, Von G. The aromatic residues Trp and Phe have different effects on the positioning of a transmembrane helix in the microsomal membrane. *Biochemistry* 1999;38(30):9778-9782.
130. Malovrh P, Viero G, Serra MD, Podlesek Z, Lakey JH, Macek P. A novel mechanism of pore formation: membrane penetration by the N-terminal amphipathic region of equinatoxin II. *J Biol Chem* 2003;278(25):22678-22685.
131. Drechsler A, Potrich C, Sabo JK, Frisanco M, Guella G, Dalla Serra M. Structure and activity of the N-terminal region of the eukaryotic cytotoxin equinatoxin II. *Biochemistry* 2006;45(6):1818-1828.
132. Likitvivatanavong S, Katzenmeier G, Angsuthanasombat C. Asn183 in alpha5 is essential for oligomerisation and toxicity of the *Bacillus thuringiensis* Cry4Ba toxin. *Arch Biochem Biophys* 2006;445(1):46-55.
133. Yau WM, Wimley WC, Gawrisch K, White SH. The preference of tryptophan for membrane interfaces. *Biochemistry* 1998;37(42):14713-14718.
134. Yuen CT, Davidson AR, Deber CM. Role of aromatic residues at the lipid-water interface in micelle-bound bacteriophage M13 major coat protein. *Biochemistry* 2000;39(51):16155-16162.
135. Schwartz JL, Lu YJ, Sohnlein P, Brousseau R, Laprade R, Masson L. Ion channels formed in planar lipid bilayers by *Bacillus thuringiensis* toxins in the presence of *Manduca sexta* midgut receptors. *FEBS Lett* 1997;412(2):270-276.
136. Marheineke K, Grunewald S, Christie W, Reilander H. Lipid composition of *Spodoptera frugiperda* (Sf9) and *Trichoplusia ni* (Tn) insect cells used for baculovirus infection. *FEBS Lett* 1998;441(1):49-52.
137. Atella GC, Shahabuddin M. Differential partitioning of maternal fatty acid and phospholipid in neonate mosquito larvae. *J Exp Biol* 2002;205(Pt 23):3623-3630.

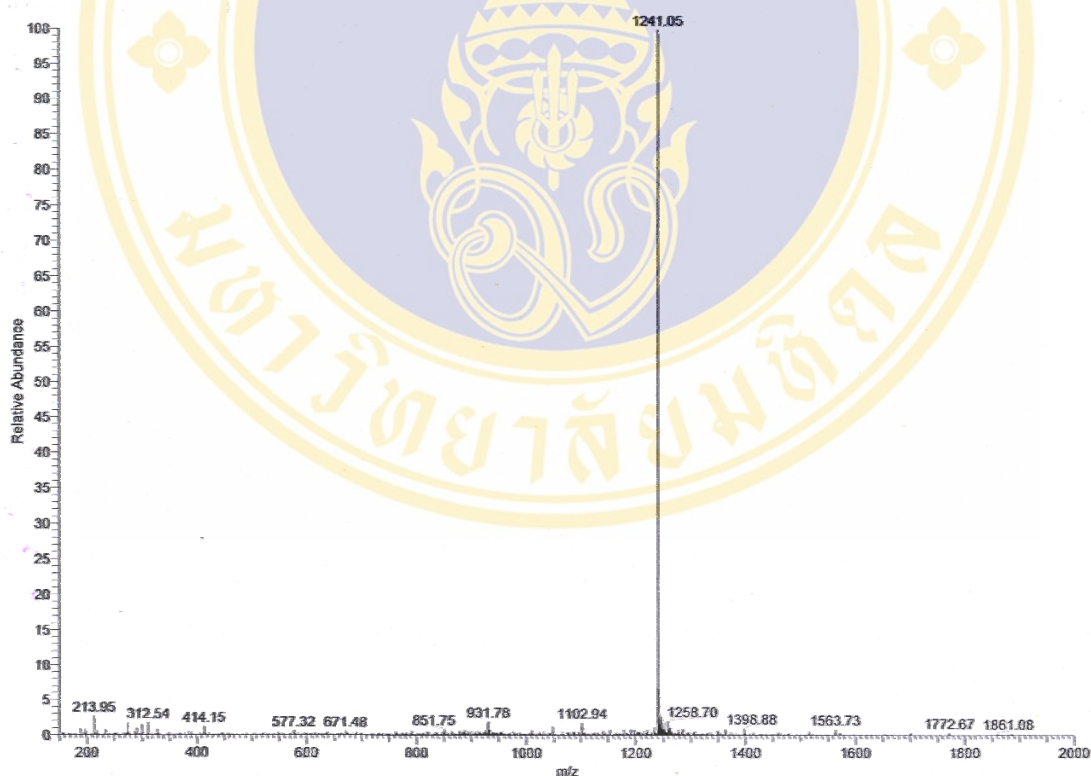
138. Gazit E, Shai Y. The assembly and organization of the alpha 5 and alpha 7 helices from the pore-forming domain of *Bacillus thuringiensis* delta-endotoxin. Relevance to a functional model. *J Biol Chem* 1995;270(6):2571-2578.
139. Karp ES, Tiburu EK, Abu-Baker S, Lorigan GA. The structural properties of the transmembrane segment of the integral membrane protein phospholamban utilizing (13)C CPMAS, (2)H, and REDOR solid-state NMR spectroscopy. *Biochim Biophys Acta* 2006;1758(6):772-780.
140. Seelig A, Alt T, Lotz S, Holzemann G. Binding of substance P agonists to lipid membranes and to the neurokinin-1 receptor. *Biochemistry* 1996;35(14):4365-4374.
141. Terzi E, Holzemann G, Seelig J. Interaction of Alzheimer beta-amyloid peptide(1-40) with lipid membranes. *Biochemistry* 1997;36(48):14845-14852.
142. Terzi E, Holzemann G, Seelig J. Alzheimer beta-amyloid peptide 25-35: electrostatic interactions with phospholipid membranes. *Biochemistry* 1994;33(23):7434-7441.
143. Terzi E, Holzemann G, Seelig J. Self-association of beta-amyloid peptide (1-40) in solution and binding to lipid membranes. *J Mol Biol* 1995;252(5):633-642.
144. Butko P. Cytolytic toxin Cyt1A and its mechanism of membrane damage: data and hypotheses. *Appl Environ Microbiol* 2003;69(5):2415-2422.
145. Biggin PC, Sansom MS. Simulation of voltage-dependent interactions of alpha-helical peptides with lipid bilayers. *Biophys Chem* 1996;60(3):99-110.
146. Tilley SJ, Orlova EV, Gilbert RJ, Andrew PW, Saibil HR. Structural basis of pore formation by the bacterial toxin pneumolysin. *Cell* 2005;121(2):247-256.
147. Iacovache I, Paumard P, Scheib H, Lesieur C, Sakai N, Matile S. A rivet model for channel formation by aerolysin-like pore-forming toxins. *Embo J* 2006;25(3):457-466.



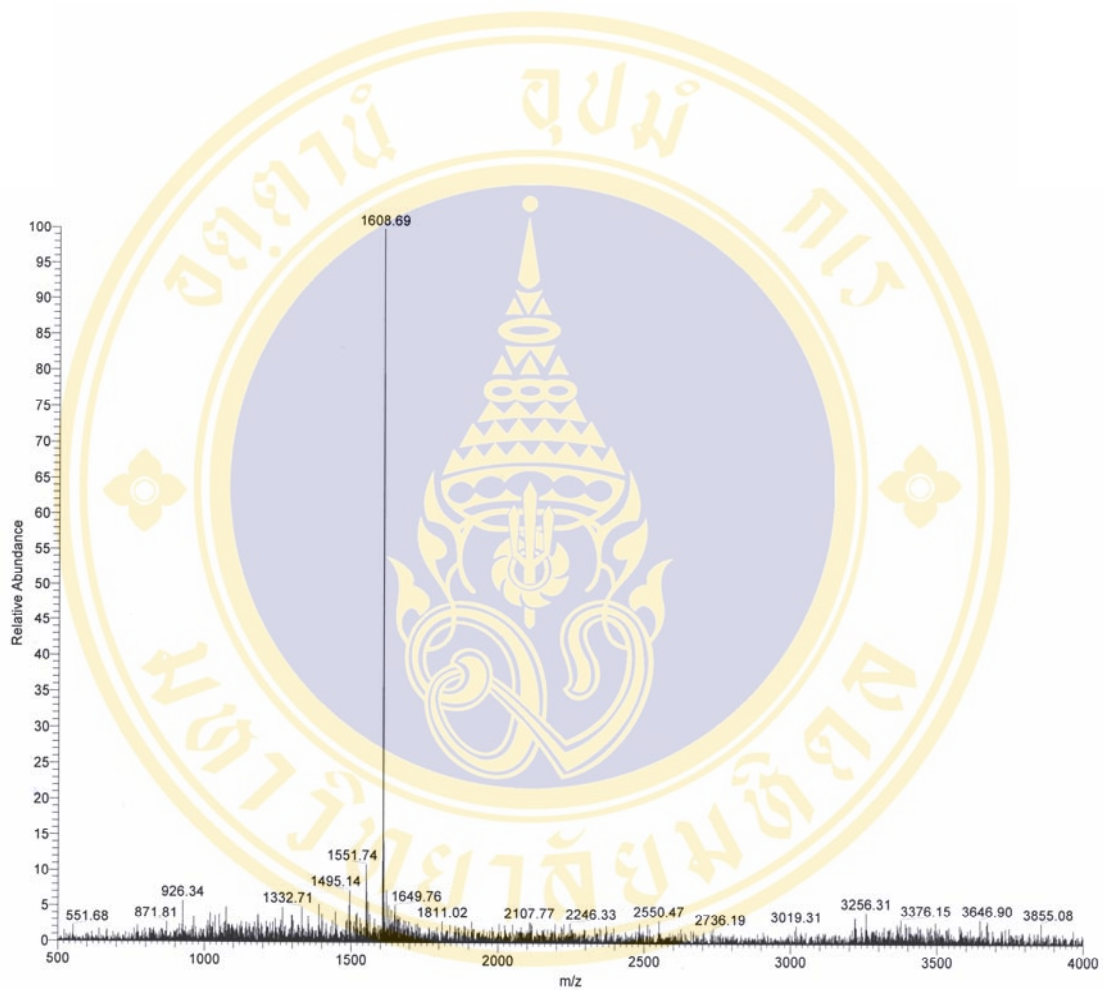
## APPENDIX

**Appendix 1: Molecular mass determination of the peptide by using mass spectrometry**

(A) The mass spectrum of helix 6 peptide is shown below. The spectrum displays a dominant molecular ion at  $m/z$  1241.05 Da, which is consistent with the expected molecular mass 3723.15 Da, as the value of  $Z$  (number of charges) equal 3.



(B) The mass spectrum of helix 7 peptide displays a dominant molecular ion at  $m/z$  1608.69 Da, which is consistent with the theoretical molecular mass 3217.40 Da, as the value of  $Z$  (number of charges) equal 2.



## BIOGRAPHY

<b>NAME</b>	Miss Kasorn Tiewsir
<b>DATE OF BIRTH</b>	18 December 1980
<b>PLACE OF BIRTH</b>	Bangkok, Thailand
<b>HOME ADDRESS</b>	20 Soi Watbaromnivhat, Rama 1, Rongmuang, Pathumwun, Bangkok, 10330, Thailand Tel. 0-2215-4980 Email: kasorn00@hotmail.com
<b>INSTITUTIONS ATTENDED</b>	Mahidol University, 1999-2003 Bachelor degree of Science (Medical Technology) Mahidol University, 2005-2007 Doctor of Philosophy (Molecular Genetics and Genetic Engineering)
<b>AWARD &amp; SCHOLARSHIP</b>	The Royal Golden Jubilee Ph.D. Scholarship (2003-2007) from the Thailand Research Fund Awarded 1 <sup>st</sup> for Poster presentation (2006): Joint Third AOHUPO and Fourth Structural Biology and Functional Genomics Conference, Singapore

## PUBLICATIONS & INTERNATIONAL MEETING ABSTRACTS

1. Tiewsir, K. *et al.* (2007) Structurally conserved aromaticity of Tyr<sup>249</sup> and Phe<sup>264</sup> in helix 7 is important for toxicity of the *Bacillus thuringiensis* Cry4Ba toxin. *J. Biochem. Mol. Biol.* (in press).
2. Tiewsir, K. *et al.* (2005) Directed mutagenesis of conserved aromatic residues in helix 7 critical for larvicidal activity of the *Bacillus thuringiensis* Cry4Ba toxin. *In* Abstract of the **4<sup>th</sup> International Conference on Biopesticides**, February 13-18, 2005, Chiang Mai, Thailand.
3. Tiewsir, K. *et al.* (2005) Functional significance of conserved aromatic residues in helix 7 critical for larvicidal activity of the *Bacillus thuringiensis* Cry4Ba toxin. *In* Abstract of **38<sup>th</sup> Annual Meeting of the Society for Invertebrate Pathology Anchorage**, August 7-13, 2005, Alaska, U.S.A.
4. Tiewsir, K. *et al.* (2006) Structures and orientations within phospholipid membranes of the  $\alpha 7$  peptide from the pore-forming domain of the *Bacillus thuringiensis* Cry4Ba toxin. *In* Abstract of **The American Society for Cell Biology 46<sup>th</sup> Annual Meeting**, December 9-13, 2006, San Diego, California, U.S.A.
5. Tiewsir, K. *et al.* (2006) Functional significance of conserved aromatic residues in helix 7 critical for larvicidal activity of the *Bacillus thuringiensis* Cry4Ba toxin. *In* Abstract of **First Annual Symposium of the Protein Society of Thailand "Challenges in Protein Research in Thailand"**, October 24-25, 2006, CRI, Thailand.
6. Tiewsir, K. *et al.* (2006) Structures and orientations within phospholipid membranes of the  $\alpha 7$  peptide from the pore-forming domain of the *Bacillus thuringiensis* Cry4Ba toxin. *In* Abstract of **Joint Third AOHUPO and Fourth Structural Biology and Functional Genomics Conference**, December 4-7, 2006, NUS, Singapore.